Interrogating Electronic and Ionic Carrier Motion in Halide Perovskites with Scanning Probe Microscopy

Justin Pothoof

A dissertation
submitted in partial fulfillment of the
requirements for the degree of

Doctor of Philosophy

University of Washington

2024

Reading Committee:

David S. Ginger, Chair

Cody Schlenker

Dan Fu

Program authorized to offer degree:

Department of Chemistry

University of Washington

Abstract

Interrogating Electronic and Ionic Carrier Motion in Halide Perovskites with Scanning Probe Microscopy

Justin Pothoof

Chair of the Supervisory Committee:
David S. Ginger
Department of Chemistry

In December of 2015, 194 states and the European Union reached The Paris Agreement – an ambitious global goal asking all countries to undertake efforts to limit global temperatures from exceeding 2 °C above pre-industrial levels. Ultimately, this has led to many countries, including the United States, to set a milestone of achieving net-zero greenhouse gas (GHG) emissions by the year 2050. Replacing fossil fuel usage with clean energy technology to generate electricity is one primary way to reduce GHG emissions. Lead halide perovskite semiconductors have emerged as highly efficient photovoltaic active layers, with power conversion efficiencies (PCE) on par with silicon – the industry standard. However, perovskites lag behind silicon in terms of long-term and operating stability. The ability of perovskite materials to conduct ions through their lattice is considered to be a large contributor to the lowered stability. We used scanning probe microscopy (SPM) to further our understanding of ionic motion in lead halide perovskites. We first used scanning kelvin probe microscopy (SKPM) to investigate how ionic motion varies with dimensionality in 2D perovskite layers undergoing an applied electric field. In this study, we investigated BA_2PbI_4 (n=1) and $BA_2MA_3Pb_4I_{13}$ (~<n>=4), where BA is butylammonium and

MA is methylammonium. We demonstrated that 2D perovskite materials undergo ionic migration, similar to their 3D counterparts, and investigated how those dynamics change under illumination. We extracted the rate of change in the contact potential difference (CPD) at temperatures ranging from 283 – 313 K and generated Arrhenius plots to calculated activation energies. In the dark, we calculated activation energies ~0.61 eV, which agrees well with the activation energy attributed to iodide ionic migration. Next, we modified the SKPM technique to probe the shift in the contact potential difference (CPD) between the AFM tip and perovskite sample immediately after applying an electric field between the sample substrate and tip. We used this technique to determine the suppression in ion motion after passivation with (3-aminopropyl)trimethoxy silane (APTMS). We found that APTMS defect passivation led to a reduction in CPD shift resulting from ionic migration from 100 to 20 mV. We further confirmed the success of APTMS defect passivation by showing a suppression in halide phase segregation using hyperspectral photoluminescence microscopy. Finally, we employed time-resolved electrostatic force microscopy (trEFM) to probe carrier recombination dynamics with sub-diffraction-limited spatial resolution. We hypothesize that trEFM is measuring the time it takes for the surface potential to equilibrate during photoexcitation. We showed that the photo-induced dynamics measured with trEFM correlate strongly with both carrier lifetimes and surface recombination velocities (SRV) measured by time-resolved photoluminescnece through the use of various surface passivating agents. Using drift-diffusion simulations, we demonstrated that the surface potential equilibration time is primarily influenced by the SRV and ion motion. On the nanoscale, trEFM revealed slower surface potential equilibration times at grain boundaries, which we propose is due to locally higher concentration of defects, such as halide vacancies, that mediate ion migration. Furthermore, we observed overall slower dynamics after passivation due

to the suppression of SRV. However, we still observed heterogeneity in the equilibration times measured after passivation, which we hypothesize is a result of local variations in the effectiveness and uniformity of passivation. We further supported our findings through a combination of intensity dependent and wavelength dependent measurements.

Table of Contents

Table of Figures

Chapter 1: Introduction

1.1 Lead Halide Perovskites

Lead halide perovskites are semiconducting materials with promising applications in various optoelectronic devices.[1–3] Indeed, single-junction, perovskite photovoltaics have surpassed 26% efficiency, on par with silicon-based technologies.[4] Perovskite semiconductors have an ABX_3 crystal structure with corner-sharing octahedron, where A is a monovalent cation such as methylammonium (MA^+), formamidinium (FA^+), or cesium (Cs^+), B is a divalent metal cation like lead (Pb^{2+}) or tin (Sn^{2+}), and X is a halide anion such as iodide (I^-), bromide (Br^-) or chloride (Cl^-). These materials can also be scaled down to a 2D structure with the formula $A'_2A_{n-1}B_nX_{3n-1}$ through the integration of a bulky, organic cation (A') such as butylammonium (BA^+) or phenylethylammonium (PEA^+), which separate the inorganic, lead-halide octahedron layers into planes of thickness n. Figure 1.1 illustrates the crystal structure for both 3D and 2D perovskite materials.

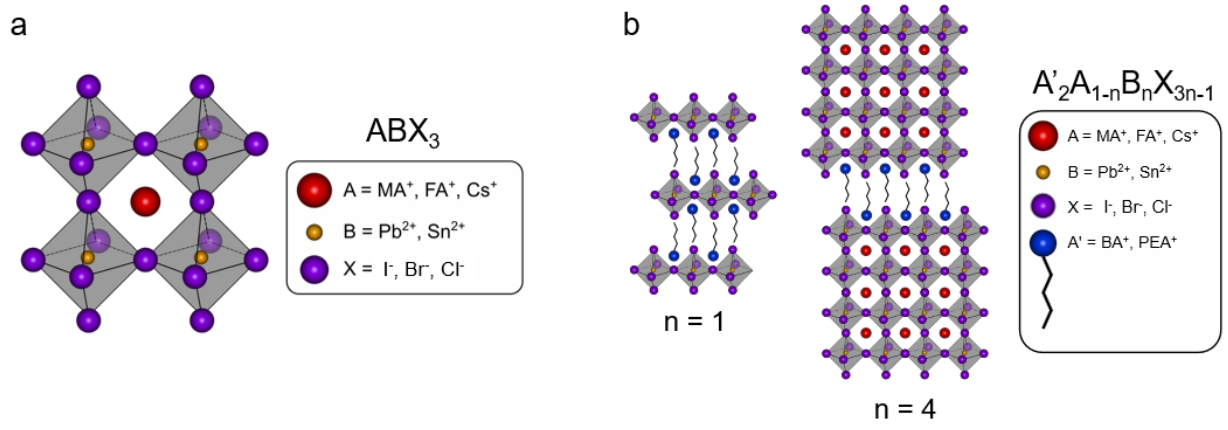

Figure 1.1. (a) ABX_3 crystal structure for a 3D perovskite material. (b) $A'_2A_{n-1}B_nX_{3n-1}$ crystal structure illustrations for n = 1 and n = 4 2D perovskite materials.

Perovskite semiconductors possess many attractive properties including solution processability, large absorption coefficients, and high carrier mobilities;[5,6] all of which make these materials more cost effective compared to standard semiconductors.[7,8] Furthermore, the perovskite bandgap can be easily tuned across the entire visible light spectrum by substituting and alloying the A, B, and X sites.[9] In lead halide perovskites, the valence band is formed by the overlap of lead 6s and halide 5p orbitals while the conduction band is formed by the overlap of lead 6p and halide 5s and 5p orbitals.[10] For this reason, lattice defects, for instance halide vacancies and interstitials, tend to energetically lie within or near the conduction and valence band.[11] Thus, these defects are described as "shallow traps" as there is not significant energy loss by electronic carriers being trapped at those sites.[11] Consequently, the field as described halide perovskites as being "defect tolerant".[12,13]

1.2 Ion Migration

While perovskite semiconductors may be defect tolerant, they are not defect free. Due to the soft nature of the perovskite lattice and the weak ionic interactions, those same lattice defects serve as channels for ion migration.[14] Figure 1.2 illustrates how ion migration occurs through the perovskite lattice, where neighboring ions are able to hop through vacancies and interstitials migrate throughout the lattice. Thus, halide perovskites are mixed electronic-ionic conductors.[15] The presence of ion motion in these materials leads to various phenomena that limit the long-term stability of perovskite-based devices, including current-voltage hysteresis,[16] electrochemical reactions,[17] and phase segregation.[18] Hence, to enhance the stability of these materials and aid in their ultimate commercialization, we have to both understand and mitigate the effects of ion migration.

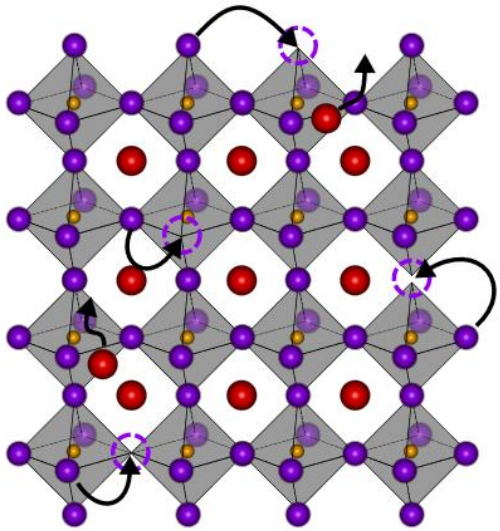

Figure 1.2. Illustration of ion migration occurring through lattice defects. Halide vacancies are shown as dashed, purple circles; vacancy-mediated ion migration is shown as neighboring vacancies hop into vacancy sites. Additionally, A-site interstitials (extra red spheres) are also shown flowing through the perovskite lattice.

Various efforts have been made to suppress ion motion: the use of 2D perovskites,[19] compositional engineering,[20] solution additives,[21] and surface passivation treatments.[22] The bulky, organic cation introduced in 2D perovskites is believed to also prevent mobile ion from migrating layer-to-layer. Thus, the field has developed 2D/3D perovskite heterojunctions to mitigate ion motion and improve photovoltaic performance and stability.[23] Furthermore, many of the most successful perovskite semiconductors have mixed A sites, with FA^+ and Cs^+, and mixed X sites, with I^- and Br^-.[24–26] Finally, solution additives and post-treatment of perovskite layers with surface passivators has been shown to suppress nonradiative recombination through the treatment of lattice defects.[27–31] Decreasing the concentration of lattice defects should, in turn, mitigate the effects of ion migration.

1.3 Scanning probe microscopy

A significant contribution to our understanding of perovskite materials has been with the application of microscopy. Confocal photoluminescence microscopy and scanning electron microscopy techniques have provided invaluable information on the perovskite microstructure and electronic carrier dynamics.[32–35] However, these techniques are either diffraction limited or inherently damage the perovskite,[36,37] making correlative measurements difficult. In modern perovskite formulations with both mixed A and X sites, perovskite grains in polycrystalline films are 100 – 200 nm in diameter. Thus, the ideal microscopy tool can image the optoelectronic properties of perovskites below the optical diffraction limit in a nondestructive manner.

Scanning probe microscopy (SPM) uses a metallic tip to map the surface of materials with nanometer level spatial resolution.[38] Furthermore, SPM can be used to probe the optoelectronic properties of perovskites on the nanoscale, for instance, scanning Kelvin probe microscopy (SKPM) maps the surface potential of the material,[39] conductive atomic force microscopy (cAFM) can be used to understand nanoscale variation in charge injection and charge extraction,[30] and time-resolved electrostatic force microscopy (trEFM) tracks transient changes in photo-induced dynamics[40–42] – allowing us to map carrier recombination and ion motion below the diffraction limit.

The objective of this thesis is to further our understanding of the mixed electronic-ionic nature of halide perovskite with the use of SPM. We show how SKPM can be used to measure ion migration in both 2D and 3D perovskite materials, and prove the suppression of ion motion with chemical surface passivation. Further, we employ trEFM to image carrier recombination dynamics with sub-diffraction-limited resolution. With both experimental and simulated support, we show trEFM is probing the time it takes for the perovskite surface potential to equilibrate,

which is *strongly* dependent on the local surface recombination velocity (SRV), but also

impacted by local ion motion.

1.4 References

(1) Chen, H.; Liu, C.; Xu, J.; Maxwell, A.; Zhou, W.; Yang, Y.; Zhou, Q.; Bati, A. S. R.; Wan, H.; Wang, Z.; Zeng, L.; Wang, J.; Serles, P.; Liu, Y.; Teale, S.; Liu, Y.; Saidaminov, M. I.; Li, M.; Rolston, N.; Hoogland, S.; Filleter, T.; Kanatzidis, M. G.; Chen, B.; Ning, Z.; Sargent, E. H. Improved Charge Extraction in Inverted Perovskite Solar Cells with Dual-Site-Binding Ligands. *Science* **2024**, *384* (6692), 189–193. https://doi.org/10.1126/science.adm9474.

(2) Li, M.; Yang, Y.; Kuang, Z.; Hao, C.; Wang, S.; Lu, F.; Liu, Z.; Liu, J.; Zeng, L.; Cai, Y.; Mao, Y.; Guo, J.; Tian, H.; Xing, G.; Cao, Y.; Ma, C.; Wang, N.; Peng, Q.; Zhu, L.; Huang, W.; Wang, J. Acceleration of Radiative Recombination for Efficient Perovskite LEDs. *Nature* **2024**, *630* (8017), 631–635. https://doi.org/10.1038/s41586-024-07460-7.

(3) Feng, X.; Li, C.; Song, J.; He, Y.; Qu, W.; Li, W.; Guo, K.; Liu, L.; Yang, B.; Wei, H. Differential Perovskite Hemispherical Photodetector for Intelligent Imaging and Location Tracking. *Nat. Commun.* **2024**, *15* (1), 577. https://doi.org/10.1038/s41467-024-44857-4.

(4) *Best Research-Cell Efficiency Chart*. https://www.nrel.gov/pv/cell-efficiency.html (accessed 2024-11-17).

(5) Faridi, A. W.; Imran, M.; Tariq, G. H.; Ullah, S.; Noor, S. F.; Ansar, S.; Sher, F. Synthesis and Characterization of High-Efficiency Halide Perovskite Nanomaterials for Light-Absorbing Applications. *Ind. Eng. Chem. Res.* **2023**, *62* (11), 4494–4502. https://doi.org/10.1021/acs.iecr.2c00416.

(6) Zhao, Y.; Nardes, A. M.; Zhu, K. Solid-State Mesostructured Perovskite $CH_3NH_3PbI_3$ Solar Cells: Charge Transport, Recombination, and Diffusion Length. *J. Phys. Chem. Lett.* **2014**, *5* (3), 490–494. https://doi.org/10.1021/jz500003v.

(7) Zhang, C.; Park, N.-G. Materials and Methods for Cost-Effective Fabrication of Perovskite Photovoltaic Devices. *Commun. Mater.* **2024**, *5* (1), 1–13. https://doi.org/10.1038/s43246-024-00636-8.

(8) Cai, M.; Wu, Y.; Chen, H.; Yang, X.; Qiang, Y.; Han, L. Cost-Performance Analysis of Perovskite Solar Modules. *Adv. Sci.* **2017**, *4* (1), 1600269. https://doi.org/10.1002/advs.201600269.

(9) Kulkarni, S. A.; Baikie, T.; Boix, P. P.; Yantara, N.; Mathews, N.; Mhaisalkar, S. Band-Gap Tuning of Lead Halide Perovskites Using a Sequential Deposition Process. *J Mater Chem A* **2014**, *2* (24), 9221–9225. https://doi.org/10.1039/C4TA00435C.

(10) Umebayashi, T.; Asai, K.; Kondo, T.; Nakao, A. Electronic Structures of Lead Iodide Based Low-Dimensional Crystals. *Phys. Rev. B* **2003**, *67* (15), 155405. https://doi.org/10.1103/PhysRevB.67.155405.

(11) Huang, J.; Yuan, Y.; Shao, Y.; Yan, Y. Understanding the Physical Properties of Hybrid Perovskites for Photovoltaic Applications. *Nat. Rev. Mater.* **2017**, *2* (7), 1–19. https://doi.org/10.1038/natrevmats.2017.42.

(12) Ye, J.; Mondal, N.; Carwithen, B. P.; Zhang, Y.; Dai, L.; Fan, X.-B.; Mao, J.; Cui, Z.; Ghosh, P.; Otero-Martínez, C.; van Turnhout, L.; Huang, Y.-T.; Yu, Z.; Chen, Z.; Greenham, N. C.; Stranks, S. D.; Polavarapu, L.; Bakulin, A.; Rao, A.; Hoye, R. L. Z. Extending the Defect Tolerance of Halide Perovskite Nanocrystals to Hot Carrier Cooling Dynamics. *Nat. Commun.* **2024**, *15* (1), 8120. https://doi.org/10.1038/s41467-024-52377-4.

(13) Steirer, K. X.; Schulz, P.; Teeter, G.; Stevanovic, V.; Yang, M.; Zhu, K.; Berry, J. J. Defect Tolerance in Methylammonium Lead Triiodide Perovskite. *ACS Energy Lett.* **2016**, *1* (2), 360–366. https://doi.org/10.1021/acsenergylett.6b00196.

(14) Yuan, Y.; Huang, J. Ion Migration in Organometal Trihalide Perovskite and Its Impact on Photovoltaic Efficiency and Stability. *Acc. Chem. Res.* **2016**, *49* (2), 286–293. https://doi.org/10.1021/acs.accounts.5b00420.

(15) Tress, W. Metal Halide Perovskites as Mixed Electronic–Ionic Conductors: Challenges and Opportunities—From Hysteresis to Memristivity. *J. Phys. Chem. Lett.* **2017**, *8* (13), 3106–3114. https://doi.org/10.1021/acs.jpclett.7b00975.

(16) Kang, D.; Park, N. On the Current–Voltage Hysteresis in Perovskite Solar Cells: Dependence on Perovskite Composition and Methods to Remove Hysteresis. *Adv. Mater.* **2019**, *31* (34), 1805214. https://doi.org/10.1002/adma.201805214.

(17) Jiang, F.; Shi, Y.; Rana, T. R.; Morales, D.; Gould, I. E.; McCarthy, D. P.; Smith, J. A.; Christoforo, M. G.; Yaman, M. Y.; Mandani, F.; Terlier, T.; Contreras, H.; Barlow, S.; Mohite, A. D.; Snaith, H. J.; Marder, S. R.; MacKenzie, J. D.; McGehee, M. D.; Ginger, D. S. Improved Reverse Bias Stability in p–i–n Perovskite Solar Cells with Optimized Hole Transport Materials and Less Reactive Electrodes. *Nat. Energy* **2024**. https://doi.org/10.1038/s41560-024-01600-z.

(18) Motti, S. G.; Patel, J. B.; Oliver, R. D. J.; Snaith, H. J.; Johnston, M. B.; Herz, L. M. Phase Segregation in Mixed-Halide Perovskites Affects Charge-Carrier Dynamics While Preserving Mobility. *Nat. Commun.* **2021**, *12* (1), 6955. https://doi.org/10.1038/s41467-021-26930-4.

(19) Xiao, X.; Dai, J.; Fang, Y.; Zhao, J.; Zheng, X.; Tang, S.; Rudd, P. N.; Zeng, X. C.; Huang, J. Suppressed Ion Migration along the In-Plane Direction in Layered Perovskites. *ACS Energy Lett.* **2018**, *3* (3), 684–688. https://doi.org/10.1021/acsenergylett.8b00047.

(20) Bush, K. A.; Frohna, K.; Prasanna, R.; Beal, R. E.; Leijtens, T.; Swifter, S. A.; McGehee, M. D. Compositional Engineering for Efficient Wide Band Gap Perovskites with Improved Stability to Photoinduced Phase Segregation. *ACS Energy Lett.* **2018**, *3* (2), 428–435. https://doi.org/10.1021/acsenergylett.7b01255.

(21) Zhang, F.; Zhu, K. Additive Engineering for Efficient and Stable Perovskite Solar Cells. *Adv. Energy Mater.* **2020**, *10* (13), 1902579. https://doi.org/10.1002/aenm.201902579.

(22) Xia, J.; Liang, C.; Gu, H.; Mei, S.; Li, S.; Zhang, N.; Chen, S.; Cai, Y.; Xing, G. Surface Passivation Toward Efficient and Stable Perovskite Solar Cells. *ENERGY Environ. Mater.* **2023**, *6* (1), e12296. https://doi.org/10.1002/eem2.12296.

(23) Wu, G.; Liang, R.; Ge, M.; Sun, G.; Zhang, Y.; Xing, G. Surface Passivation Using 2D Perovskites toward Efficient and Stable Perovskite Solar Cells. *Adv. Mater.* **2022**, *34* (8), 2105635. https://doi.org/10.1002/adma.202105635.

(24) Liu, C.; Yang, Y.; Chen, H.; Xu, J.; Liu, A.; Bati, A. S. R.; Zhu, H.; Grater, L.; Hadke, S. S.; Huang, C.; Sangwan, V. K.; Cai, T.; Shin, D.; Chen, L. X.; Hersam, M. C.; Mirkin, C. A.; Chen, B.; Kanatzidis, M. G.; Sargent, E. H. Bimolecularly Passivated Interface Enables Efficient and Stable Inverted Perovskite Solar Cells. *Science* **2023**, *382* (6672), 810–815. https://doi.org/10.1126/science.adk1633.

(25) Liang, Z.; Zhang, Y.; Xu, H.; Chen, W.; Liu, B.; Zhang, J.; Zhang, H.; Wang, Z.; Kang, D.-H.; Zeng, J.; Gao, X.; Wang, Q.; Hu, H.; Zhou, H.; Cai, X.; Tian, X.; Reiss, P.; Xu, B.; Kirchartz, T.; Xiao, Z.; Dai, S.; Park, N.-G.; Ye, J.; Pan, X. Homogenizing Out-of-Plane Cation Composition in Perovskite Solar Cells. *Nature* **2023**, *624* (7992), 557–563. https://doi.org/10.1038/s41586-023-06784-0.

(26) Wang, R.; Liu, X.; Yan, S.; Meng, N.; Zhao, X.; Chen, Y.; Li, H.; Qaid, S. M. H.; Yang, S.; Yuan, M.; He, T. Efficient Wide-Bandgap Perovskite Photovoltaics with Homogeneous Halogen-Phase Distribution. *Nat. Commun.* **2024**, *15* (1), 8899. https://doi.org/10.1038/s41467-024-53344-9.

(27) Ding, B.; Ding, Y.; Peng, J.; Romano-deGea, J.; Frederiksen, L. E. K.; Kanda, H.; Syzgantseva, O. A.; Syzgantseva, M. A.; Audinot, J.-N.; Bour, J.; Zhang, S.; Wirtz, T.; Fei, Z.; Dörflinger, P.; Shibayama, N.; Niu, Y.; Hu, S.; Zhang, S.; Tirani, F. F.; Liu, Y.; Yang, G.-J.; Brooks, K.; Hu, L.; Kinge, S.; Dyakonov, V.; Zhang, X.; Dai, S.; Dyson, P. J.; Nazeeruddin, M. K. Dopant-Additive Synergism Enhances Perovskite Solar Modules. *Nature* **2024**, *628* (8007), 299–305. https://doi.org/10.1038/s41586-024-07228-z.

(28) Uddin, M. A.; Rana, P. J. S.; Ni, Z.; Yang, G.; Li, M.; Wang, M.; Gu, H.; Zhang, H.; Dou, B. D.; Huang, J. Iodide Manipulation Using Zinc Additives for Efficient Perovskite Solar Minimodules. *Nat. Commun.* **2024**, *15* (1), 1355. https://doi.org/10.1038/s41467-024-45649-6.

(29) Jiang, Q.; Zhao, Y.; Zhang, X.; Yang, X.; Chen, Y.; Chu, Z.; Ye, Q.; Li, X.; Yin, Z.; You, J. Surface Passivation of Perovskite Film for Efficient Solar Cells. *Nat. Photonics* **2019**, *13* (7), 460–466. https://doi.org/10.1038/s41566-019-0398-2.

(30) Shi, Y.; Rojas-Gatjens, E.; Wang, J.; Pothoof, J.; Giridharagopal, R.; Ho, K.; Jiang, F.; Taddei, M.; Yang, Z.; Sanehira, E. M.; Irwin, M. D.; Silva-Acuña, C.; Ginger, D. S. (3-Aminopropyl)Trimethoxysilane Surface Passivation Improves Perovskite Solar Cell Performance

by Reducing Surface Recombination Velocity. *ACS Energy Lett.* **2022**, *7* (11), 4081–4088. https://doi.org/10.1021/acsenergylett.2c01766.

(31) deQuilettes, D. W.; Koch, S.; Burke, S.; Paranji, R. K.; Shropshire, A. J.; Ziffer, M. E.; Ginger, D. S. Photoluminescence Lifetimes Exceeding 8 Ms and Quantum Yields Exceeding 30% in Hybrid Perovskite Thin Films by Ligand Passivation. *ACS Energy Lett.* **2016**, *1* (2), 438–444. https://doi.org/10.1021/acsenergylett.6b00236.

(32) deQuilettes, D. W.; Vorpahl, S. M.; Stranks, S. D.; Nagaoka, H.; Eperon, G. E.; Ziffer, M. E.; Snaith, H. J.; Ginger, D. S. Impact of Microstructure on Local Carrier Lifetime in Perovskite Solar Cells. *Science* **2015**, *348* (6235), 683–686. https://doi.org/10.1126/science.aaa5333.

(33) Jariwala, S.; Sun, H.; Adhyaksa, G. W. P.; Lof, A.; Muscarella, L. A.; Ehrler, B.; Garnett, E. C.; Ginger, D. S. Local Crystal Misorientation Influences Non-Radiative Recombination in Halide Perovskites. *Joule* **2019**, *3* (12), 3048–3060. https://doi.org/10.1016/j.joule.2019.09.001.

(34) Taddei, M.; Jariwala, S.; Westbrook, R. J. E.; Gallagher, S.; Weaver, A. C.; Pothoof, J.; Ziffer, M. E.; Snaith, H. J.; Ginger, D. S. Interpreting Halide Perovskite Semiconductor Photoluminescence Kinetics. *ACS Energy Lett.* **2024**, *9* (6), 2508–2516. https://doi.org/10.1021/acsenergylett.4c00614.

(35) Orri, J. F.; Tennyson, E. M.; Kusch, G.; Divitini, G.; Macpherson, S.; Oliver, R. A.; Ducati, C.; Stranks, S. D. Using Pulsed Mode Scanning Electron Microscopy for Cathodoluminescence Studies on Hybrid Perovskite Films. *Nano Express* **2021**, *2* (2), 024002. https://doi.org/10.1088/2632-959X/abfe3c.

(36) Maznev, A. A.; Wright, O. B. Upholding the Diffraction Limit in the Focusing of Light and Sound. *Wave Motion* **2017**, *68*, 182–189. https://doi.org/10.1016/j.wavemoti.2016.09.012.

(37) Xiao, C.; Li, Z.; Guthrey, H.; Moseley, J.; Yang, Y.; Wozny, S.; Moutinho, H.; To, B.; Berry, J. J.; Gorman, B.; Yan, Y.; Zhu, K.; Al-Jassim, M. Mechanisms of Electron-Beam-Induced Damage in Perovskite Thin Films Revealed by Cathodoluminescence Spectroscopy. *J. Phys. Chem. C* **2015**, *119* (48), 26904–26911. https://doi.org/10.1021/acs.jpcc.5b09698.

(38) Umeda, K.; McArthur, S. J.; Kodera, N. Spatiotemporal Resolution in High-Speed Atomic Force Microscopy for Studying Biological Macromolecules in Action. *Microscopy* **2023**, *72* (2), 151–161. https://doi.org/10.1093/jmicro/dfad011.

(39) Melitz, W.; Shen, J.; Kummel, A. C.; Lee, S. Kelvin Probe Force Microscopy and Its Application. *Surf. Sci. Rep.* **2011**, *66* (1), 1–27. https://doi.org/10.1016/j.surfrep.2010.10.001.

(40) Karatay, D. U.; Harrison, J. S.; Glaz, M. S.; Giridharagopal, R.; Ginger, D. S. Fast Time-Resolved Electrostatic Force Microscopy: Achieving Sub-Cycle Time Resolution. *Rev. Sci. Instrum.* **2016**, *87* (5), 053702. https://doi.org/10.1063/1.4948396.

(41) Giridharagopal, R.; Precht, J. T.; Jariwala, S.; Collins, L.; Jesse, S.; Kalinin, S. V.; Ginger, D. S. Time-Resolved Electrical Scanning Probe Microscopy of Layered Perovskites Reveals

Spatial Variations in Photoinduced Ionic and Electronic Carrier Motion. *ACS Nano* **2019**, *13* (3), 2812–2821. https://doi.org/10.1021/acsnano.8b08390.

(42) Breshears, M. D.; Giridharagopal, R.; Pothoof, J.; Ginger, D. S. A Robust Neural Network for Extracting Dynamics from Electrostatic Force Microscopy Data. *J. Chem. Inf. Model.* **2022**, *62* (18), 4342–4350. https://doi.org/10.1021/acs.jcim.2c00738.

Chapter 2: Scanning Kelvin Probe Microscopy Reveals that Ion Motion Varies with Dimensionality in 2D Halide Perovskites

Adapted from Jiang, F.; Pothoof, J.; Muckel, F.; Giridharagopal, R.; Wang, J.; and Ginger, D.S. Scanning Kelvin Probe Microscopy Reveals that Ion Motion Varies with Dimensionality in 2D Halide Perovskites. ACS Energy Lett. 2021, 6, 1, 100–108. https://doi.org/10.1021/acsenergylett.0c02032.

2.1 Overview

We study ion migration in 2D lead halide perovskites of varying dimensionality using scanning Kelvin probe microscopy (SKPM). We perform potentiometry on micron-scale lateral junctions in the absence of injected charge and we compare how ion motion varies between prototypical two-dimensional n-butylammonium lead iodide perovskites (BA_2PbI_4, n=1), and methylammonium-incorporated quasi-2D perovskites ($BA_2MA_3Pb_4I_{13}$, ~<n>=4) under the effects of illumination and temperature. We attribute the observed slow dynamics to relaxation of the bias-induced ionic charge distributions at different temperatures, and we extract the activation energies associated with the ionic motion in each case. Finally, we propose an explanation for these phenomena by hypothesizing that ion motion in purely-2D BA_2PbI_4 perovskite films is dominated by paired halide and halide vacancy, whereas for quasi-2D $BA_2MA_3Pb_4I_{13}$ perovskites, the ion motion is a combination of both halide and methylammonium (vacancy) migration. These data show that dimensionality in these systems plays a critical role in ion dynamics.

2.2 Introduction

Ruddlesden-Popper two-dimensional (2D) perovskites of the form $(RNH_3)_2A_{n-1}Pb_nX_{3n+1}$, with A representing a small cation (typically $CH_3NH_3^+$ (MA^+) or $HC(CH_2)_2^+$ (FA^+)), X being a halide anion, and RNH_3 being a large organic cation such as 2-phenylethylammonium (PEA^+) or *n*-butylammonium (BA^+), have shown great potential for optoelectronic applications due to their combination of performance and stability compared with three-dimensional (3D) perovskites.[1-8] In conventional 3D lead halide perovskites with the classic $APbX_3$ structure, each inorganic $[PbX_6]^{4-}$ octahedra is connected with six neighbors via the halide anions, with small organic cations residing in the voids of the octahedra network. In contrast, the Ruddlesden-Popper 2D perovskites, $(RNH_3)_2A_{n-1}Pb_nX_{3n+1}$, can be viewed as *n* layers of $[PbX_6]^{4-}$ octahedra and *n*-1 layers of small organic cations sandwiched between two layers of large organic cations. Since the large organic cations control the electronic coupling between these octahedra layers, the 2D perovskites naturally form multiple-quantum-well structures, which enable new and tailorable physical properties for 2D perovskites in comparison to their 3D counterparts.[9, 10]

It is widely recognized that metal halide perovskites show both electronic and ionic conductivity,[11-13] and their role as mixed ionic/electronic conductors has been invoked to explain many phenomena in perovskite-based materials and devices, such as current-voltage hysteresis,[14-16] the switchable photovoltaic effect,[17] and device degradation.[16, 18] It is thus important to understand the ionic transport process in hopes of mitigating (or utilizing) those phenomena. While ionic transport in 3D perovskites has been well explored through both experimental and theoretical studies,[19-24] such ionic transport processes in 2D perovskites are comparatively less understood. Indeed, while Huang and co-workers have reported that 2D perovskites show no detectable ion transport compared to 3D perovskites,[25, 26] Ren and co-workers reported ion transport in exfoliated

2D PEA_2PbI_4 and PEA_2PbBr_4 (n=1) perovskite single crystals based on field effect transistors and resistive memory devices, respectively.[27, 28] More recently, AFM studies have attempted to understand this question at the local level. We showed that time-resolved scanning Kelvin probe microscopy reveals slow timescale variations that might be consistent with ion motion or trap-mediated charge motion.[29] Marohn and coworkers showed via time-resolved electrostatic force and "phase-kick" electrostatic force microscopy that the light induced conductivity in 2D BA_2PbI_4 (n=1) recovers five orders of magnitude faster than that in 3D perovskite systems, suggesting that there is little clear indication of light-induced vacancy formation in 2D BA_2PbI_4 (n=1) compared to 3D perovskites.[30]

2.3 Results and Discussion

Herein, we use frequency-modulated scanning Kelvin probe microscopy (SKPM) to study field-induced charge motion in 2D lead halide perovskite films on lateral junction devices. Importantly, we use a thick insulating layer to block electronic charge injection and therefore better isolate the effects of ionic motion from the effects of injected charges.[31, 32] We focus on two different kinds of 2D perovskite films, the prototypical two-dimensional *n*-butylammonium lead iodide perovskite (BA_2PbI_4, n=1), and the methylammonium-incorporated quasi-two-dimensional perovskite ($BA_2MA_3Pb_4I_{13}$, ~<n>=4) both in the dark and under illumination. We find that the time-dependent potential behavior differs between BA_2PbI_4 and $BA_2MA_3Pb_4I_{13}$ perovskite films. For pure 2D BA_2PbI_4 (n=1) perovskite films, we observe similar symmetric potential profiles both in the dark and under illumination, while for quasi-2D (~<n>=4) $BA_2MA_3Pb_4I_{13}$ perovskite films, we observe asymmetric potential profiles during both the charging and discharging processes in the dark, with large initial potential drops at the anode during the charging process and with large residual potential at the cathode during the discharging process. The asymmetric potential profile

gradually becomes symmetric as the illumination intensity increases during both the charging and discharging process. We propose that these observations are related to the background electronic carrier population difference, and that the ion migration in 2D BA_2PbI_4 (n=1) perovskites results primarily from halide/halide vacancy migration, while ion migration in $BA_2MA_3Pb_4I_{13}$ (~<n>=4) occurs through both halide and methylammonium (vacancy) migrations. Finally, we measure the relaxation of the bias-induced ionic charge distributions at different temperatures and extract the activation energies associated with the ionic motion in each case, which supports our proposed mechanism.

Figure 2.1a-b shows the geometry of the lateral junctions, comprising stacks of glass/perovskite/PMMA/SiO_x/Au. Here we chose an insulating stack, e.g. the PMMA/SiO_x, which perform better than either the polymer or the SiO_x layer alone, to prevent injected charges from affecting the resulting ionic motion behavior and preserve the semiconductor properties (e.g. photoluminescence).[31, 32] The as-fabricated BA_2PbI_4 (n=1) and $BA_2MA_3Pb_4I_{13}$ (~<n>=4) perovskite film qualities are characterized and displayed in **Appendix A** as **Figures S1-3**. When an external bias is applied across the junction, both the electronic and ionic charges will migrate due to the resulting electric field, leading to changes in the surface potential. Such potential changes can be detected dynamically via SKPM and are recorded here as V_{tip}, the experimental bias applied to the tip to nullify the contact potential difference *(see SI for SKPM details)*. We note that all the potential curves displayed in this study refer to V_{tip}, unless otherwise stated.

For the BA_2PbI_4 (n=1) perovskite devices, during the charging process (**Figure 2.1a**), an external electric field is applied to the microscale lateral junction by biasing one electrode with +9 V and grounding the other one. The resulting potential profiles as measured by SKPM are shown in **Figure 2.1c**. As expected, we observe two stable, flat potential plateaus on either side of the

junction where the Au contacts are, and the potential difference between the anode and cathode is 9 V. The potential profiles within the two electrodes refer to the local surface potential at that point on the perovskite films, which should be a combined result of the external bias, and the local, electronic and ionic charges (both mobile and trapped), as well as surface dipoles. When the external bias is first applied (the dark purple line), we observe a symmetrical screening of the applied potential at both sides of the junction at the initial stage within the response time of the measurement (~ seconds). We expect the potential drop at both edges, i.e. the extent of the potential screening at early times, depends on the mobile electronic carrier density, as confirmed by drift-diffusion simulation (**Appendix A Figure S4a**). Somewhat surprisingly, the potential then evolves into a stable dielectric-like behavior with a uniform drop across the whole junction (the dark red line), a process which takes ~300 seconds to finish. Since electronic carriers are able to drift on a timescale orders of magnitude faster than ionic carriers, we propose that the time evolution behavior can be viewed as two time-separated processes. First the fast migration of the free electronic carriers, and second, the migration/reaction of the ionic carriers under the net field resulting from the applied electric field and the electric field of poled electronic carriers. A more detailed discussion is provided in supporting information (**Appendix A Section 2.5 and Figure S5**): a key result is that the experimentally measured potential and field profile after *removing* the bias matches almost exactly the difference between the early and long time potential profiles obtained under bias. Consistent with this hypothesis, less ionic charge is stored for shorter poling periods (**Appendix A Figure S6**). The exact nature of the chemical reactions that are likely during the ion charging process requires further investigation. Here, we focus our analysis on the difference in the slow discharging recovery dynamics of the perovskites as a function of dimensionality and temperature.

During the discharging process, as shown in **Figure 2.1b**, we remove the external bias, ground both electrodes, and measure the potential profile immediately. The as-obtained potential profiles are shown in **Figure 2.1d**, by assuming the contact potential difference between the tip and gold electrode as zero (as they are grounded together). Two obvious peaks of opposite sign and similar magnitude of around ~1 V are observed within the junction (the dark purple line). This potential profile then gradually evolves back to a flat plateau (the dark red line). We also plot this evolution of the potential as a function of time in a 2D map, as shown in **Figure 2.1e**, which shows that whole discharging process also takes ~300 seconds to finish.

In contrast, **Figure 2.1f** shows that, when measuring the $BA_2MA_3Pb_4I_{13}$ (~<*n*>=4) perovskite devices in the dark, the initial potential screening at both sides of the junction during the charging process is *asymmetric* (the dark purple line), with a larger initial potential drop at the *anode* side. We propose, and qualitatively confirm via drift-diffusion simulations (**Appendix A Figure S4b**), that such an asymmetric potential drop would be consistent with p-doping of the $BA_2MA_3Pb_4I_{13}$ (~<*n*>=4) perovskites,[34] at a doping concentration on the order $N_A \sim 10^{15}$ cm^{-3}. In this case, the larger potential drop near the anode side is due to depleted acceptor dopants. During the discharging process, as **Figure 2.1g** shows, the potential profiles remain *asymmetric*, with a larger potential drop of around ~4 V at the cathode side in comparison to ~1 V at the anode side. **Figure 2.1h** shows the time evolution of the potential during the discharging process. We observe the potential peaks decay in intensity and shift towards the center of the junction, which suggests reversible migration of the poled charges. In this case, the discharging process takes ~200 seconds to finish.

Both samples, BA_2PbI_4 (*n*=1) and $BA_2MA_3Pb_4I_{13}$ (~<*n*>=4), show partial screening of the applied potential immediately after application of the bias (within the scan resolution of < 16 –

17s, which is the time required for each scanning trace). The timescale for the initial photoinduced charging (due to electronic charges) can be on the order of 100 μs and is not captured within the Kelvin probe time-resolution here.[29, 30] We attribute this rapid response to rapid motion of intrinsic electronic carriers in the film at early times due to unintentional doping. Clearly, there are additional slow components with relaxation timescales of hundreds of seconds.

We note that the observation of such slow, long-distance (microscale), and reversible charge migration under an applied bias contrasts with previous measurements reporting the absence of ion migration in 2D perovskites based on temperature-dependent conductivity measurements.[25, 26] We attribute our ability to measure ion motion in these junctions both because scanning probe potentiometry can measure orders of magnitude lower current densities than DC current measurements, [24, 35] and possibly because the use of injecting contacts in previous experiments may complicate the measurement of ionic charge motion, both because of the much higher density of injected electronic charge relative to background ionic charge, and because of the possibility for electrochemistry to change oxidation states of various defects.[31, 32, 36] While our data do not exclude the potential profiles are due to slower redistribution of trapped electronic carriers, we note that a trap filling and emptying process would still involve electronic carriers moving under the electric field and thus could not explain the time evolution of the potential under bias. As supported by our data and mentioned before, we propose that ion migration occurs under the net electric field resulting from the applied electric field and the electric field of poled electronic carriers.

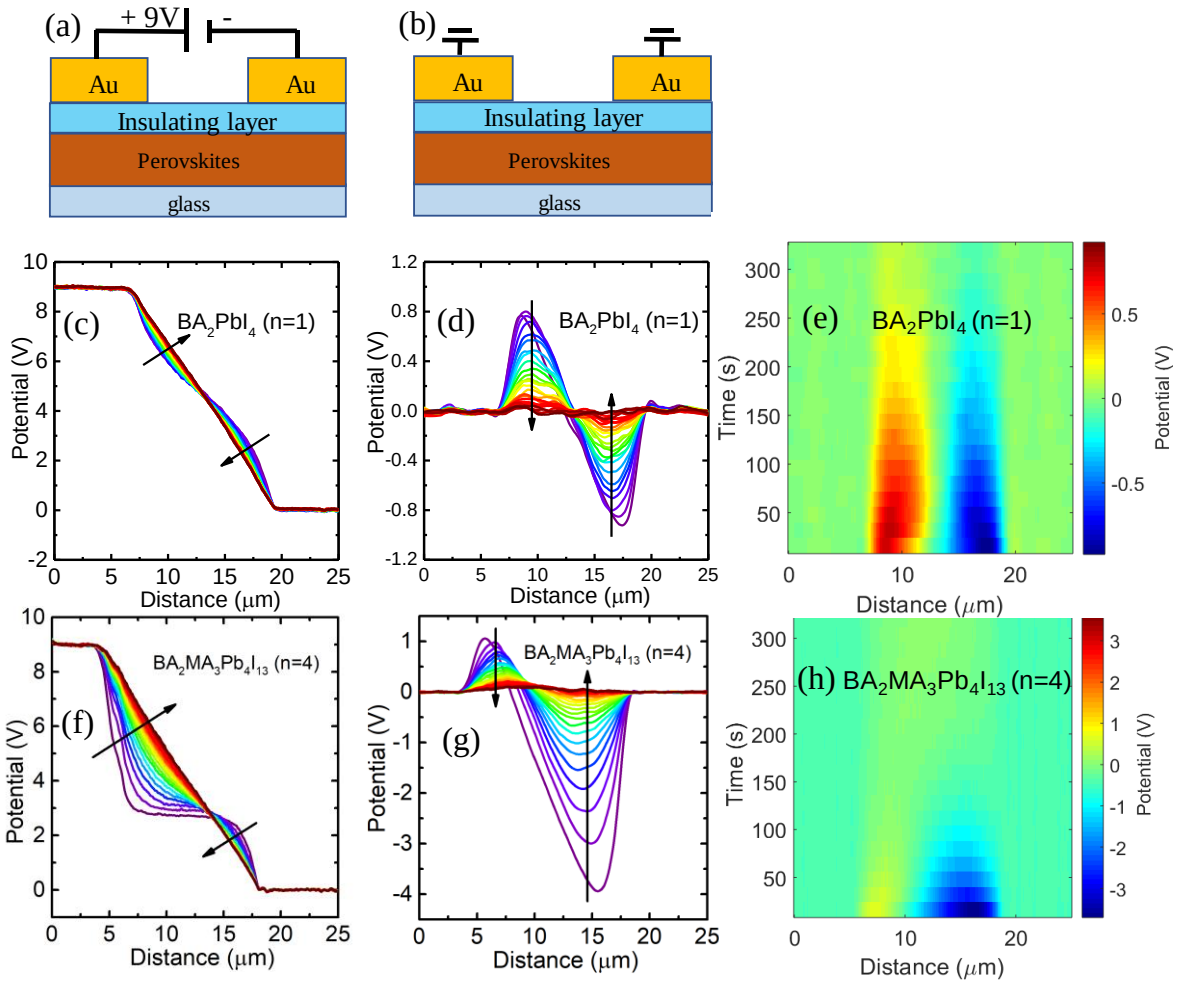

Figure 2.1. Device architectures for SKPM measurement during the (a) charging and (b) discharging process. The measured potential profiles, evolving from dark purple to dark red lines with a 16 – 17 seconds timescale for each scanning trace, during the charging process for (c) BA_2PbI_4 (n=1) and (f) $BA_2MA_3Pb_4I_{13}$ (~<n>=4) perovskite films, and during the discharging process for (d) BA_2PbI_4 (n=1) and (g) $BA_2MA_3Pb_4I_{13}$ (~<n>=4) perovskite films. The arrows in these figures indicate the evolution with respect to time. The corresponding time-resolved potential decay for (e) BA_2PbI_4 (n=1) and (h) $BA_2MA_3Pb_4I_{13}$ (~<n>=4) perovskite films during the discharging process. All of the potential profiles have been shifted so that the grounded electrode is fixed at zero (essentially removing the small contact potential difference (CPD) between the tip and the gold electrode).

Light illumination is believed to be a key factor affecting ionic motion in 3D perovskites.[37, 38] Here, we compare the time-dependent potential profile of the 2D BA_2PbI_4 (n=1) and quasi-2D $BA_2MA_3Pb_4I_{13}$ (~<n>=4) perovskite films of varying dimensionality in the dark and under light illumination using the same device architecture as shown in **Figure 2.1a-b**. **Figures 2.2a-b** compare the potential profiles during the discharging process of BA_2PbI_4 (n=1) perovskite films measured both in the dark, and with light illumination (LED with a wavelength of 455 nm and intensity of 330 W/m^2), respectively. We observe the same symmetric potential profiles for both cases, except that the peak potential values associated with the accumulated charge increase from ~1 V (in the dark) to >2 V (under light illumination).

Application of the Poisson equation allows us to extract the charge density ρ from the potential V during the discharging process.

$$\nabla^2 V(x,\ t) = \frac{-\rho(x,t)}{\varepsilon_0 \varepsilon_r} \quad (1)$$

Here ε_0 and ε_r denote respectively the permittivity of free space, and the relative static dielectric constant (we take ε_r as 6 for our BA_2PbI_4 (n=1) perovskite sample[39]). The charge densities in the dark (**Appendix A Figure S7a**) and under light illumination (**Appendix A Figure S7b**) are calculated from the potential profiles shown in **Figure 2.2a** and **Figure 2.2b**, respectively. They show accumulated negative and positive charges at the anode and cathode, respectively, each accompanied with opposite signed charges extending into the middle part of the junction. In other words, each of the two potential peaks that relaxes during the discharging process corresponds to a pair of oppositely signed charges that diffuse (and recombine) back to the equilibrium neutral condition (**Appendix A Figure S7**). The amount of charge density built up at the electrodes, at the beginning of the discharging process, increases from around ~ 2×10^{14} carriers/cm^3 in the dark to ~ 4.00×10^{14} carriers/cm^3 under 330 W/m^2 of 455-nm LED illumination. Furthermore, **Appendix**

A Figure S8 shows that both the positive and negative potential peaks increase with increasing light intensity. This enhancement of ion motion upon light illumination is consistent with previous studies in 3D perovskites.[37, 38] In 3D halide perovskites, ion migration is believed to be a defect-mediated hopping process where the hopping rate depends on the density and position of adjacent vacancies.[20, 40] Therefore, light illumination could generate more interstitial sites or vacancies, and provide more hopping opportunities for the mobile ions.[27, 37, 38]

Similarly, illumination increases the amount of mobile ionic charge we observe in quasi-2D $BA_2MA_3Pb_4I_{13}$ (~<*n*>=4) perovskites. **Figures 2.2e-f** directly compares the potential profiles of $BA_2MA_3Pb_4I_{13}$ (~<*n*>=4) perovskite films in the dark and with light illumination (LED with wavelength of 455 nm and intensity of 330 W/m^2). The results show, in the dark, that a large initial potential drop at the anode side can be observed during the charging process, as well as a large residual charge at the cathode side during the discharging process, as we have already discussed and attributed to the self p-doping behavior of the $BA_2MA_3Pb_4I_{13}$ (~<*n*>=4) films (**Figure 2.1f-g**). However, under illumination, the charging and discharging processes both become more symmetric. The light-induced symmetry change is further confirmed by varying the illumination intensity from 0 to 610 W/m^2. In **Figure 2.2i-j**, we measured the charging and discharging potential profiles at each intensity including the dark case, and then extracted the first potential line obtained upon turning on/off the applied bias. These results show that, as the light intensity increases from 0 to 64 W/m^2, the asymmetric potential profile gradually becomes more symmetric, then the potential profile remain unchanged as the light intensity further increases. As suggested by drift-diffusion simulation (**Appendix A Figure S4c**), this behavior is probably because the applied bias has been further screened by the photogenerated electronic charges under strong illumination. **Figure 2.2c-d** and 2.**2g-h** compare the discharging process as a function of time for BA_2PbI_4 (*n*=1)

and $BA_2MA_3Pb_4I_{13}$ (~<*n*>=4) perovskite films in the dark and under illumination. Again, these figures highlight the increase in density of slow mobile (ionic) species under illumination for BA_2PbI_4 (*n*=1) perovskites, and the transition from an asymmetric potential profile to a more symmetric potential profile under illumination for $BA_2MA_3Pb_4I_{13}$ (~<*n*>=4) perovskite films. We also note that all the potential profiles obtained from SKPM measurements do not show clear evidence of strong charge trapping/migration at grain boundaries, which is consistent with the results of Yun and co-authors.[24] If the grain boundaries show faster ionic transport and therefore lower resistance to ionic transport, the high-resistance (and larger) grains will dominate the total resistance of the lateral transport path and the small lateral grain boundaries will be invisible in lateral SKPM. We also note that we observe similar ion migration behavior based on devices that use a PMMA layer with different thicknesses; similarly, replacing PMMA with polystyrene (PS) results in a similar ion migration behavior, as shown in **Appendix A Figure S9**.

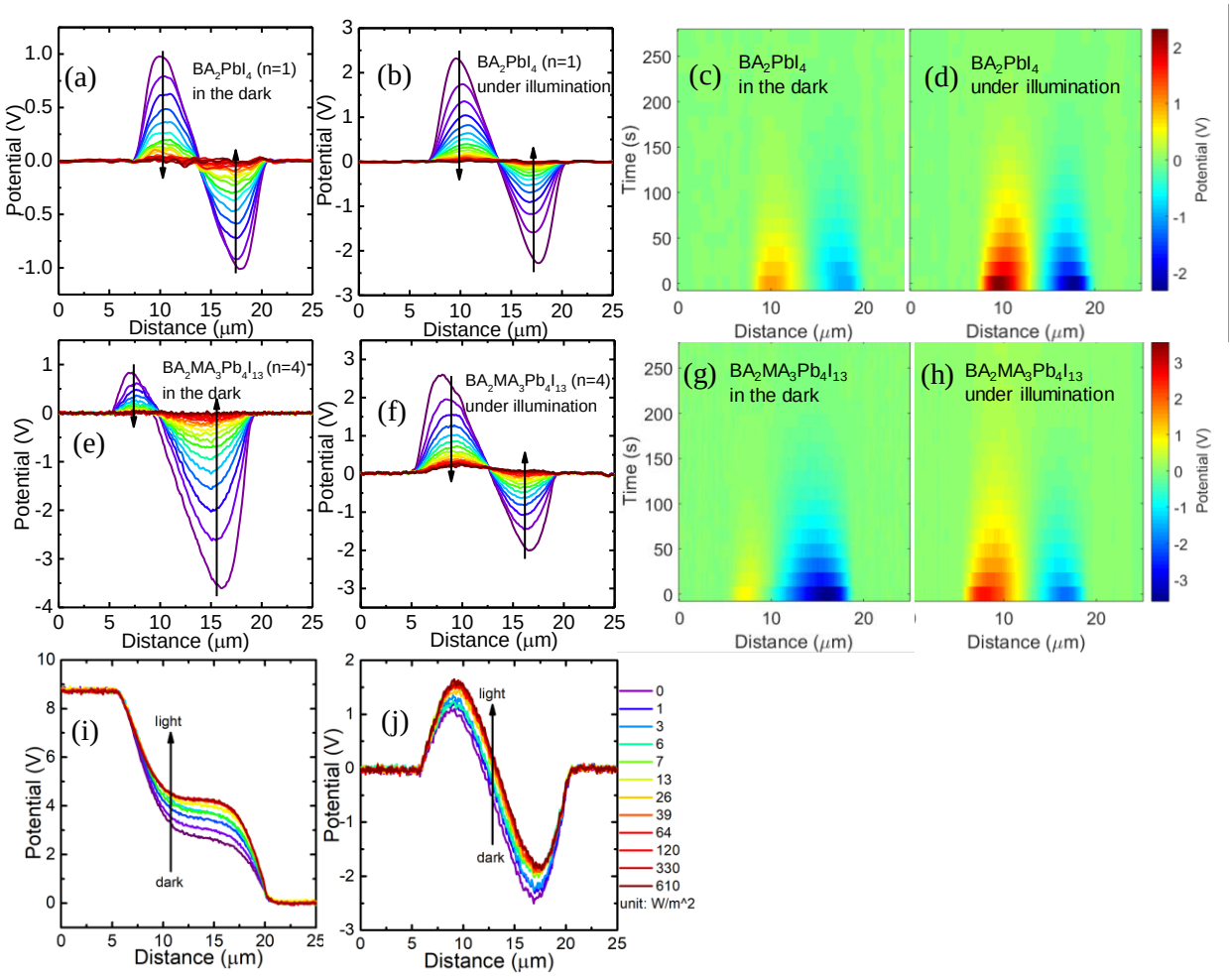

Figure 2.2. Potential profiles, evolving from dark purple to dark red lines with a 16 – 17 seconds timescale for each scanning trace, during the discharging process for BA_2PbI_4 (n=1) perovskite films (a) in the dark and (b) under illumination (455 nm, 330 W/m^2), and the corresponding time resolved potential decay (c) in the dark and (d) under illumination; The potential profiles during the discharging process for $BA_2MA_3Pb_4I_{13}$ (~<n>=4) perovskite films (e) in the dark and (f) under illumination, and the corresponding time resolved potential decay (g) in the dark and (h) under illumination. Potential profiles, evolving from dark purple lines to dark red lines as light illumination intensity increases, for $BA_2MA_3Pb_4I_{13}$ (~<n>=4) based devices during the (i) charging and (j) discharging process under illumination with different intensities. All the lines shown in (i-

j) are the extracted first potential lines after turning on/off the bias. All of the potential profiles have been shifted so that the grounded electrode is fixed at zero (essentially removing the small CPD between the tip and the gold electrode).

Speculating as to the origin of these phenomena, we propose that the ion motion in purely 2D BA_2PbI_4 perovskite films is dominated by paired halide and halide vacancy motion, whereas for quasi-2D $BA_2MA_3Pb_4I_{13}$ films, the ion motion is a combination of two paired charges, i.e. halide and its vacancy and another one (perhaps methylammonium and its vacancy). The proposed paired ion/vacancy motion involves ions taking up the position of vacancies as they migrate through the perovskite lattice. So as ions are driven by the electric field in one direction, vacancies move in the opposite direction. During the discharging process, we propose that the ions and vacancies recombine/annihilate resulting in the decrease of the accumulated surface potential over time.

To better test this hypothesis, we measured the relaxation of the bias-induced charge distributions at different temperatures for both BA_2PbI_4 (n=1) and $BA_2MA_3Pb_4I_{13}$ (~<n>=4) perovskite films. According to our hypothesis, there should be a single dominant paired species, hence single temperature dependence for BA_2PbI_4 (n=1) perovskite, whereas the $BA_2MA_3Pb_4I_{13}$ (~<n>=4) films should exhibit different temperature dependences for the positive and negative potential relaxations. In addition, the change in the decay dynamics under illumination are also expected to be symmetrical for BA_2PbI_4 (n=1) films but asymmetrical for $BA_2MA_3Pb_4I_{13}$ (~<n>=4) films.

Figures 2.3a and **2.3b** compare the decays of the potential profiles after bias is removed for BA_2PbI_4 (n=1) perovskite films at different temperatures in the dark and under light illumination. **Figure 2.3c** and 2.**3d** compare the decays for $BA_2MA_3Pb_4I_{13}$ (~<n>=4) perovskite

films at different temperatures in the dark and under light illumination. As we can see, at all temperatures ranging from 283 K to 313 K, BA_2PbI_4 (*n*=1) perovskite films (**Figure 2.3a-b**) display symmetric potential decays both in the dark and under illumination, with increasing magnitudes under illumination. In contrast, at all measured temperatures, $BA_2MA_3Pb_4I_{13}$ (~<*n*>=4) perovskite samples show asymmetric potential profiles in the dark, which become more symmetric under illumination. Notably, the ion motion is strongly temperature dependent, even over the relatively modest temperature range from 283 K to 313 K, with the potential decay rate (ion motion) increasing as the temperature increases.

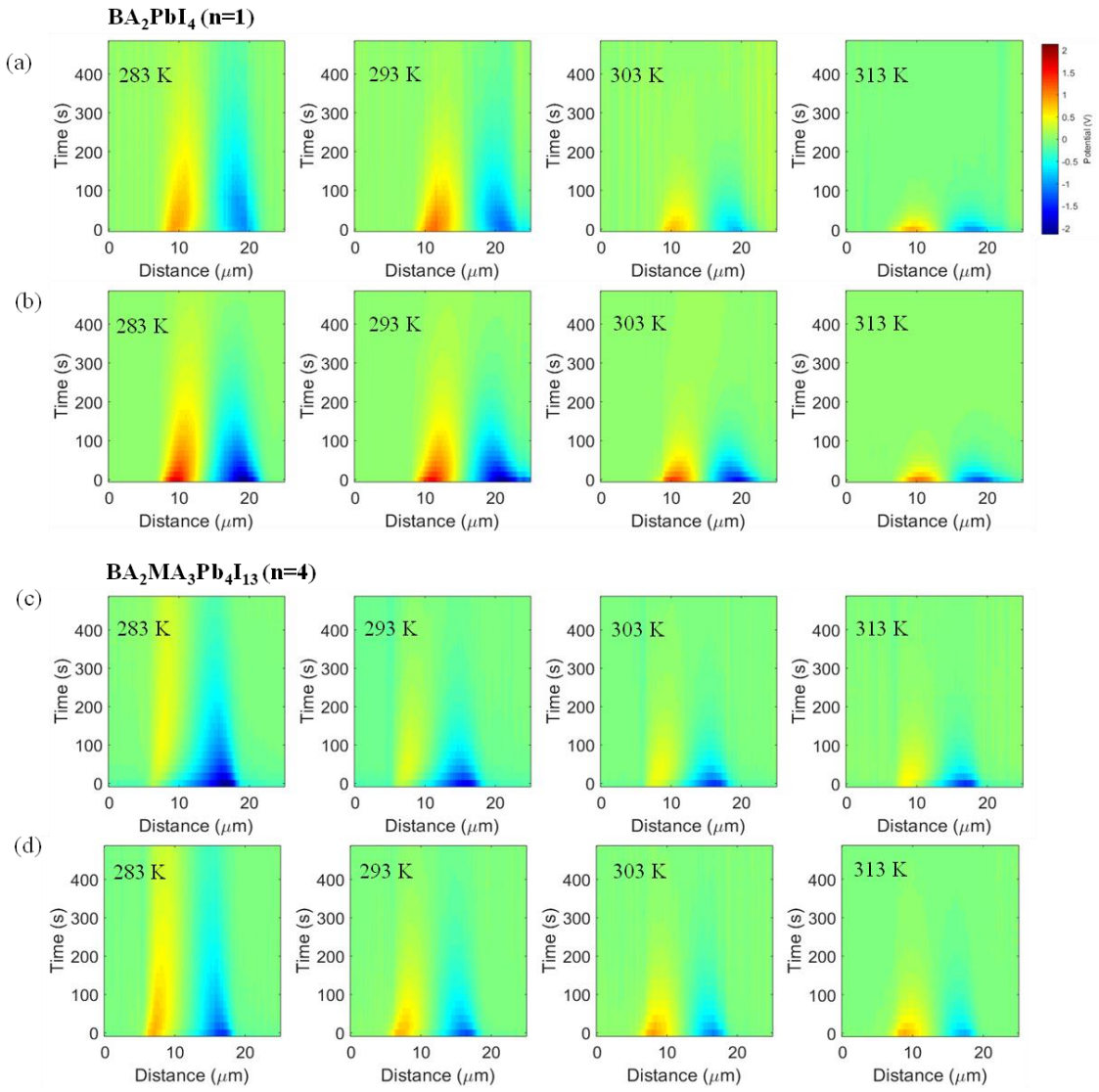

Figure 2.3. Time resolved potential decays at temperatures of 283, 293, 303 and 313 K for BA_2PbI_4 (*n*=1) perovskite films (a) in the dark and (b) under light illumination, and for $BA_2MA_3Pb_4I_{13}$ (~<*n*>=4) perovskite films (c) in the dark and (d) under light illumination during the discharging process.

The temperature-dependent relaxation of the bias-induced ionic charge distributions allows us to estimate the activation energies associated with the charge motion in each case. We track the decay of the migrating ionic species by extracting the amplitude of both the negative and positive potential peaks at each time step and fit the decay curves with exponential functions to obtain the decay rates for the two charge pairs at each temperature (See **Appendix A Figure S10-11** for fits). We fit the decay rates against the temperature to extract activation energies with the Arrhenius equation:

$$\lambda = A * e^{-\frac{E_a}{k_b T}} \quad (2)$$

using non-linear least squares orthogonal distance regression as described in the SI. In equation 2, λ, E_a, T, k_b and A refer to the decay rate, activation energy, temperature, Boltzmann constant and a prefactor respectively. The Arrhenius fittings shown by plotting the log of the decay rate versus the inverse temperature are displayed in **Figure 2.4a-d**. From these fits, we obtain activation energies associated with the ionic motion in each case, as plotted in **Appendix A Figure S12** and summarized in **Table 2.1**.

For the BA_2PbI_4 (*n*=1) perovskite samples, the activation energies E_a of negative and positive potential peaks in the dark are best fit to be 0.61 ± 0.07 eV and 0.55 ± 0.05 eV, respectively, which decrease to 0.37 ± 0.05 eV and 0.30 ± 0.08 eV, respectively, under light illumination. In both cases, the activation energy for the positive and negative potential peaks are within one standard error of each other, consistent with our hypothesis that ion migration is

dominated by paired halide and halide vacancy motion. The light-induced decrease of activation energies is qualitatively consistent with previous reports of light-activated ion migration[37, 38] and light-activated halide vacancy formation[41, 42] in 3D perovskites, suggesting that similar light-activated processes occur in 2D perovskites.

In contrast, the $BA_2MA_3Pb_4I_{13}$ (~<*n*>=4) perovskite samples show a more complex temperature dependence. We observe asymmetric potential decay for the positive and negative potential peaks in $BA_2MA_3Pb_4I_{14}$ (~<*n*>=4) films (**Appendix A Figure S11**); this difference in decay rate is maintained under illumination even though the potential profile becomes more symmetric. The best fit E_a corresponding to the negative potential in the dark are calculated to be 0.64 ± 0.15 eV, which change to 0.39 ± 0.07 eV under light illumination. Both activation energies are similar to that of the BA_2PbI_4 (*n*=1) film, suggesting the charge pair associated with the negative potential is related to halide and its vacancy. This is consistent with this charge pair being located at the hole-accumulating electrode and the theory that holes promote the formation of neutral iodine interstitial formation.[33] On the other hand, the best fit E_a corresponding to positive potential in the dark and under illumination are similar, 0.24 ± 0.07 eV and 0.25 ± 0.10 eV, respectively.

These results are broadly consistent with the expectations from our hypothesis above: both the positive and negative potentials for the BA_2PbI_4 (*n*=1) films result from a same ionic charge pair, thus exhibiting a similar temperature dependence; while the negative potential and associated charge pair for $BA_2MA_3Pb_4I_{13}$ (~<*n*>=4) films show a similar temperature dependence (common origin and transport mechanism) with the BA_2PbI_4 (*n*=1) films, the positive potential and associated charge pair exhibits distinctly different temperature dependence and light dependence

and therefore suggests a different chemical origin, which we tentatively attribute to the methylammonium ions and vacancies.

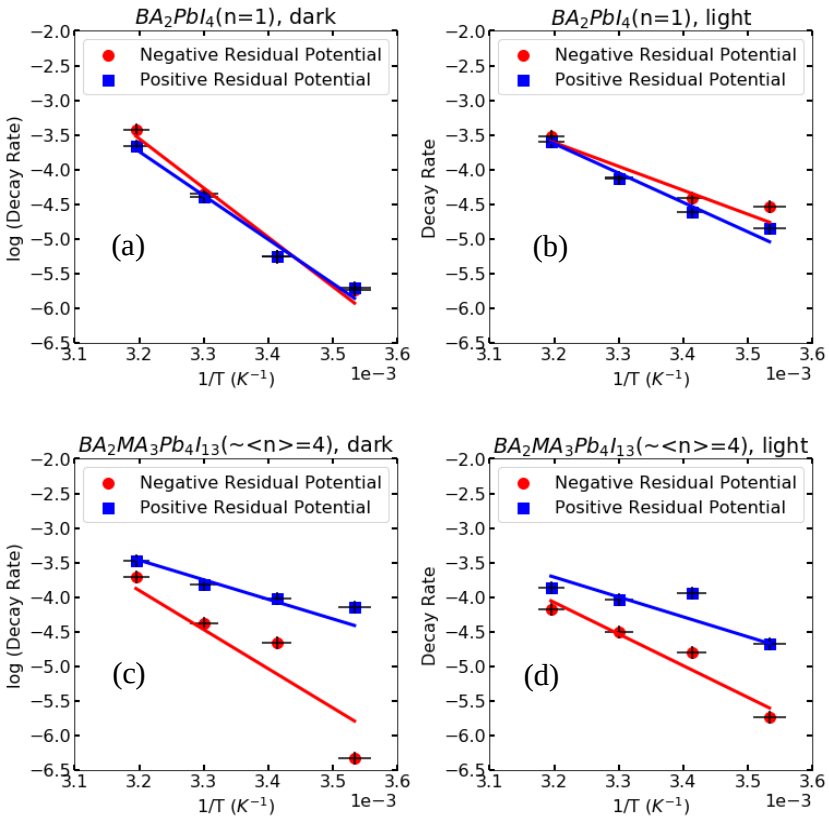

Figure 2.4. Arrhenius plots showing the temperature dependence of the decay rate for BA_2PbI_4 (*n*=1) perovskite films (a) in the dark and (b) under light illumination, and for $BA_2MA_3Pb_4I_{13}$ (~<*n*>=4) perovskite films (c) in the dark and (d) under light illumination. The solid lines indicate the fitted line used to calculate activation energies and the error bars represent one standard deviation in the uncertainty of the fit parameters as determined in SI.

Table 2.1. Activation energies E_a of negative and positive potentials for BA_2PbI_4 (n=1) and $BA_2MA_3Pb_4I_{13}$ (~<n>=4) perovskite films in the dark and under light illumination as determined by fitting temperature-dependent-potential curves.

Conditions	E_a (eV)
BA_2PbI_4 (n=1), dark, negative potential	0.61 ± 0.07
BA_2PbI_4 (n=1), dark, positive potential	0.55 ± 0.05
BA_2PbI_4 (n=1), light, negative potential	0.37 ± 0.05
BA_2PbI_4 (n=1), light, positive potential	0.30 ± 0.08
$BA_2MA_3Pb_4I_{13}$ (n=1), dark, negative potential	0.64 ± 0.15
$BA_2MA_3Pb_4I_{13}$ (n=1), dark, positive potential	0.24 ± 0.07
$BA_2MA_3Pb_4I_{13}$ (n=1), light, negative potential	0.39 ± 0.07
$BA_2MA_3Pb_4I_{13}$ (n=1), light, positive potential	0.25 ± 0.10

2.4 Conclusions

In summary, we perform SKPM measurement on micron-scale lateral junctions in the absence of charge injection in order to study ion motion in prototypical 2D BA_2PbI_4 (n=1) perovskite films, and methylammonium-incorporated quasi-2D $BA_2MA_3Pb_4I_{13}$ (~<n>=4) perovskite films, as functions of both light illumination and temperature. We show that these two films show differently-shape potential profiles during the charging process, which we attribute to a difference in their background electronic carrier population, as well as the carrier redistribution due to photogeneration. Furthermore, we observe that the relaxation dynamics differ between BA_2PbI_4 (n=1) and $BA_2MA_3Pb_4I_{13}$ (~<n>=4) films. We explain these phenomena by proposing that the ion motion in pure 2D BA_2PbI_4 (n=1) perovskites could be dominated by paired halide

and halide vacancy motion, whereas for methylammonium-incorporated quasi-2D $BA_2MA_3Pb_4I_{13}$ (~$\langle n \rangle$=4) perovskite films, the ion motion results from the interplay between paired halide/vacancy and methylammonium/vacancy. In contrast to earlier reports, these results indicate that, just as in 3D perovskites, ion transport can and does take place, although dimensionality clearly affects the character of both electronic and ionic transport in 2D perovskites. These results provide a basis for understanding bias-, illumination-, and temperature-dependent ion motion in 2D perovskites that can be used to improve the performance and stability of perovskite-based optoelectronic devices.

2.5 Acknowledgments

This paper is primarily based on work sponsored by the Department of Energy (DOE-SC0013957). We acknowledge support by the State of Washington through the University of Washington Clean Energy Institute and the Washington Research Foundation for supporting student fellowships and instrumentation. Part of this work was conducted at the Molecular Analysis Facility, a National Nanotechnology Coordinated Infrastructure site at the University of Washington that is supported in part by the National Science Foundation (grant no. ECC-1542101), the University of Washington, the Molecular Engineering & Sciences Institute, the Clean Energy Institute and the National Institutes of Health. F.J. was additionally supported by the program of China Scholarship Council, F.M. was additionally supported by the German Academic Exchange Service (DAAD) with funds from the German Federal Ministry of Education and Research (BMBF) and the European Union (FP7-PEOPLE-2013-COFUND - grant agreement No. 605728), and J.W acknowledges postdoctoral fellowship support from the Washington Research Foundation and the Mistletoe foundation.

2.6 References

(1) Smith, I. C.; Hoke, E. T.; Solis-Ibarra, D.; McGehee, M. D.; Karunadasa, H. I., A Layered Hybrid Perovskite Solar-Cell Absorber with Enhanced Moisture Stability. *Angew. Chem. Int. Ed.* **2014**, 53, 11232-11235.

(2) Tsai, H.; Nie, W.; Blancon, J. C.; Stoumpos, C. C.; Asadpour, R.; Harutyunyan, B.; Neukirch, A. J.; Verduzco, R.; Crochet, J. J.; Tretiak, S.; Pedesseau, L.; Even, J.; Alam, M. A.; Gupta, G.; Lou, J.; Ajayan, P. M.; Bedzyk, M. J.; Kanatzidis, M. G., High-Efficiency Two-Dimensional Ruddlesden-Popper Perovskite Solar Cells. *Nature* **2016**, 536, 312-316.

(3) Liao, Y.; Liu, H.; Zhou, W.; Yang, D.; Shang, Y.; Shi, Z.; Li, B.; Jiang, X.; Zhang, L.; Quan, L. N.; Quintero-Bermudez, R.; Sutherland, B. R.; Mi, Q.; Sargent, E. H.; Ning, Z., Highly Oriented Low-Dimensional Tin Halide Perovskites with Enhanced Stability and Photovoltaic Performance. *J. Am. Chem. Soc.* **2017**, 139, 6693-6699.

(4) Zhang, X.; Ren, X.; Liu, B.; Munir, R.; Zhu, X.; Yang, D.; Li, J.; Liu, Y.; Smilgies, D.-M.; Li, R.; Yang, Z.; Niu, T.; Wang, X.; Amassian, A.; Zhao, K.; Liu, S., Stable High Efficiency Two-Dimensional Perovskite Solar Cells Via Cesium Doping. *Energy Environ. Sci.* **2017**, 10, 2095-2102.

(5) Fu, W.; Wang, J.; Zuo, L.; Gao, K.; Liu, F.; Ginger, D. S.; Jen, A. K. Y., Two-Dimensional Perovskite Solar Cells with 14.1% Power Conversion Efficiency and 0.68% External Radiative Efficiency. *ACS Energy Lett.* **2018**, 3, 2086-2093.

(6) Chen, Y.; Sun, Y.; Peng, J.; Tang, J.; Zheng, K.; Liang, Z., 2d Ruddlesden–Popper Perovskites for Optoelectronics. *Adv. Mater.* **2018**, 30, 1703487.

(7) Liu, T.; Jiang, Y.; Qin, M.; Liu, J.; Sun, L.; Qin, F.; Hu, L.; Xiong, S.; Jiang, X.; Jiang, F.; Peng, P.; Jin, S.; Lu, X.; Zhou, Y., Tailoring Vertical Phase Distribution of Quasi-Two-Dimensional Perovskite Films Via Surface Modification of Hole-Transporting Layer. *Nat. Commun.* **2019**, 10, 878.

(8) Zhang, F.; Lu, H.; Tong, J.; Berry, J. J.; Beard, M. C.; Zhu, K., Advances in Two-Dimensional Organic–Inorganic Hybrid Perovskites. *Energy Environ. Sci.* **2020**, 13, 1154-1186.

(9) Cheng, L.; Jiang, T.; Cao, Y.; Yi, C.; Wang, N.; Huang, W.; Wang, J., Multiple-Quantum-Well Perovskites for High-Performance Light-Emitting Diodes. *Adv. Mater.* **2020**, 32, 1904163.

(10) Sun, Y.; Zhang, L.; Wang, N.; Zhang, S.; Cao, Y.; Miao, Y.; Xu, M.; Zhang, H.; Li, H.; Yi, C.; Wang, J.; Huang, W., The Formation of Perovskite Multiple Quantum Well Structures for High Performance Light-Emitting Diodes. *npj Flex. Electron.* **2018**, 2, 12.

(11) Yang, T.-Y.; Gregori, G.; Pellet, N.; Grätzel, M.; Maier, J., The Significance of Ion Conduction in a Hybrid Organic–Inorganic Lead-Iodide-Based Perovskite Photosensitizer. *Angew. Chem. Int. Ed.* **2015**, 54, 7905-7910.

(12) Senocrate, A.; Moudrakovski, I.; Kim, G. Y.; Yang, T.-Y.; Gregori, G.; Grätzel, M.; Maier, J., The Nature of Ion Conduction in Methylammonium Lead Iodide: A Multimethod Approach. *Angew. Chem. Int. Ed.* **2017**, 56, 7755-7759.

(13) Kerner, R. A.; Rand, B. P., Ionic–Electronic Ambipolar Transport in Metal Halide Perovskites: Can Electronic Conductivity Limit Ionic Diffusion? *J. Phys. Chem. Lett.* **2018**, 9, 132-137.

(14) Snaith, H. J.; Abate, A.; Ball, J. M.; Eperon, G. E.; Leijtens, T.; Noel, N. K.; Stranks, S. D.; Wang, J. T.-W.; Wojciechowski, K.; Zhang, W., Anomalous Hysteresis in Perovskite Solar Cells. *J. Phys. Chem. Lett.* **2014**, 5, 1511-1515.

(15) Zhang, T.; Chen, H.; Bai, Y.; Xiao, S.; Zhu, L.; Hu, C.; Xue, Q.; Yang, S., Understanding the Relationship between Ion Migration and the Anomalous Hysteresis in High-Efficiency Perovskite Solar Cells: A Fresh Perspective from Halide Substitution. *Nano Energy* **2016**, 26, 620-630.

(16) Miyano, K.; Yanagida, M.; Tripathi, N.; Shirai, Y., Hysteresis, Stability, and Ion Migration in Lead Halide Perovskite Photovoltaics. *J. Phys. Chem. Lett.* **2016**, 7, 2240-2245.

(17) Xiao, Z.; Yuan, Y.; Shao, Y.; Wang, Q.; Dong, Q.; Bi, C.; Sharma, P.; Gruverman, A.; Huang, J., Giant Switchable Photovoltaic Effect in Organometal Trihalide Perovskite Devices. *Nat. Mater.* **2015**, 14, 193-198.

(18) Boyd, C. C.; Cheacharoen, R.; Leijtens, T.; McGehee, M. D., Understanding Degradation Mechanisms and Improving Stability of Perovskite Photovoltaics. *Chem. Rev.* **2019**, 119, 3418-3451.

(19) Yuan, Y.; Huang, J., Ion Migration in Organometal Trihalide Perovskite and Its Impact on Photovoltaic Efficiency and Stability. *Acc. Chem. Res.* **2016**, 49, 286-293.

(20) Walsh, A.; Stranks, S. D., Taking Control of Ion Transport in Halide Perovskite Solar Cells. *ACS Energy Lett.* **2018**, 3, 1983-1990.

(21) Calado, P.; Telford, A. M.; Bryant, D.; Li, X.; Nelson, J.; O'Regan, B. C.; Barnes, P. R., Evidence for Ion Migration in Hybrid Perovskite Solar Cells with Minimal Hysteresis. *Nat. Commun.* **2016**, 7, 13831.

(22) Lan, D., The Physics of Ion Migration in Perovskite Solar Cells: Insights into Hysteresis, Device Performance, and Characterization. *Prog. Photovolt.* **2020**, 28, 533-537.

(23) Haruyama, J.; Sodeyama, K.; Han, L.; Tateyama, Y., First-Principles Study of Ion Diffusion in Perovskite Solar Cell Sensitizers. *J. Am. Chem. Soc.* **2015**, 137, 10048-10051.

(24) Yun, J. S.; Seidel, J.; Kim, J.; Soufiani, A. M.; Huang, S.; Lau, J.; Jeon, N. J.; Seok, S. I.; Green, M. A.; Ho-Baillie, A., Critical Role of Grain Boundaries for Ion Migration in Formamidinium and Methylammonium Lead Halide Perovskite Solar Cells. *Adv. Energy Mater.* **2016**, 6, 1600330.

(25) Lin, Y.; Bai, Y.; Fang, Y.; Wang, Q.; Deng, Y.; Huang, J., Suppressed Ion Migration in Low-Dimensional Perovskites. *ACS Energy Lett.* **2017**, 2, 1571-1572.

(26) Xiao, X.; Dai, J.; Fang, Y.; Zhao, J.; Zheng, X.; Tang, S.; Rudd, P. N.; Zeng, X. C.; Huang, J., Suppressed Ion Migration Along the in-Plane Direction in Layered Perovskites. *ACS Energy Lett.* **2018**, 3, 684-688.

(27) Li, Y.-T.; Ding, L.; Li, J.-Z.; Kang, J.; Li, D.-H.; Ren, L.; Ju, Z.-Y.; Sun, M.-X.; Ma, J.-Q.; Tian, Y.; Gou, G.-Y.; Xie, D.; Tian, H.; Yang, Y.; Wang, L.-W.; Peng, L.-M.; Ren, T.-L., Light-Enhanced Ion Migration in Two-Dimensional Perovskite Single Crystals Revealed in Carbon Nanotubes/Two-Dimensional Perovskite Heterostructure and Its Photomemory Application. *ACS Cent. Sci* **2019**, 5, 1857-1865.

(28) Tian, H.; Zhao, L.; Wang, X.; Yeh, Y.-W.; Yao, N.; Rand, B. P.; Ren, T.-L., Extremely Low Operating Current Resistive Memory Based on Exfoliated 2d Perovskite Single Crystals for Neuromorphic Computing. *ACS Nano* **2017**, 11, 12247-12256.

(29) Giridharagopal, R.; Precht, J. T.; Jariwala, S.; Collins, L.; Jesse, S.; Kalinin, S. V.; Ginger, D. S., Time-Resolved Electrical Scanning Probe Microscopy of Layered Perovskites Reveals Spatial Variations in Photoinduced Ionic and Electronic Carrier Motion. *ACS Nano* **2019**, 13, 2812-2821.

(30) Tirmzi, A. M.; Dwyer, R. P.; Jiang, F.; Marohn, J. A., Light-Dependent Impedance Spectra and Transient Photoconductivity in a Ruddlesden–Popper 2d Lead–Halide Perovskite Revealed by Electrical Scanned Probe Microscopy and Accompanying Theory. *J. Phys. Chem. C* **2020**, 124, 13639-13648.

(31) Birkhold, S. T.; Precht, J. T.; Liu, H.; Giridharagopal, R.; Eperon, G. E.; Schmidt-Mende, L.; Li, X.; Ginger, D. S., Interplay of Mobile Ions and Injected Carriers Creates Recombination Centers in Metal Halide Perovskites under Bias. *ACS Energy Lett.* **2018**, 3, 1279-1286.

(32) Birkhold, S. T.; Precht, J. T.; Giridharagopal, R.; Eperon, G. E.; Schmidt-Mende, L.; Ginger, D. S., Direct Observation and Quantitative Analysis of Mobile Frenkel Defects in Metal Halide Perovskites Using Scanning Kelvin Probe Microscopy. *J. Phys. Chem. C* **2018**, 122, 12633-12639.

(33) Kim, G. Y.; Senocrate, A.; Yang, T.-Y.; Gregori, G.; Grätzel, M.; Maier, J., Large Tunable Photoeffect on Ion Conduction in Halide Perovskites and Implications for Photodecomposition. *Nat. Mater.* **2018**, 17, 445-449.

(34) Peng, W.; Yin, J.; Ho, K.-T.; Ouellette, O.; De Bastiani, M.; Murali, B.; El Tall, O.; Shen, C.; Miao, X.; Pan, J.; Alarousu, E.; He, J.-H.; Ooi, B. S.; Mohammed, O. F.; Sargent, E.; Bakr, O. M., Ultralow Self-Doping in Two-Dimensional Hybrid Perovskite Single Crystals. *Nano Lett.* **2017**, 17, 4759-4767.

(35) Giridharagopal, R.; Cox, P. A.; Ginger, D. S., Functional Scanning Probe Imaging of Nanostructured Solar Energy Materials. *Acc. Chem. Res.* **2016**, 49, 1769-1776.

(36) Kerner, R. A.; Schulz, P.; Christians, J. A.; Dunfield, S. P.; Dou, B.; Zhao, L.; Teeter, G.; Berry, J. J.; Rand, B. P., Reactions at Noble Metal Contacts with Methylammonium Lead Triiodide Perovskites: Role of Underpotential Deposition and Electrochemistry. *APL Mater.* **2019**, 7, 041103.

(37) Zhao, Y. C.; Zhou, W. K.; Zhou, X.; Liu, K. H.; Yu, D. P.; Zhao, Q., Quantification of Light-Enhanced Ionic Transport in Lead Iodide Perovskite Thin Films and Its Solar Cell Applications. *Light Sci. Appl.* **2017**, 6, e16243.

(38) Xing, J.; Wang, Q.; Dong, Q.; Yuan, Y.; Fang, Y.; Huang, J., Ultrafast Ion Migration in Hybrid Perovskite Polycrystalline Thin Films under Light and Suppression in Single Crystals. *Phys. Chem. Chem. Phys.* **2016**, 18, 30484-30490.

(39) Pedesseau, L.; Kepenekian, M.; Sapori, D.; Huang, Y.; Rolland, A.; Beck, A.; Cornet, C.; Durand, O.; Wang, S.; Katan, C.; Even, J., Dielectric Properties of Hybrid Perovskites and Drift-Diffusion Modeling of Perovskite Cells. *Proc. SPIE Int. Soc. Opt. Eng.* **2016**, 9743, 97430N.

(40) Eames, C.; Frost, J. M.; Barnes, P. R.; O'Regan, B. C.; Walsh, A.; Islam, M. S., Ionic Transport in Hybrid Lead Iodide Perovskite Solar Cells. *Nat. Commun.* **2015**, 6, 7497.

(41) Ruan, S.; Surmiak, M.-A.; Ruan, Y.; McMeekin, D. P.; Ebendorff-Heidepriem, H.; Cheng, Y.-B.; Lu, J.; McNeill, C. R., Light Induced Degradation in Mixed-Halide Perovskites. *J. Mater. Chem. C* **2019**, 7, 9326-9334.

(42) Li, Z.; Ji, J.; Zhang, C.; Hou, Q.; Jin, P., First-Principles Study on the Oxygen–Light-Induced Iodide Vacancy Formation in Fasni3 Perovskite. *J. Phys. Chem. C* **2020**, 124, 14147-14157.

Chapter 3: Surface Passivation Suppresses Local Ion Motion in Halide Perovskites

Adapted from Pothoof, J.; Westbrook, R.J.E.; Giridharagopal, R.; Breshears, M.D.; and Ginger, D.S. Surface Passivation Suppresses Local Ion Motion in Halide Perovskites. J. Phys. Chem. Lett. 2023, 14, 26, 6092-6098. https://doi.org/10.1021/acs.jpclett.3c01089.

3.1 Overview

We use scanning probe microscopy to study ion migration in the formamidinium (FA)-containing halide perovskite semiconductor $Cs_{0.22}FA_{0.78}Pb(I_{0.85}Br_{0.15})_3$ in the presence and absence of chemical surface passivation. We measure the evolving contact potential difference (CPD) using scanning Kelvin probe microscopy (SKPM) following voltage poling. We find that ion migration leads to a ~100 mV shift in the CPD of control films after poling with 3 V for only a few seconds. Moreover, we find that ion migration is heterogeneous, with domain interfaces leading to a larger shift in the CPD. Application of (3-aminopropyl)trimethoxysilane (APTMS) as a surface passivator further leads to 5-fold reduction in the CPD shift from ~100 mV to ~20 mV. We use hyperspectral microscopy to confirm that APTMS-treated perovskite films undergo less photoinduced halide migration than control films. We interpret these results as due to a reduction in halide vacancy concentration after APTMS passivation.

3.2 Introduction

Halide perovskite semiconductors are important materials for a range of optoelectronic applications such as photovoltaics and light-emitting devices,[1,2] and power conversion efficiencies for single-junction perovskite solar cells have increased to 25.8%.[3] One challenge facing some applications is that perovskites are prone to ion migration, in which ions move through the crystal lattice.[4,5] Ion migration reduces operational stability and can lead to undesired interactions between the perovskite active layer and transport layers or electrodes and segregation of the perovskite into separate phases.[6–11] Due to a low activation energy, vacancy-mediated halide migration is thought to be the dominant ion migration process in the perovskite lattice.[5,12] While some theoretical studies have claimed halide vacancies are not defects of concern due to their shallow energy levels within the perovskite bandgap,[13–15] many experiments have been performed using chemical passivation strategies as a method of reducing surface halide vacancies, which has resulted in increased photoluminescence quantum yields and ultimately improved device performance.[16–23] However, there are far fewer studies that examine how surface passivation affects ion migration by means other than hysteresis reduction,[24–27] especially at the local level, which may reveal the location of halide vacancies that cause ion migration.

Previous work from our group has shown that (3-aminopropyl)trimethoxysilane (APTMS) significantly reduces nonradiative recombination in halide perovskite semiconductors.[28,29] Since halide migration often involves halide vacancies,[5,12] the same sites that are often targeted by chemical surface passivation,[17,19–21,23,30–32] we hypothesize that surface passivation using the specific chemistry offered by molecules such as APTMS should also suppress halide migration.

Here, we examine this hypothesis, with a particular emphasis on investigating how APTMS surface passivation can affect ion migration *locally*, via scanning Kelvin probe microscopy (SKPM). We combine SKPM measurements on locally poled perovskite samples with studies of photoluminescence using hyperspectral photoluminescence microscopy. The use of SKPM allows us to probe ion motion and effects of APTMS surface passivation below the optical diffraction limit of conventional photoluminescence measurements.[33–35] We focus our study on wide-gap (~1.7 eV), mixed-halide perovskites because such formulations are particularly relevant for perovskite-on-silicon tandem photovoltaics and because ion migration often causes halide phase segregation in these compositions.[25,36] We find that the contact potential difference (CPD) of the perovskite samples evolves with applied electric fields. We quantify the average shift in CPD for perovskite control films to be near ~100 mV at poling extremes of +/- 3 V with a dwell time of only a few seconds, which is reduced to ~20 mV after surface passivation with APTMS. We attribute this reduction in CPD shift to the passivation of surface halide defects. Using photoluminescence hyperspectral imaging, we also observe a reduction in photoinduced halide segregation in the perovskite films after surface passivation with APTMS.

3.3 Results and Discussion

For this study, we prepared mixed-halide perovskite semiconductor films of the composition $Cs_{0.22}FA_{0.78}Pb(I_{0.85}Br_{0.15})_3$ on ITO substrates by using a one-step spin-coating technique as adapted from the literature (see Appendix B for full details).[37] We refer to these as-grown films as “control” or “unpassivated” perovskites. To prepare passivated perovskite films, we exposed the films to APTMS for five minutes at room temperature in a low-vacuum chamber as previously described.[28,29] We verified that the films had a perovskite structure using XRD

(**Appendix B Figures S1a and b**). UV-Vis absorption data is consistent with a bandgap of ~1.7 eV, confirming the target compositions of $Cs_{0.22}FA_{0.78}Pb(I_{0.85}Br_{0.15})_3$ and $Cs_{0.17}FA_{0.83}Pb(I_{0.75}Br_{0.25})_3$ (**Appendix B Figure S1c and d**). **Figure 3.1** shows that APTMS passivation lengthens the photoluminescence (PL) lifetimes and increases the PL intensity (and thus the PL quantum yield) of perovskite films, as is consistent with a reduction in the surface trap state density.

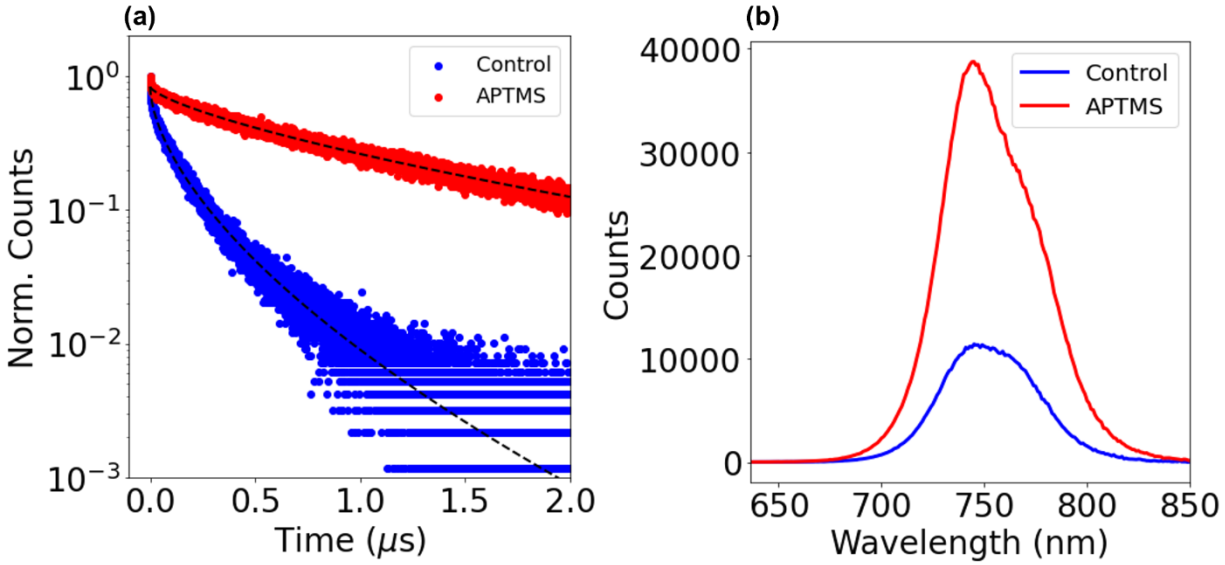

Figure 3.1. (a) Time-resolved PL measurements for $Cs_{0.22}FA_{0.78}Pb(I_{0.85}Br_{0.15})_3$ control and APTMS-passivated films deposited on glass substrates. We excited the samples with a 640 nm laser and an excitation fluence of ~3.4 nJ/cm^2. Stretched exponential fits for the decay curves are shown in black. We calculated average lifetimes of 120.78 and 1015.60 ns for control and APTMS-passivated films, respectively. (b) Steady-state PL spectra for perovskite control and APTMS-passivated films deposited on glass substrates.

In order to probe ion migration in these films at the local level, we combine local electric-field poling with SKPM to measure the evolution of the CPD following application of poling

fields of both positive and negative bias. **Figure 3.2** shows the general experimental approach, which is similar to the method Yun et al. and Richheimer et al. have used to study ion migration in unpassivated MA-based perovskites.[38,39]

First, we perform a single pass with the cantilever to measure the topography across a single line. Next, we lift the cantilever 10 nm above the sample, apply a potential to the tip, and perform a second pass across the same line. During the second pass, the poling bias causes mobile charges to move towards or away from the surface, depending upon the sign of the poling bias. Finally, we remove the poling bias, engage the Kelvin probe at the same lift height, and we measure the CPD between the tip and sample after poling. We repeat this process for every line in the image. After measuring the sample at a range of different tip voltages, we generate a stack of CPD images in the same region. This process ensures that there is no charge injected into the film that could complicate the measurement or cause electrochemical interactions,[40] and probes the samples in the dark.

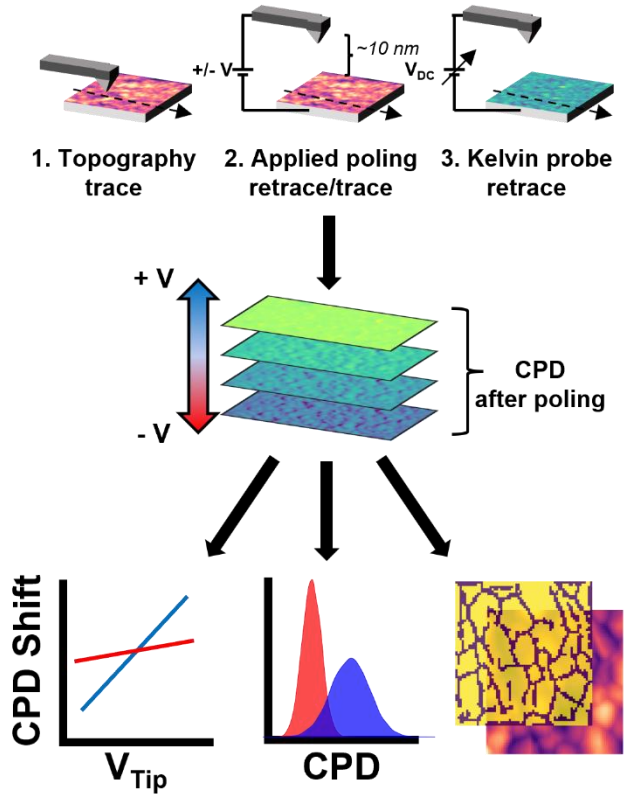

Figure 3.2. Schematic of poling-based SKPM measurement and pathways of data analysis. We measure the topography, followed by a poling step, and finally initiate a Kelvin probe loop to measure the CPD at each line in the image. Parameters such as CPD shift, CPD shift distribution and domain interface-domain center heterogeneity are extracted in data analysis.

We use the poling-based SKPM measurement to probe a $Cs_{0.22}FA_{0.78}Pb(I_{0.85}Br_{0.15})_3$ control film on ITO under biases ranging from -3 V to +3 V with steps of 1 V. **Figures 3.3a-d** show the topography and the evolution of the CPD at applied biases of 0, +3, and -3 V. We observe a shift to more positive CPD values when applying a positive bias to the tip, which we attribute to the buildup of negative charges at the surface. This is consistent with accumulation of negative ionic surface charge at the film surface resulting in a vacuum level offset. We observe the opposite effect when a negative bias is applied to the tip – a large shift to negative CPD values is seen as positive charges accumulate at the surface, resulting in a vacuum-level offset of

the opposite sign, which we illustrate in **Appendix B Figure S2**. **Figure 3.3d**, measured at a tip bias of -3 V, shows a significant degree of heterogeneity in the CPD as the applied tip bias becomes more negative and net positive charge accumulates at the perovskite surface (presumably due to driving negative ions away).

Figures 3.3e-h show the topography and CPD evolution of an APTMS-passivated perovskite film on ITO, which reveals two key differences between the passivated and unpassivated samples. First, the surface-passivated samples show lower overall shifts in their CPD following local poling. Second, the passivated perovskite films have much more homogenous CPD distributions, both before, and after poling.

Figure 3.3i shows the distribution of the CPD shift, which is determined by the difference between the CPD after poling and the CPD measured at 0 V. **Figures 3.3j and k** show the average CPD shift and full-width half max (FWHM) of the CPD shift relative to the poling bias. We see that the average CPD shift measured at the bias extremes decreases from around 100 mV to only ~20 mV. Importantly, this observation that APTMS-based passivation reduces the CPD shift induced during poling is consistent with the hypothesized suppression of ion migration due to the suppression of halide vacancies. Accordingly, the FWHM of the measured CPD shift should reflect the extent of heterogeneity in local ion migration in a given film. **Figure 3.3k** shows that upon applying more negative biases, we observe a broadening of the FWHM in the unpassivated film, while the APTMS-passivated film exhibits a consistent, narrow FWHM of only ~10 mV. We propose that this difference is due to the greater heterogeneity in the control film, likely due to differences in ion mobility between the perovskite domains and the interfaces between domains. In **Appendix B Figure S5**, we present topography and CPD shift images for a second wide-bandgap perovskite formulation - $Cs_{0.17}FA_{0.83}Pb(I_{0.75}Br_{0.25})_3$ – with and without

APTMS passivation. We also show a full picture of the average CPD shift and heterogeneity as a function of poling bias for both perovskite formulations in **Appendix B Figure S6**. Overall, these results show that APTMS surface passivation mitigates ion migration in the wide-gap perovskite formulations studied here via reducing the concentration of surface defects – such as halide vacancies.

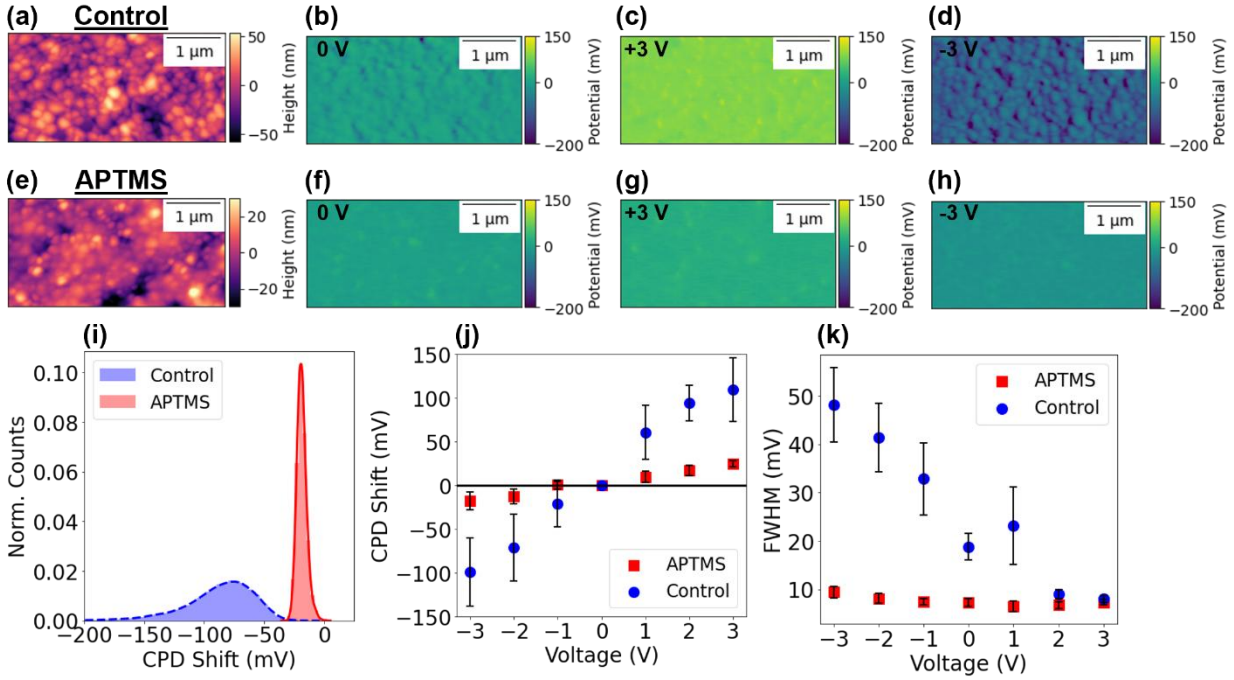

Figure 3.3. (a) Topography and (b-d) CPD of a $Cs_{0.22}FA_{0.78}Pb(I_{0.85}Br_{0.15})_3$ control film measured with applied tip biases of 0, +3, and -3 V. (e) Topography and (f-h) CPD of APTMS passivated film measured with applied tip biases of 0, +3, and -3 V. All CPD images are displayed on the same color scale to show the differences between the two samples. (i) Probability density distribution of the shift in CPD relative to the baseline CPD for control and APTMS passivated films measured at -3 V. (j) CPD shift relative to the baseline CPD as a function of bias for control and APTMS passivated films. (k) FWHM of the CPD shift distribution as a function of applied tip bias for control and APTMS passivated films. Error bars are shown as standard error of the mean for three measurements performed on three different films.

We recognize based on previous literature that the topographical features observed are not necessarily grain boundaries, as a single crystallite can contain multiple domains,[41,42] but for the purposes of convenience here we refer to the crystallites as "domains" and the spaces between them as "interfaces". To separate the differences between the perovskite domains and interfaces, we compare the mean CPDs at the domains and interfaces using images of the $Cs_{0.22}FA_{0.78}Pb(I_{0.85}Br_{0.15})_3$ film collected at various biases. To achieve this separation, we align each CPD image based on its associated topography image and manually select masks to distinguish individual topographical domains. **Figures 3.4a and b** show the topography of the unpassivated perovskite film, and the mask used to separate the domains and interfaces. Using this methodology, we aggregate the CPD as a function of distance to the nearest domain interface pixel for control and APTMS-passivated films. **Figure 3.4c** shows the average CPD as a function of distance to the nearest domain interface for control and APTMS-passivated films measured with a -3 V bias (**Appendix B Figure S7** shows this calculation for all poling biases). We observe a large difference in the average CPD measured at or near domain interfaces compared to regions further away – at domain centers. In films that are surface passivated with APTMS, we see that the CPD becomes more homogenous relative to its distance from the nearest interface. The error bars in **Figure 3.4c** show the distribution of CPD values measured at each distance and thus represent heterogeneity in surface defect density. We see that APTMS passivation significantly narrows this distribution at all distances, which we attribute to the effective treatment of surface defects. **Figure 3.4d** shows the difference between the average CPD measured at domain centers and interfaces relative to the poling bias for unpassivated and APTMS-passivated films. We observe a decreasing trend in the CPD difference with poling biases increasing from -3 to +3 V for the unpassivated film. In contrast, we see the CPD

difference remains relatively unchanged with varying biases for the passivated film. **Appendix B Figure S8** visualizes the difference between the domain centers and interfaces, in which we see a contrast inversion in the CPD color scale for the unpassivated film. The larger CPD shifts at the visible interfaces are consistent with a range of literature reports suggesting increased ion motion near surface interfaces and domain interfaces.[38,40,43] Importantly, these new SKPM results also show that APTMS-based passivation preferentially treats domain interface-related defects, leading to significantly more homogeneous films in terms of their response to bias-induced ion motion.

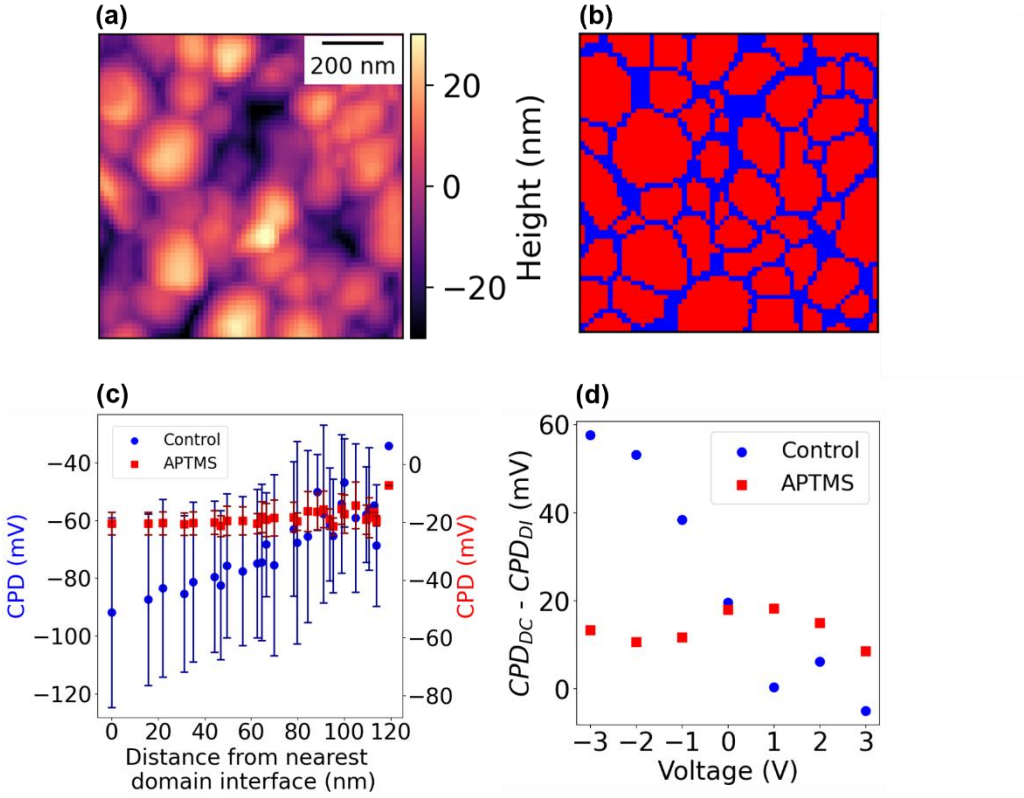

Figure 3.4. (a) Topography of $Cs_{0.22}FA_{0.78}Pb(I_{0.85}Br_{0.15})_3$ control film. (b) Binary mask created to separate perovskite domains (red) from domain interfaces (blue). (c) Average CPD as a function of distance from the nearest domain interface for control and APTMS-passivated films. The errors bars show the standard deviation or distribution of CPD values measured at each

difference. (d) Difference in the CPD measured at domain centers (DC) and interfaces (DI) for control and APTMS-passivated films.

Finally, we use hyperspectral photoluminescence microscopy to further explore ion migration in the control and APTMS-treated films. For this measurement, we kept the perovskite samples in a dry-nitrogen environment and excited them with a 532 nm laser at 600 mW/cm^2. Although higher than one Sun, we selected this illumination intensity to accelerate the effects of ion migration within a reasonable time frame. We provide further details of the measurement parameters in the Appendix B.

Figures 3.5a and b show peak wavelength maps of the unpassivated perovskite sample before and after light-soaking under laser illumination, obtained with hyperspectral PL microscopy. **Figure 3.5c** shows the normalized ensemble PL spectra measured during the light-soaking process. Based on the time-dependent evolution of the PL, we observe a shift in the PL spectra and spatial distribution of features, which we interpret as phase segregation with contributions from both iodide-rich (peak emission at 780 nm) and mixed (peak emission at 740 nm) phases.[44] This phase segregation can be visualized in the overall spectra as a shoulder peak emerging at 772 nm. The existence of phase segregated regions prior to photosoaking have been attributed to an inhomogeneous elemental distribution that forms during the crystallization process.[45–47] **Figures 3.5a and b** show that the iodide-rich regions grow significantly in size after 30 minutes of light soaking.

We also looked at hyperspectral photoluminescence maps of APTMS-passivated films. **Appendix B Figure S10** shows the cumulative photoluminescence mapping for unpassivated and APTMS-passivated films, in which we see a consistently higher photoluminescence intensity for the surface passivated films. **Figures 3.5d and e** show the hyperspectral mapping and overall

photoluminescence spectra for APTMS-passivated films undergoing light-soaking. Similar to the control film, we see initial halide segregation. In contrast to the control, we see that the growth of the iodide-rich regions is hindered by the APTMS surface passivation. In both films, we observe a slight red-shifting of the main mixed-phase emission peak, which may be attributed to demixing of the A-site cations as observed by Knight, et al.[44]

We apply a wavelength threshold of 765 nm to separate the mixed and iodide-rich phases by binning the pixels based on their emission wavelength (**Appendix B Figure S11a**), with the aim of further understanding how the mixed and iodide-rich phases evolve over the course of light-soaking. **Appendix B Figure S11b** shows the shift in emission wavelength relative to light-soaking duration for the mixed and iodide-rich phases in control and passivation films. We see the conversion from mixed-phase to iodide-rich perovskite during light-soaking, where regions emitting at wavelengths shorter than 765 nm, prior to prolonged light exposure, shift to longer wavelengths over time. This effect is more pronounced in the control film as compared to the APTMS-passivated film.

In **Appendix Figure S11c**, we determined the extent of phase segregation by calculating the fraction of iodide-rich pixels relative to mixed-phase pixels as a function of light-soaking time compared with the initial amount of phase-segregation prior to light exposure. While both the control and APTMS-passivated films show consistent red-shifting with light-soaking, the extent of phase-segregation increases to 7X its initial value after prolonged light-soaking in the control film, as compared to an increase of 2X in the APTMS-passivated film. Overall, we see that APTMS passivates defects like halide vacancies in wide-gap perovskites, which results in increased photoluminescence quantum yields and reduces halide segregation. These

photoluminescence observations are in agreement with and complement the results obtained with SKPM.

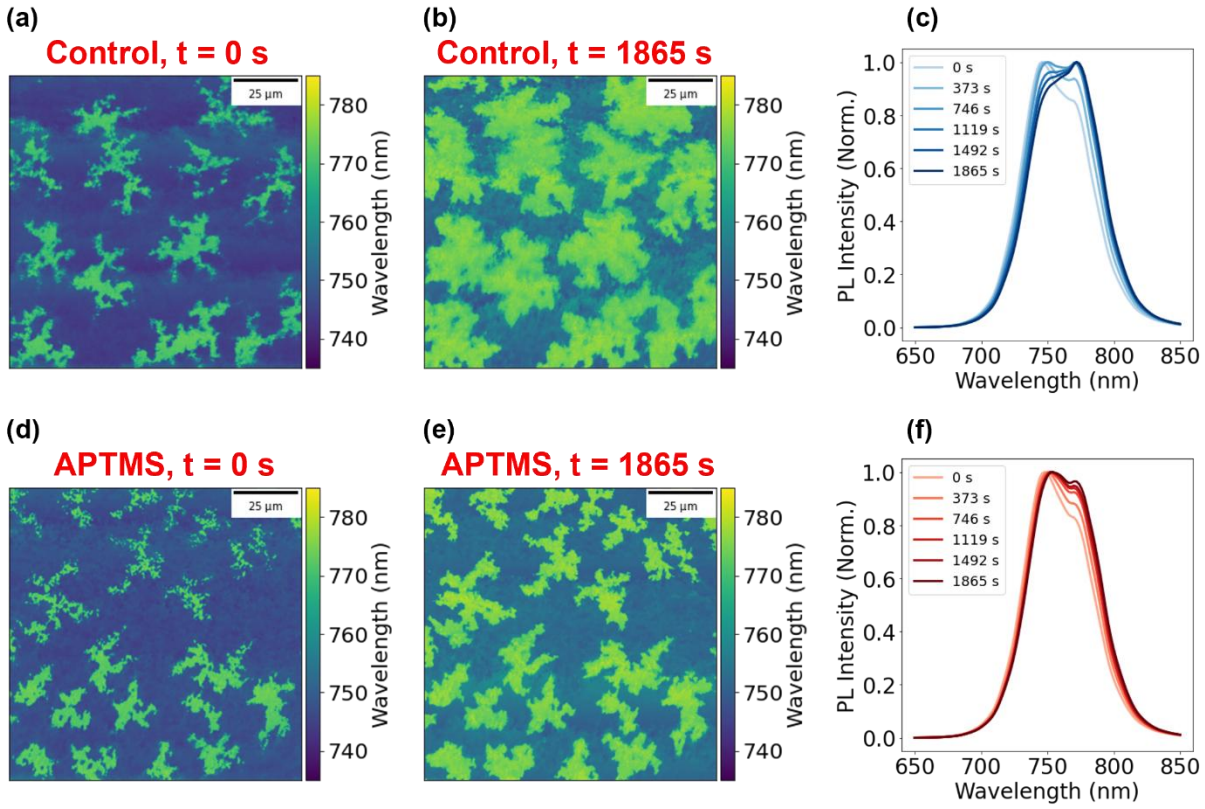

Figure 3.5. Peak wavelength images, extracted from hyperspectral photoluminescence microscopy, collected at light-soaking times of (a) 0 s and (b) 1865 s for the unpassivated $Cs_{0.22}FA_{0.78}Pb(I_{0.85}Br_{0.15})_3$ control. (c) Ensemble spectra as a function of time for control films obtained from the hyperspectral maps. Peak wavelength images, extracted from hyperspectral photoluminescence microscopy, collected at light-soaking times of (d) 0 s and (e) 1865 s for $Cs_{0.22}FA_{0.78}Pb(I_{0.85}Br_{0.15})_3$ passivated with APTMS. The color scale represents the emission wavelength of each pixel. (f) Ensemble spectra for APTMS passivated films calculated from hyperspectral maps. Samples were excited with a 532 nm laser and a fluence of ~600 mW/cm^2.

3.4 Conclusions

Studying the evolution of the surface potential with SKPM following poling reveals insight into how APTMS passivation affects ion motion in halide perovskites. Notably, we observe a significant reduction in the concentration of charges that drift from poling after surface passivation with APTMS. We examined differences in the CPD of domain centers and domain interfaces as a function of poling bias and polarity, and we observed that domain interfaces exhibit a higher amount of ion migration compared to domain centers. This difference is suppressed following passivation with APTMS. To further study the role of APTMS on ion migration, we used hyperspectral photoluminescence microscopy to explore time-dependent halide segregation during illumination of these materials. We found that halide segregation, as measured by the PL red-shift, is significantly more pronounced in unpassivated films. Taken together, these data indicate that surface passivation with the unique chemistry of APTMS molecules reduces ion migration, both in terms of domain-to-domain variations in ion migration rate as well as the overall ion migration magnitude, and that these effects are correlated with lower amounts of photoinduced halide segregation. With the combination of scanning probe microscopy and defect passivation with APTMS, we see the surface and domain interfaces play an important role in ion migration. These results highlight the importance of continuing to develop new strategies to measure ion migration at the local level and provide a simple method for screening new passivating agents via AFM for beneficial ion migration properties.

3.5 Acknowledgements

This letter is based on work supported primarily by the U.S. Department of Energy (DOE-SC0013957). Part of this work was conducted at the Washington Nanofabrication Facility / Molecular Analysis Facility, a National Nanotechnology Coordinated Infrastructure (NNCI)

site at the University of Washington with partial support from the National Science Foundation via awards NNCI-1542101 and NNCI-2025489, the Molecular Engineering & Sciences Institute, the Clean Energy Institute, and the University of Washington. We acknowledge the University of Washington Clean Energy Institute and the Washington Research Foundation. M.D.B. is supported by an NSF Graduate Student Fellowship under Grant no. DGE-2140004. D.S.G. acknowledges salary and infrastructure support from the Washington Research Foundation, the Alvin L. and Verla R. Kwiram endowment, and the B. Seymour Rabinovitch Endowment.

3.6 References

(1) Fakharuddin, A.; Gangishetty, M. K.; Abdi-Jalebi, M.; Chin, S. H.; bin Mohd Yusoff, A. R.; Congreve, D. N.; Tress, W.; Deschler, F.; Vasilopoulou, M.; Bolink, H. J. Perovskite Light-Emitting Diodes. *Nat Electron* **2022**, *5* (4), 203–216. https://doi.org/10.1038/S41928-022-00745-7.

(2) Kim, J. Y.; Lee, J. W.; Jung, H. S.; Shin, H.; Park, N. G. High-Efficiency Perovskite Solar Cells. *Chem Rev* **2020**, *120* (15), 7867–7918. https://doi.org/10.1021/acs.chemrev.0c00107.

(3) *NREL Photovoltaic Research-Cell Efficiency Chart. Available at https://www.nrel.gov/pv/cell-efficiency.html (accessed on Apr. 20, 2023).*

(4) Meggiolaro, D.; Mosconi, E.; De Angelis, F. Formation of Surface Defects Dominates Ion Migration in Lead-Halide Perovskites. *ACS Energy Lett* **2019**, *4* (3), 779–785. https://doi.org/10.1021/acsenergylett.9b00247.

(5) Eames, C.; Frost, J. M.; Barnes, P. R. F.; O'Regan, B. C.; Walsh, A.; Islam, M. S. Ionic Transport in Hybrid Lead Iodide Perovskite Solar Cells. *Nat Commun* **2015**, *6*, 7497. https://doi.org/10.1038/ncomms8497.

(6) Li, J.; Dong, Q.; Li, N.; Wang, L. Direct Evidence of Ion Diffusion for the Silver-Electrode-Induced Thermal Degradation of Inverted Perovskite Solar Cells. *Adv Energy Mater* **2017**, *7* (14), 1602922. https://doi.org/10.1002/aenm.201602922.

(7) Carrillo, J.; Guerrero, A.; Rahimnejad, S.; Almora, O.; Zarazua, I.; Mas-Marza, E.; Bisquert, J.; Garcia-Belmonte, G. Ionic Reactivity at Contacts and Aging of Methylammonium Lead Triiodide Perovskite Solar Cells. *Adv Energy Mater* **2016**, *6* (9), 1502246. https://doi.org/10.1002/aenm.201502246.

(8) Bush, K. A.; Frohna, K.; Prasanna, R.; Beal, R. E.; Leijtens, T.; Swifter, S. A.; McGehee, M. D. Compositional Engineering for Efficient Wide Band Gap Perovskites with Improved Stability to Photoinduced Phase Segregation. *ACS Energy Lett* **2018**, *3* (2), 428–435. https://doi.org/10.1021/acsenergylett.7b01255.

(9) Bischak, C. G.; Hetherington, C. L.; Wu, H.; Aloni, S.; Ogletree, D. F.; Limmer, D. T.; Ginsberg, N. S. Origin of Reversible Photoinduced Phase Separation in Hybrid Perovskites. *Nano Lett* **2017**, *17* (2), 1028–1033. https://doi.org/10.1021/acs.nanolett.6b04453.

(10) Motti, S. G.; Patel, J. B.; Oliver, R. D. J.; Snaith, H. J.; Johnston, M. B.; Herz, L. M. Phase Segregation in Mixed-Halide Perovskites Affects Charge-Carrier Dynamics While Preserving Mobility. *Nat Commun* **2021**, *12*, 6955. https://doi.org/10.1038/s41467-021-26930-4.

(11) Brennan, M. C.; Ruth, A.; Kamat, P. V.; Kuno, M. Photoinduced Anion Segregation in Mixed Halide Perovskites. *Trends Chem* **2020**, *2* (4), 282–301. https://doi.org/10.1016/j.trechm.2020.01.010.

(12) Haruyama, J.; Sodeyama, K.; Han, L.; Tateyama, Y. First-Principles Study of Ion Diffusion in Perovskite Solar Cell Sensitizers. *J Am Chem Soc* **2015**, *137* (32), 10048–10051. https://doi.org/10.1021/jacs.5b03615.

(13) Niu, T.; Lu, J.; Munir, R.; Li, J.; Barrit, D.; Zhang, X.; Hu, H.; Yang, Z.; Amassian, A.; Zhao, K.; Liu, S. F. Stable High-Performance Perovskite Solar Cells via Grain Boundary Passivation. *Advanced Materials* **2018**, *30* (16), 1706576. https://doi.org/10.1002/adma.201706576.

(14) Hanmandlu, C.; Swamy, S.; Singh, A.; Chen, H.-A.; Liu, C.-C.; Lai, C.-S.; Mohapatra, A.; Pao, C.-W.; Chen, P.; Chu, W. Suppression of Surface Defects to Achieve Hysteresis-Free Inverted Perovskite Solar Cells via Quantum Dot Passivation. *J. Mater. Chem. A* **2020**, *8*, 5263–5274. https://doi.org/10.1039/c9ta12904a.

(15) Tumen-Ulzii, G.; Matsushima, T.; Klotz, D.; Leyden, M. R.; Wang, P.; Qin, C.; Lee, J.-W.; Lee, S.-J.; Yang, Y.; Adachi, C. Hysteresis-Less and Stable Perovskite Solar Cells with a Self-Assembled Monolayer. *Commun Mater* **2020**, *1* (31). https://doi.org/10.1038/s43246-020-0028-z.

(16) Lin, R.; Xu, J.; Wei, M.; Wang, Y.; Qin, Z.; Liu, Z.; Wu, J.; Xiao, K.; Chen, B.; Min Park, S.; Chen, G.; Atapattu, H. R.; Graham, K. R.; Xu, J.; Zhu, J.; Li, L.; Zhang, C.; Sargent, E. H.; Tan, H. All-Perovskite Tandem Solar Cells with Improved Grain Surface Passivation. *Nature* | **2022**, *603*, 73. https://doi.org/10.1038/s41586-021-04372-8.

(17) Qian, F.; Yuan, S.; Cai, Y.; Han, Y.; Zhao, H.; Sun, J.; Liu, Z.; Liu, S. Novel Surface Passivation for Stable FA0.85MA0.15PbI3 Perovskite Solar Cells with 21.6% Efficiency. *Solar RRL* **2019**, *3* (7), 1900072. https://doi.org/10.1002/solr.201900072.

(18) Laskar, M. A. R.; Luo, W.; Ghimire, N.; Chowdhury, A. H.; Bahrami, B.; Gurung, A.; Reza, K. M.; Pathak, R.; Bobba, R. S.; Lamsal, B. S.; Chen, K.; Rahman, M. T.; Rahman, S. I.; Emshadi, K.; Xu, T.; Liang, M.; Zhang, W. H.; Qiao, Q. Phenylhydrazinium Iodide for Surface Passivation and Defects Suppression in Perovskite Solar Cells. *Adv Funct Mater* **2020**, *30* (22), 2000778. https://doi.org/10.1002/adfm.202000778.

(19) He, Q.; Worku, M.; Xu, L.; Zhou, C.; Lteif, S.; Schlenoff, J. B.; Ma, B. Surface Passivation of Perovskite Thin Films by Phosphonium Halides for Efficient and Stable Solar Cells. *J. Mater. Chem. A* **2020**, *8*, 2039–2046. https://doi.org/10.1039/c9ta12597c.

(20) Jiang, Q.; Zhao, Y.; Zhang, X.; Yang, X.; Chen, Y.; Chu, Z.; Ye, Q.; Li, X.; Yin, Z.; You, J. Surface Passivation of Perovskite Film for Efficient Solar Cells. *Nat Photonics* **2019**, *13* (7), 460–466. https://doi.org/10.1038/s41566-019-0398-2.

(21) Shirzadi, E.; Tappy, N.; Ansari, F.; Nazeeruddin, M. K.; Hagfeldt, A.; Dyson, P. J. Deconvolution of Light-Induced Ion Migration Phenomena by Statistical Analysis of Cathodoluminescence in Lead Halide-Based Perovskites. *Advanced Science* **2022**, *9* (13), 2103729. https://doi.org/10.1002/advs.202103729.

(22) Chen, C.; Song, Z.; Xiao, C.; A. Awni, R.; Yao, C.; Shrestha, N.; Li, C.; Singh Bista, S.; Zhang, Y.; Chen, L.; J. Ellingson, R.; Jiang, C.-S.; Al-Jassim, M.; Fang, G.; Yan, Y. Arylammonium-Assisted Reduction of the Open-Circuit Voltage Deficit in Wide-Bandgap Perovskite Solar Cells: The Role of Suppressed Ion Migration. *ACS Energy Lett* **2020**, *5* (8), 2560–2568. https://doi.org/10.1021/acsenergylett.0c01350.

(23) Kang, D.-H.; Kim, S.-Y.; Lee, J.-W.; Park, N.-G. Efficient Surface Passivation of Perovskite Films by a Post-Treatment Method with a Minimal Dose. *J. Mater. Chem. A* **2021**, *9*, 3441–3450. https://doi.org/10.1039/d0ta10581c.

(24) Mahapatra, A.; Parikh, N.; Kumari, H. Reducing Ion Migration in Methylammonium Lead Tri-Bromide Single Crystal via Lead Sulfate Passivation. *J. Appl. Phys* **2020**, *127*, 185501. https://doi.org/10.1063/5.0005369.

(25) Jariwala, S.; Burke, S.; Dunfield, S.; Shallcross, R. C.; Taddei, M.; Wang, J.; Eperon, G. E.; Armstrong, N. R.; Berry, J. J.; Ginger, D. S. Reducing Surface Recombination Velocity of Methylammonium-Free Mixed-Cation Mixed-Halide Perovskites via Surface Passivation. *Chemistry of Materials* **2021**, *33* (13), 5035–5044. https://doi.org/10.1021/acs.chemmater.1c00848.

(26) Shi, Y.; Rojas-Gatjens, E.; Wang, J.; Pothoof, J.; Giridharagopal, R.; Ho, K.; Jiang, F.; Taddei, M.; Yang, Z.; Sanehira, E. M.; Irwin, M. D.; Silva-Acuña, C.; Ginger, D. S. (3-Aminopropyl)Trimethoxysilane Surface Passivation Improves Perovskite Solar Cell Performance by Reducing Surface Recombination Velocity. *ACS Energy Lett* **2022**, *7* (11), 4081–4088. https://doi.org/10.1021/acsenergylett.2c01766.

(27) Chen, B.; Rudd, P. N.; Yang, S.; Yuan, Y.; Huang, J. Imperfections and Their Passivation in Halide Perovskite Solar Cells. *Chem. Soc. Rev* **2019**, *48*, 3842–3867. https://doi.org/10.1039/c8cs00853a.

(28) Abdi-Jalebi, M.; Andaji-Garmaroudi, Z.; Cacovich, S.; Stavrakas, C.; Philippe, B.; Richter, J.; Alsari, M.; Booker, E. P.; Hutter, E.; Pearson, A. J.; Lilliu, S.; Savenije, T. J.; Rensmo, H.; Divitini, G.; Ducati, C.; Friend, R.; Stranks, S. D. Maximizing and Stabilizing Luminescence from Halide Perovskites with Potassium Passivation. *Nature* **2018**, *555*, 497–501. https://doi.org/10.1038/nature25989.

(29) Westbrook, R. J. E.; Macdonald, T. J.; Xu, W.; Lanzetta, L.; Marin-Beloqui, J. M.; Clarke, T. M.; Haque, S. A. Lewis Base Passivation Mediates Charge Transfer at Perovskite Heterojunctions. *J. Am. Chem. Soc* **2021**, *143*, 12230–12243. https://doi.org/10.1021/jacs.1c05122.

(30) Jiang, F.; Pothoof, J.; Muckel, F.; Giridharagopal, R.; Wang, J.; Ginger, D. S. Scanning Kelvin Probe Microscopy Reveals That Ion Motion Varies with Dimensionality in 2D Halide Perovskites. *ACS Energy Lett* **2021**, *6* (1), 100–108. https://doi.org/10.1021/acsenergylett.0c02032.

(31) Birkhold, S. T.; Precht, J. T.; Giridharagopal, R.; Eperon, G. E.; Schmidt-Mende, L.; Ginger, D. S. Direct Observation and Quantitative Analysis of Mobile Frenkel Defects in Metal Halide Perovskites Using Scanning Kelvin Probe Microscopy. *Journal of Physical Chemistry C* **2018**, *122* (24), 12633–12639. https://doi.org/10.1021/acs.jpcc.8b03255.

(32) Birkhold, S. T.; Precht, J. T.; Liu, H.; Giridharagopal, R.; Eperon, G. E.; Schmidt-Mende, L.; Li, X.; Ginger, D. S. Interplay of Mobile Ions and Injected Carriers Creates Recombination Centers in Metal Halide Perovskites under Bias. *ACS Energy Lett* **2018**, *3* (6), 1279–1286. https://doi.org/10.1021/acsenergylett.8b00505.

(33) Xu, F.; Zhang, M.; Li, Z.; Yang, X.; Zhu, R.; Xu, F.; Yang, X.; Zhu, R.; Zhang, M.; Li, Z. Challenges and Perspectives toward Future Wide-Bandgap Mixed-Halide Perovskite Photovoltaics. *Adv Energy Mater* **2023**, *13* (13), 2203911. https://doi.org/10.1002/aenm.202203911.

(34) Xu, J.; Boyd, C. C.; Yu, Z. J.; Palmstrom, A. F.; Witter, D. J.; Larson, B. W.; France, R. M.; Werner, J.; Harvey, S. P.; Wolf, E. J.; Weigand, W.; Manzoor, S.; Van Hest, M. F. A. M.; Berry, J. J.; Luther, J. M.; Holman, Z. C.; McGehee, M. D. Triple-Halide Wide-Band Gap Perovskites with Suppressed Phase Segregation for Efficient Tandems. *Science* **2020**, *367*, 1097–1104. https://doi.org/10.1126/science.aaz5074.

(35) Yun, J. S.; Seidel, J.; Kim, J.; Soufiani, A. M.; Huang, S.; Lau, J.; Jeon, N. J.; Seok, S. Il; Green, M. A.; Ho-Baillie, A. Critical Role of Grain Boundaries for Ion Migration in Formamidinium and Methylammonium Lead Halide Perovskite Solar Cells. *Adv Energy Mater* **2016**, *6* (13), 1600330. https://doi.org/10.1002/aenm.201600330.

(36) Richheimer, F.; Toth, D.; Hailegnaw, B.; Baker, M. A.; Dorey, R. A.; Kienberger, F.; Castro, F. A.; Kaltenbrunner, M.; Scharber, M. C.; Gramse, G.; Wood, S. Ion-Driven Nanograin Formation in Early-Stage Degradation of Tri-Cation Perovskite Films. *Nanoscale* **2022**, *14* (7), 2605–2616. https://doi.org/10.1039/d1nr05045a.

(37) Giridharagopal, R.; Precht, J. T.; Jariwala, S.; Collins, L.; Jesse, S.; Kalinin, S. V.; Ginger, D. S. Time-Resolved Electrical Scanning Probe Microscopy of Layered Perovskites Reveals Spatial Variations in Photoinduced Ionic and Electronic Carrier Motion. *ACS Nano* **2019**, *13* (3), 2812–2821. https://doi.org/10.1021/acsnano.8b08390.

(38) Li, W.; Yadavalli, S. K.; Lizarazo-Ferro, D.; Chen, M.; Zhou, Y.; Padture, N. P.; Zia, R. Subgrain Special Boundaries in Halide Perovskite Thin Films Restrict Carrier Diffusion. *ACS Energy Lett* **2018**, *3* (11), 2669–2670. https://doi.org/10.1021/acsenergylett.8b01704.

(39) Jariwala, S.; Sun, H.; Adhyaksa, G. W. P.; Lof, A.; Muscarella, L. A.; Ehrler, B.; Garnett, E. C.; Ginger, D. S. Local Crystal Misorientation Influences Non-Radiative Recombination in Halide Perovskites. *Joule* **2019**, *3* (12), 3048–3060. https://doi.org/10.1016/j.joule.2019.09.001.

(40) Shao, Y.; Fang, Y.; Li, T.; Wang, Q.; Dong, Q.; Deng, Y.; Yuan, Y.; Wei, H.; Wang, M.; Gruverman, A.; Shield, J.; Huang, J. Grain Boundary Dominated Ion Migration in

Polycrystalline Organic-Inorganic Halide Perovskite Films. *Energy Environ Sci* **2016**, *9* (5), 1752–1759. https://doi.org/10.1039/c6ee00413j.

(41) Knight, A. J.; Borchert, J.; Oliver, R. D. J.; Patel, J. B.; Radaelli, P. G.; Snaith, H. J.; Johnston, M. B.; Herz, L. M. Halide Segregation in Mixed-Halide Perovskites: Influence of A-Site Cations. *ACS Energy Lett* **2021**, *6* (2), 799–808. https://doi.org/10.1021/acsenergylett.0c02475.

(42) Luo, Y.; Aharon, S.; Stuckelberger, M.; Magaña, E.; Lai, B.; Bertoni, M. I.; Etgar, L.; Fenning, D. P. The Relationship between Chemical Flexibility and Nanoscale Charge Collection in Hybrid Halide Perovskites. *Adv Funct Mater* **2018**, *28* (18), 1706995. https://doi.org/10.1002/adfm.201706995.

(43) Wieghold, S.; Tresback, J.; Correa-Baena, J. P.; Hartono, N. T. P.; Sun, S.; Liu, Z.; Layurova, M.; Vanorman, Z. A.; Bieber, A. S.; Thapa, J.; Lai, B.; Cai, Z.; Nienhaus, L.; Buonassisi, T. Halide Heterogeneity Affects Local Charge Carrier Dynamics in Mixed-Ion Lead Perovskite Thin Films. *Chemistry of Materials* **2019**, *31* (10), 3712–3721. https://doi.org/10.1021/acs.chemmater.9b00650.

(44) Gratia, P.; Grancini, G.; Audinot, J. N.; Jeanbourquin, X.; Mosconi, E.; Zimmermann, I.; Dowsett, D.; Lee, Y.; Grätzel, M.; de Angelis, F.; Sivula, K.; Wirtz, T.; Nazeeruddin, M. K. Intrinsic Halide Segregation at Nanometer Scale Determines the High Efficiency of Mixed Cation/Mixed Halide Perovskite Solar Cells. *J Am Chem Soc* **2016**, *138* (49), 15821–15824. https://doi.org/10.1021/jacs.6b10049.

Chapter 4: Sub-diffraction Imaging of Carrier Dynamics in Halide Perovskite Semiconductors: Effects of Passivation, Morphology, and Ion Motion

Madeleine D. Breshears[+], Justin Pothoof[+], Rajiv Giridharagopal, David S. Ginger

[+]M.D. Breshears and J. Pothoof contributed equally to this work.

4.1 Overview

We spatially resolve photocarrier dynamics in halide perovskites using time-resolved electrostatic force microscopy (trEFM) to map surface potential equilibration during photoexcitation. Following treatment with different surface passivation agents, we show that trEFM probes dynamics directly related to surface recombination velocity and carrier lifetimes correlated with time-resolved photoluminescence. Our results reveal nanoscale variations in recombination dynamics following surface passivation. We also observe heterogeneity in surface potential equilibration times dependent on perovskite film morphology. We combine wavelength- and intensity-dependent measurements with drift-diffusion simulations to disentangle the influence of carrier recombination and ion migration on surface potential equilibration. These results demonstrate that we can use mechanical detection to image electronic carrier recombination dynamics in perovskites below the optical diffraction limit while also showing the potential for future improvements in heterogeneity of surface passivation.

4.2 Introduction

Halide perovskite semiconductors have numerous applications including solar cells,[1,2] light-emitting diodes,[2,3] radiation detectors,[4] and even sources of quantum light.[5] Their advantages include scalable additive manufacturing, large absorption coefficients, bandgap tunability,[6] and high defect tolerance.[2] While perovskites are defect tolerant, they are not defect free.[2,7–11] Passivation strategies to reduce surface recombination velocity (SRV) by a factor of ~100 have improved perovskite device efficiencies over the last several years.[7,12–17] At the same time, ion motion, linked to phase segregation and electrochemical reactions, can be a limiting factor in perovskite semiconductor performance and stability.[18–25] Probing these effects at the device level is useful, but inherently reflects average values given the heterogenous nature of halide perovskite thin films,[8,9,26–28] and understanding how local film microstructure correlates with both electronic and ionic defects,[8,9,27,29–31] could advance materials processing.

Indeed, microscopy tools that elucidate the relationship between local structure and nonradiative recombination have already proven useful for analyzing and improving semiconductor performance.[8,20,27,29,30,32–35] Time-resolved photoluminescence (trPL) probes electronic carrier recombination processes in perovskite materials;[36,37] and with confocal microscopy, we can obtain spatially resolved trPL maps at the optical diffraction limit. However, current best-in-class perovskites comprise mixed-cation, mixed-halide compositions with grains that are often ~100 nm or smaller,[38–40] which is far below the optical diffraction limit with visible light. Other techniques, such as cathodoluminescence microscopy, can map carrier recombination dynamics on the nanoscale using an electron beam but often damage the sample in the process.[32,41] The ideal microscopy tool for advancing cutting edge perovskites would thus allow for

measurement of carrier recombination dynamics at nanometer scale resolution without damaging the sample.

Time-resolved electrostatic force microscopy (trEFM), a scanning probe microscopy technique among the family of methods capable of providing fast electronic dynamics,[42–46] uses a mechanical cantilever to sense dynamic changes in the local electrostatic force gradient between the tip and the sample during photoexcitation.[30,31,47–49] To date, we have used trEFM to measure systems with large exciton binding energies such as organic photovoltaics and layered Ruddlesden-Popper perovskites.[30,31,43,48–53] In mixed-cation, mixed-halide perovskite systems where photoexcitation leads to free carriers, we expect the time-dependent changes measured should readily probe local recombination rates rather than be quantum efficiency-limited.

Here, we compare high-resolution trEFM images with spatially averaged trPL and drift-diffusion simulations. We show that trEFM measures the time it takes for surface potential to equilibrate as controlled by the evolution of electronic and ionic carrier concentrations during photoexcitation, and we probe the effects of chemical passivation on electronic carrier recombination and of local defect-mediated ion migration.

We demonstrate that treatments with different surface passivators, including (3-aminopropyl)trimethoxysilane (APTMS),[14–16] [3-(2-aminoethylamino)propyl]trimethoxysilane (AEAPTMS),[14] and phenethylammonium iodide (PEAI),[54,55] result in slower surface potential equilibration times due to reduced surface recombination velocities. We find that the local carrier dynamics vary with the perovskite morphology, where grain boundaries exhibit slower photoinduced dynamics than grain interiors. Through a combination of wavelength- and intensity-dependent experiments and drift-diffusion simulations, we show the competing influence of electronic carrier recombination and mobile ions on the surface potential equilibration time. We

attribute the slower surface potential equilibration times following chemical passivation to the suppression of SRV; we ascribe the slower surface potential equilibration time, observed at grain boundaries to locally higher defect densities that mediate slow ion migration and incur increased trap-mediated electronic carrier motion. Importantly, we show that surface potential equilibration times measured by trEFM correlate directly with minority carrier lifetimes and SRVs as measured by trPL. Our results connect the properties measured by trEFM with established optical characterization techniques and verify that trEFM can be a predictive tool for evaluating carrier recombination dynamics in modern halide perovskites with sub-diffraction-limited resolution, while also demonstrating that even common, effective surface passivation schemes can still exhibit local heterogeneity.

4.3 Results and Discussion

Figure 4.1a shows a schematic of the trEFM experiment we use to probe carrier dynamics below the diffraction limit.[48,49] Here, we photoexcite the sample through the ITO substrate using a laser with a rise time of ~2 ns and record the time evolution of the mechanical cantilever dynamics to record the transient electronic response of the sample. **Figure 4.1b** shows the timing diagram of the excitation. Following photoexcitation, the carrier populations generated by the illumination will evolve to a new equilibrium. The time-dependence of these processes leads to a time-dependent change in the surface potential, surface capacitance, and dissipative properties of the sample,[42,43,48,49] and these shifts lead to transient deviations of the cantilever motion from the steady-state sinusoidal motion of a damped, driven harmonic oscillator.[56] These transient deviations encode information about short time dynamics of the local electronic environment's approach to a new equilibrium, which can be reconstructed via empirical calibration,[48] or even simulation and machine learning approaches.[53] **Figure 4.1c** shows a representative cantilever

frequency shift over time in response to photoexcitation. We obtain this frequency shift by demodulating the cantilever's oscillation (see Methods and **Appendix C Note 1**). The rapid shift in the cantilever's frequency following photoexcitation captures the transient dynamics of interest; following that, the cantilever relaxes to its resonance frequency on timescales governed by the cantilever quality factor, Q. We fit the frequency vs. time trace to a product of two exponentials (black dotted line in **Figure 4.1c**), which enables us to find the time it takes for the cantilever to reach its maximum frequency deviation. We calibrate this time against the simulated response to excitation events with a defined time constant to extract a cantilever-independent time constant, τ (see Methods, **Appendix C Note 1**, and **Appendix C Figure S1**).[48,49] Next, we show that this time constant reflects the surface potential equilibration time in halide perovskites.

The surface potential equilibration time is controlled by the sample's electronic carrier recombination dynamics and illumination conditions. First, we show there is a qualitative correlation between trEFM and confocal PL microscopy over large length scales on a partial perovskite device stack (or "half-stack)" with the architecture ITO/Me-4PACz/$Cs_{0.17}FA_{0.83}Pb(I_{0.75}Br_{0.25})_3$. This perovskite formulation is known to exhibit PL heterogeneity on the multi-micron-scale.[57] **Figure 4.1d** shows a map of surface potential equilibration times in a 17.6×10 μm region-of-interest (ROI) as measured by trEFM, with empirical time constants on the microsecond-scale. **Appendix C Figure 4.2a** shows the topography. After imaging the sample with trEFM, we perform correlated confocal PL microscopy (see Methods). **Figure 4.1e** shows the PL intensity map of the ROI. **Figure 4.1f** shows correlated line traces (marked by the dashed lines in **Figure 4.1d,e**), where slower surface potential equilibration times measured by trEFM correspond to brighter PL. Annotations on **Figure 4.1f** show average minority carrier lifetime values collected at the corresponding positions shown in

Figure 4.1e, confirming that slower surface potential equilibration times measured by trEFM not only correlate to brighter PL, but also, qualitatively longer minority carrier lifetimes. **Appendix C Figure S2b** shows a positive correlation between local surface potential equilibration times measured by trEFM and carrier dynamics measured by trPL in this image, with a Pearson correlation coefficient of 0.88 (with a p-value of 0.018).

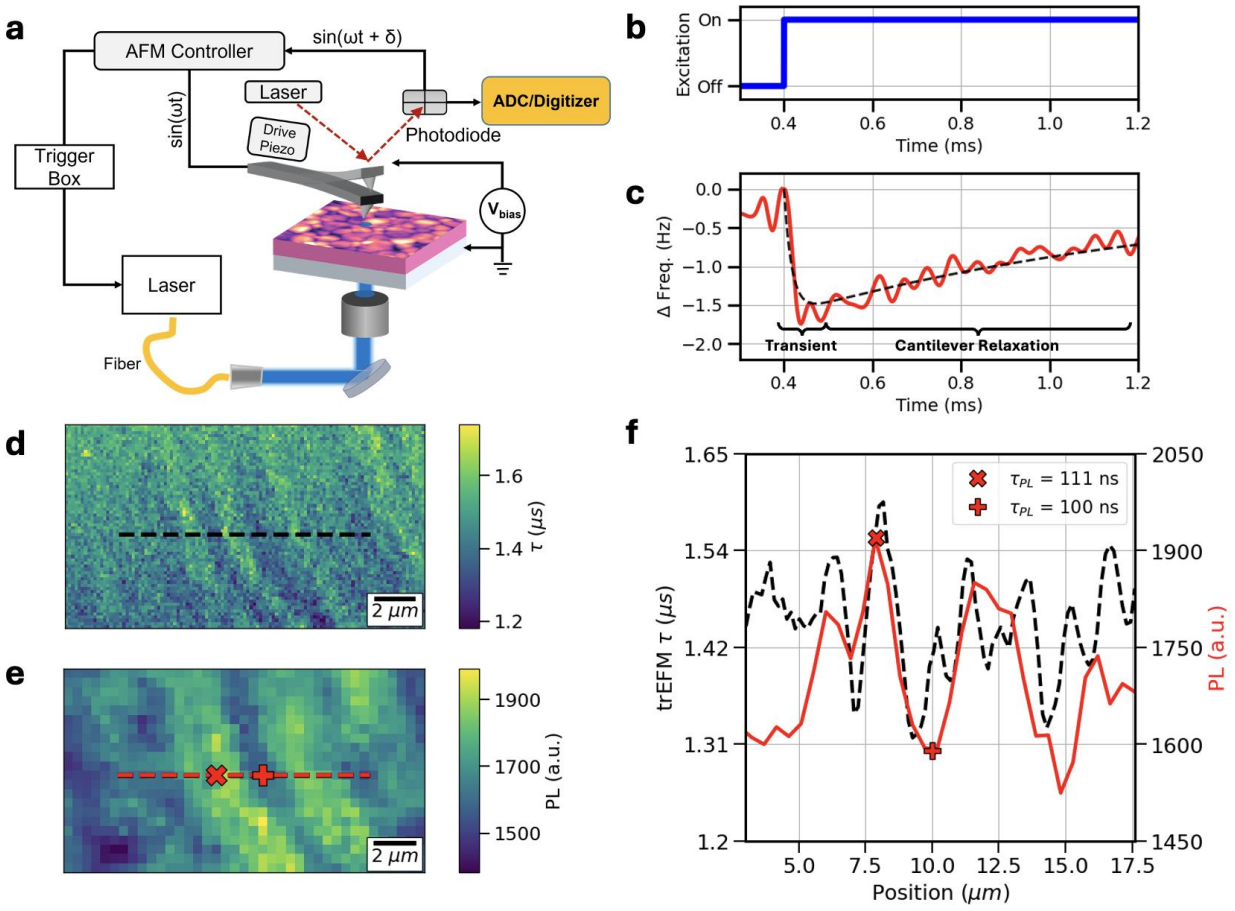

Figure 4.1: trEFM measures photoinduced dynamics that correlate to PL metrics of interest. (a) trEFM schematic, where ADC refers to an analog-to-digital converter. (b) Excitation protocol for typical trEFM experiment. (c) Change in instantaneous frequency of cantilever after excitation, where the black dashed line shows an empirical fit of the product of two exponentials which describe the transient perturbation of interest and the cantilever relaxation (see **Appendix C Note**

1). (d) trEFM map of photoinduced dynamics across a 17.6×10 μm ROI on a sample with the formulation $Cs_{0.17}FA_{0.83}Pb(I_{0.75}Br_{0.25})_3$ collected using 705 nm excitation at an incident intensity of 100 mW/cm^2; **Appendix C Figure S2a** shows the topography of this ROI. (e) Correlated PL map of the same ROI, taken using 60× objective, NA=0.7, using a 640 nm laser at a fluence of 105 nJ/cm^2. (f) Correlated line traces from the dotted lines shown in (d) and (e), where the trEFM line trace was smoothed to reduce pixel-to-pixel noise. Markers on (f) indicate positions shown in (e) where time-correlated single photon counting histograms were collected and fit with a stretched exponential (see **Appendix C Note 2**) to extract carrier lifetimes shown in legend (see **Appendix C Figure S2b** for additional PL lifetimes collected in this ROI and corresponding correlated surface potential equilibration times).

To further examine this correlation between trEFM equilibration times and electronic carrier dynamics, we investigate the effects of three established surface passivation agents: APTMS,[14–16] AEAPTMS,[14] and PEAI.[54,55] We prepared half-stacks with the architecture glass/ITO/Me-4PACz/$Cs_{0.22}FA_{0.78}Pb(I_{0.85}Br_{0.15})_3$. **Appendix C Figures S3-4** show UV-vis absorbance, XRD, PL, and trPL characterization for the half-stacks. The samples exhibit a Gaussian-shaped peak with a PL maximum at 755 nm, consistent with literature reports for this composition.[58] We fit the trPL decays using stretched exponential functions[36] and summarize the fit parameters in **Appendix C Table 1**. From the half-stack PL data, we extract an 18×, 2×, and 2× improvement in the minority carrier lifetime for APTMS, AEAPTMS, and PEAI treatments respectively. **Appendix C Figure S5** show the average PL quantum yields for each half-stack, which show a 13×, 4×, and 2× improvement for APTMS, AEAPTMS, and PEAI respectively. We attribute these enhancements to a reduction in nonradiative recombination pathways.[7,14–17,59]

Figure 4.2a shows the surface potential equilibration times we measured with trEFM on untreated and passivated samples plotted against the PL lifetime measured by trPL for those samples. **Appendix C Figure S6** show the trEFM maps for these samples and **Appendix C Figure S4** and **Appendix C Table 1** summarize the trPL measurements. We see that the extracted surface potential equilibration time scales proportionally to the carrier lifetime as measured on perovskite half-stacks before and after passivation. These trends are consistent with our interpretation of the trEFM probing the time it takes for the surface potential to equilibrate during photoexcitation, largely influenced by the time it takes for carriers to reach new equilibrium profiles. As we reduce nonradiative recombination pathways via passivation, we observe slower surface potential equilibration times that correspond to enhanced minority carrier lifetimes, consistent with general carrier generation and recombination kinetics.[60] However, consistently, the dynamics measured via trEFM are an order of magnitude larger than the average carrier lifetime measured via trPL, indicating that we are not measuring the trPL lifetime with trEFM. This difference is due to the nature of each experiment: trPL probes minority carrier population decay after pulsed excitation, while trEFM probes the evolution of the carrier population to a new equilibrium distribution in response to a step-function in photoexcitation.

In **Figure 4.2b**, we compare the trEFM time constant with the SRV computed from the trPL data following Wang et al.[13] (see **Appendix C Note 3** for additional information on this calculation). We find a strong inverse linear relationship between the dynamics measured by trEFM and the log of the SRV with a Pearson correlation coefficient of -0.91 (with a p-value of 0.013), where a value of -1.0 would indicate a perfect inverse correlation. These results show that the surface potential equilibration time measured by trEFM is predictive of the local SRV, meaning

we can use trEFM to characterize treatments for the suppression of nonradiative recombination at perovskite surfaces.

The direct correlation we show between trEFM equilibration times and SRV underpins the opportunity to image carrier dynamics below the optical diffraction limit. **Figures 4.2c,d** show the topography and surface potential equilibration times measured across a 2×1 μm region of an unpassivated perovskite half-stack. We measure surface potential equilibration times that range from 3.7 – 5.6 μs, with grain boundaries exhibiting slower dynamics than grain interiors. **Figures 4.2e,f** show the topography and surface potential equilibration time images for an APTMS-treated sample; APTMS polymerizes on the surface of the sample, changing the observed topography.[15,18,19] As expected from the above analysis, the equilibration times measured by trEFM are indeed significantly (~6×) slower after passivation. Furthermore, we can no longer differentiate grain interiors from grain boundaries. However, we still observe heterogeneous equilibration times across the ROI, indicating that passivated samples still exhibit local heterogeneity in SRV. We show in **Appendix C Figure S7** and **Appendix C Table 2** that these results are consistent across different regions and samples.

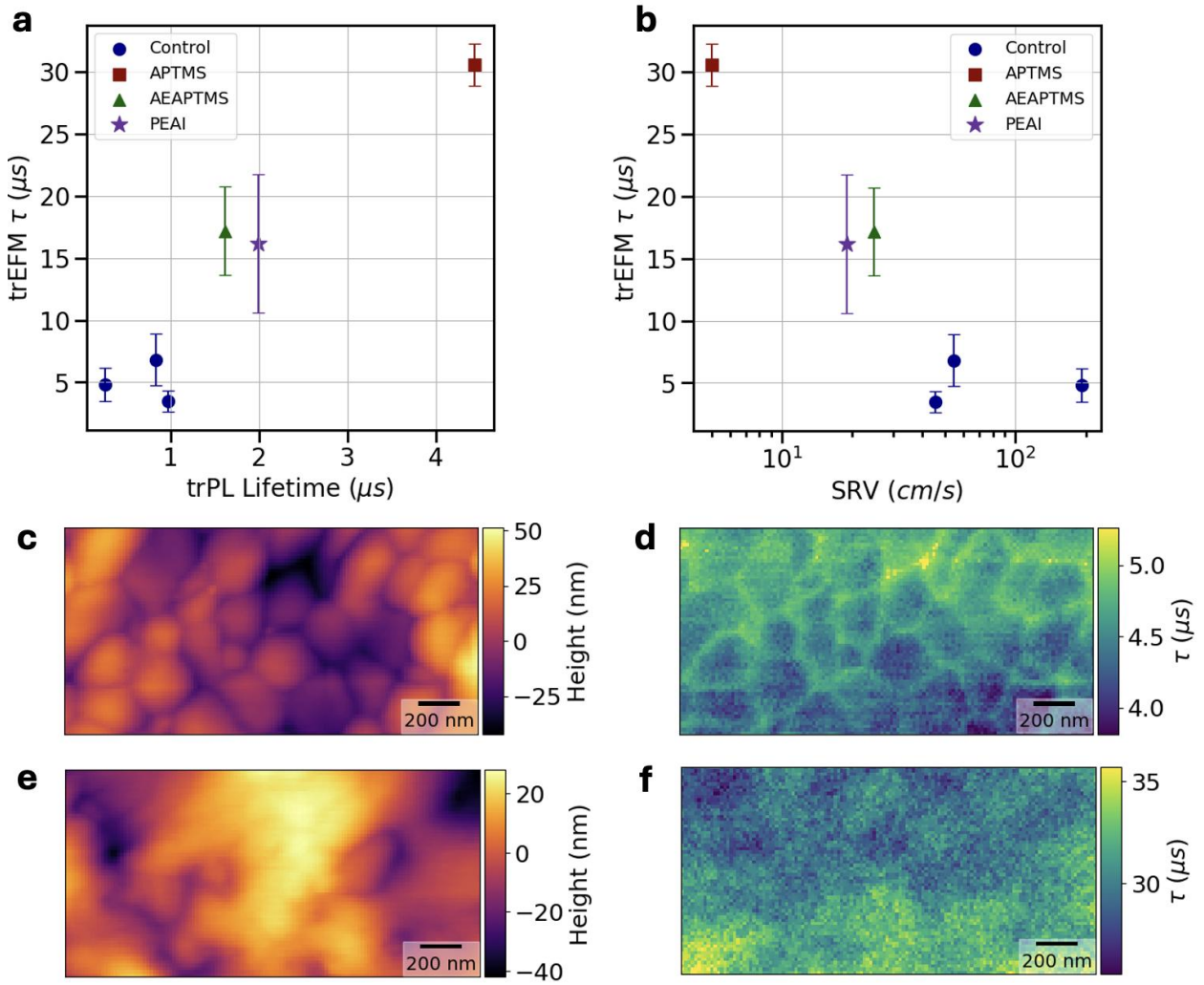

Figure 4.2: Photoinduced dynamics measured by trEFM correlate to PL lifetime and (inversely) to SRV, revealing nanoscale heterogeneity on unpassivated and passivated samples. (a) Average trEFM τ values plotted against minority carrier lifetimes measured by trPL and (b) approximated SRV (see **Appendix C Note 3** for SRV calculation). All trPL measurements were carried out using a pulsed 640 nm laser operated at ~30 nJ/cm^2 – enough to generate 2×10^{15} cm^{-3} carriers (1-2 Suns). (c) Topography of untreated half-stack and (d) corresponding trEFM τ map. (e) Topography of sample after APTMS-passivation with (f) trEFM τ map. All trEFM experiments here used a 405 nm laser with an incident intensity of ~150 mW/cm^2 (1.5 Suns) operated in a quasi-steady state regime.

The data so far support our hypothesis that trEFM dynamics probe carrier equilibration during photoexcitation, as dominated by SRV. To further examine this hypothesis, we use the open source 1D drift-diffusion simulator IonMonger, which enables us to explore the effects of various physical parameters, such as mobile ion concentration, excitation wavelength and intensity, and carrier recombination rates, on surface potential dynamics.[61–63] To reproduce our experimental setup, we model a device stack with an inverted, p-i-n architecture and we extract the potential evolution at the active layer surface. We find that the simulated surface potential equilibrates on the microsecond timescale, dependent on both the electronic carrier concentration and mobile ion concentration evolution, consistent with our experimental observations. **Appendix C Note 4** describes the relationship between electronic and ionic carrier populations and the surface potential evolution further.

Figure 4.3a shows the simulated surface potential evolution as a function of SRV ranging from 0.1 to 1000 cm/s, spanning the range of expected experimental values for untreated and treated films,[12,13,16,36] and **Figure 4.3b** shows the simulated surface potential equilibration time plotted against SRV. As we decrease SRV, the simulated surface potential takes longer to reach the new steady-state, in agreement with the experimental trends from trEFM (**Figure 4.2b**). This result is consistent with general behavior of rate equations and approach to equilibrium, where carrier generation rate is equal to recombination rate: if we decrease the recombination rate by suppressing SRV, then we will reach equilibrium more slowly (see **Appendix C Note 4**). While we are not attempting to simulate the full 3D system quantitatively, the excellent qualitative agreement between the experimental and simulated timescales further supports our physical interpretation that changes in surface potential equilibration times upon passivation (**Figure 4.2a,b**) are primarily due to suppression of SRV. **Appendix C Figures S8-9** show the relationship

between simulated surface potential equilibration time and bulk nonradiative and bimolecular recombination processes. **Appendix C Table 3** contains complete simulation parameter details.

We next turn to interpreting the slower trEFM kinetics at the grain boundaries observed in our unpassivated samples. So far, we have established that known reductions in nonradiative recombination result in slower surface potential equilibration times, clearly showing that trEFM dynamics correlate with minority carrier lifetimes and SRVs. However, **Figure 4.2d** shows that defect-rich grain boundaries in unpassivated samples also exhibit relatively slower equilibration times. In our previous work on 2D butylammonium lead iodide (BA_2PbI_4) perovskite materials, we also observed slower trEFM dynamics at grain boundaries, which we proposed are caused by increased contributions from slow ionic motion or trap-mediated electronic carrier transport.[31]

We now support this hypothesis with additional simulations of ion motion. **Figure 4.3c** shows the simulated surface potential evolution as a function of the mobile ion concentration ranging from 1×10^{14} cm^{-3} to 1×10^{17} cm^{-3}, fixing the ion diffusion coefficient at 1×10^{-13} cm^2s^{-1} (parameter details are available in **Appendix C Table 3**).[64–70] **Figure 4.3d** shows the simulated equilibration times as a function of mobile ion concentration, where higher mobile ion concentrations result in relatively slower surface potential equilibration times. This observation is supported by Poisson's Equation: as we increase the mobile ion concentration, the contribution of slow ion motion to the surface potential dynamics increases, thus lengthening the equilibration times (see **Appendix C Note 4** for further discussion).[63] These results suggest that slower surface potential equilibration times measured at grain boundaries indeed result from higher local mobile ion concentrations.

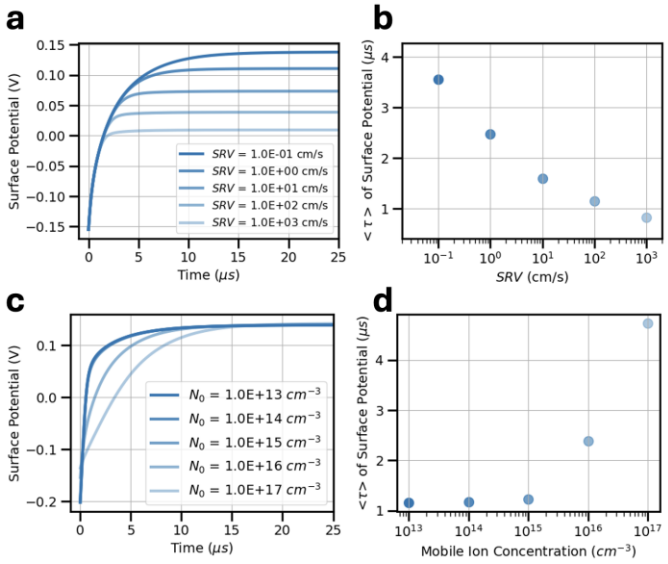

Figure 4.3: Drift-diffusion simulations reveal influence of SRV and mobile ions on surface potential evolution. (a) Simulated surface potential evolutions plotted against time with varied SRV. (b) The average time constants describing the simulated surface potential equilibration times with respect to SRV, showing slower equilibration behavior at lower SRVs. (c) Simulated surface potential evolutions with varied mobile ion concentrations. (d) Average time constant that describes the equilibration of the simulated surface potential traces with respect to mobile ion concentration (N_0, cm^{-3}), showing slower equilibration behavior at higher mobile ion concentrations. For complete simulation parameter details see **Appendix C Table 3**.

To better understand the slower dynamics at grain boundaries, we explore the effect of different background illuminations intensities on the trEFM dynamics. Background illumination creates a population of mobile electronic carriers which can screen charged defects, such as halide vacancies or charge traps, masking their influence on observed dynamics. We thus expect background illumination bias should have two net effects: (1) the surface potential equilibration times should become faster due to overall higher electronic carrier concentrations reducing the marginal contribution from slower ionic processes, and (2) the observed contrast between grain

boundaries and grain interiors should homogenize due to screening of both mobile ions and charge traps.

Figure 4.4 presents data consistent with both these expectations. We apply a continuous illumination bias to the ROI using an LED with a peak wavelength of 660 nm. While under this constant illumination bias, we use the 405 nm laser at 110 mW/cm^2 incident intensity to photoexcite the sample for trEFM imaging. We vary the illumination bias intensity from 0 mW/cm^2 to 100 mW/cm^2. **Figure 4.4a** shows the representative topography of the ROI, with the characteristic nanoscale grains. **Figure 4.4b-e** show the surface potential equilibration time maps measured by trEFM according to increasing illumination bias intensity (where **Figure 4.4f** returns to 0 mW/cm^2). Consistent with our hypothesis, **Figure 4.4** shows that with increasing background illumination intensity, the average equilibration time becomes faster, consistent with our hypothesis above. **Figure 4.4g** shows the surface potential equilibration times for grain boundaries and interiors plotted against illumination bias intensity. We see that with increasing illumination bias, the difference between grain boundaries and interiors decreases, again consistent with our hypothesis (**Appendix C Figures S10-14** for detailed analysis and replicated results with 660 nm and 455 nm illumination biases). Overall, these results are consistent with our earlier observations and drift-diffusion simulations in both overall equilibration times, and the intensities/photocarrier densities required to mask the grain boundary signals.

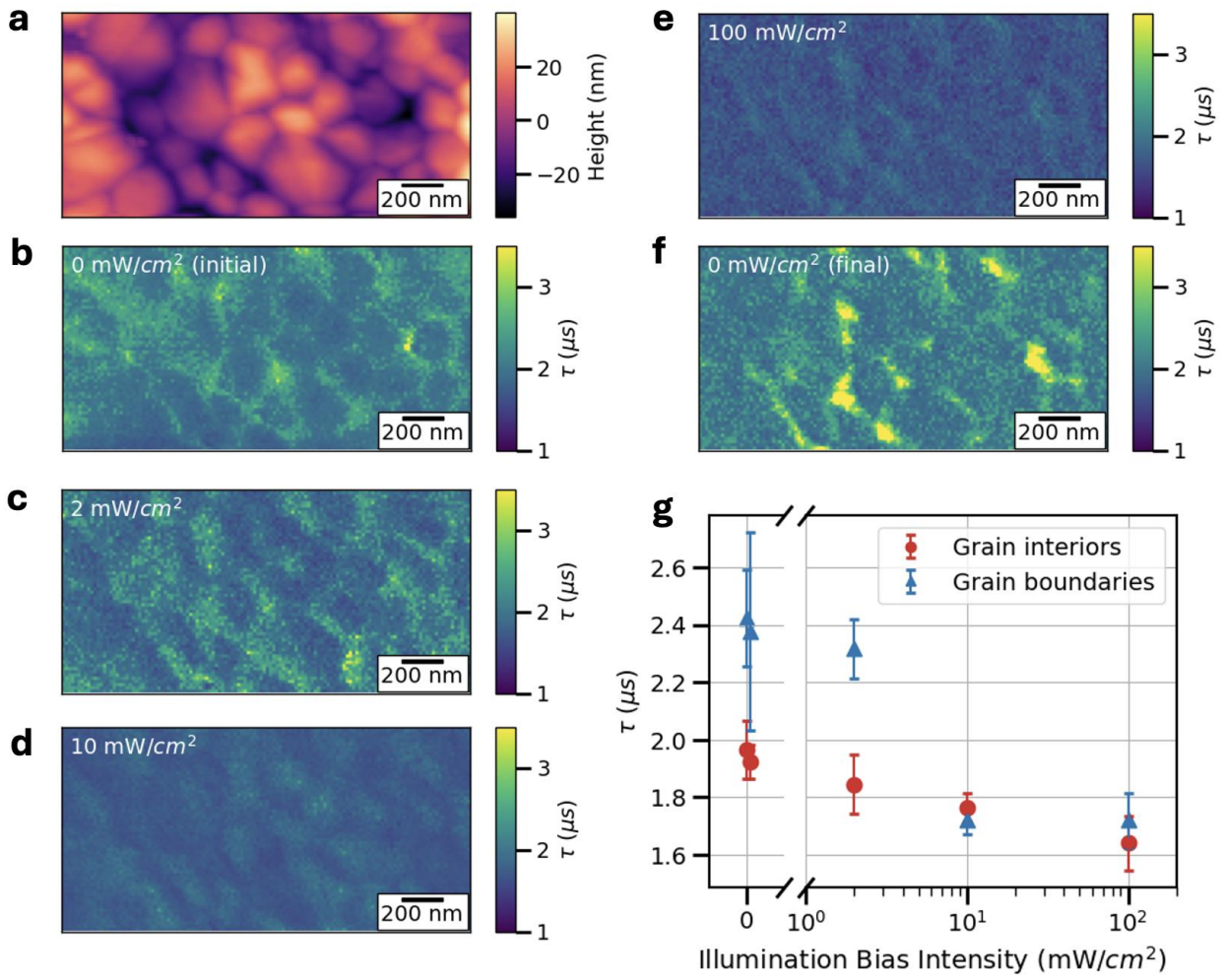

Figure 4.4: Surface potential equilibration with varying background illumination bias intensity. (a) Topography of 2×1 μm ROI. (b)-(e) Images of surface potential equilibration time constants taken in the same ROI with increasing 660 nm bias illumination intensity ranging from 0 mW/cm^2 to 100 mW/cm^2, with a step-edge 405 nm laser at 110 mW/cm^2 used for trEFM excitation. (f) Reproduced trEFM time constant image at 0 mW/cm^2 showing return to unbiased time constants. (g) Average grain interior and boundary trEFM time constants with respect to background illumination bias intensity, error bars show standard deviation of masked pixel selection (**Appendix C Figure S10**).

We stress test our model and interpretation with both intensity-dependent and wavelength-dependent trPL and trEFM measurements. **Appendix C Figures S15-19** and **Table 4** show the detailed analysis of these experiments and simulations, which are broadly consistent with our interpretation. First, at higher excitation intensities we observe both faster trPL and faster trEFM signatures, consistent with higher order recombination processes and a correspondingly faster approach to equilibrium. Second, since we are exciting the half-stacks through the ITO with the cantilever at the perovskite surface, redder wavelength illumination photoexcites carriers closer to the surface of the film, resulting in a greater contribution from SRV to the surface potential equilibration time.

Putting the experiment and simulation results together, **Figure 4.5a** illustrates the key factors that influence the surface potential dynamics: the local mobile ion concentration and SRV. **Figure 4.5b** shows simulated surface potential evolutions given parameters that approximate unpassivated and passivated grain boundaries and interiors. In the unpassivated regime, slightly higher mobile ion concentrations (grain boundaries) result in slightly slower equilibration times. In the passivated regime, upon the suppression of SRV and reduction in mobile ion concentration[18,19] the equilibration times become slower and indistinguishable. These results suggest that the heterogeneity we observe in surface potential equilibration times after passivation (**Figure 4.2f**) is primarily due to local variations in SRV. This work highlights trEFM's ability to diagnose passivator uniformity and efficiency on the nanoscale.

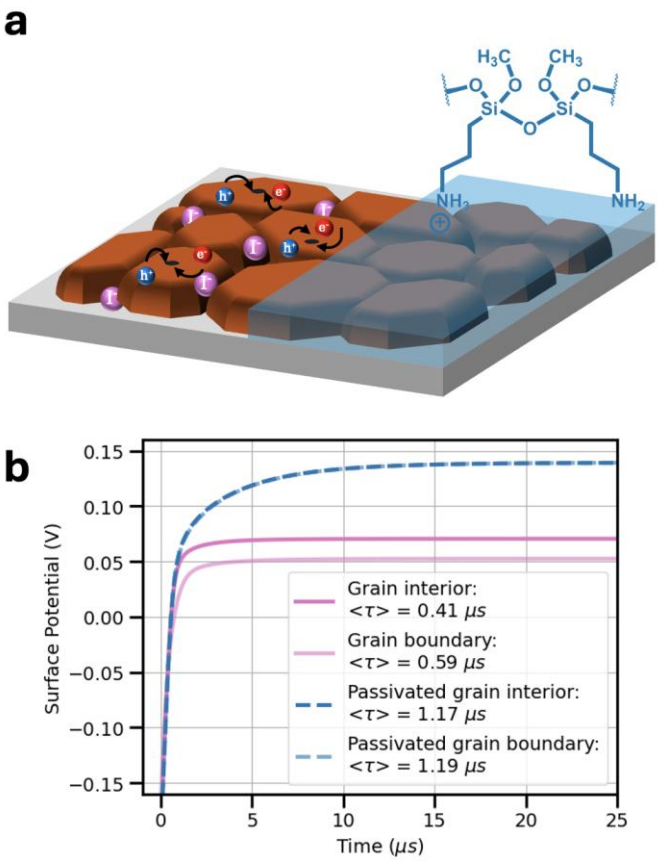

Figure 4.5: Illustration of mobile ions and SRV, which influence surface potential evolution, supported by drift-diffusion simulations. (a) Illustration describing the effects of SRV and slow ion migration, which are both reduced by surface passivation with APTMS. (b) Drift-diffusion simulations of the surface potential where the primary difference between the grain interior and grain boundary is the concentration of mobile ions (1×10^{15} cm^{-3} and 5×10^{15} cm^{-3} respectively) with a SRV of 100 cm/s; simulated surface potential evolution of passivated grain interiors and boundaries have both reduced mobile ion concentrations and suppressed SRV values (5×10^{14} cm^{-3} and 1×10^{15} cm^{-3} for grain interiors and boundaries respectively, with a SRV of 0.1 cm/s). Note that there are two blue, dashed traces representing the passivated condition that are indistinguishable. For complete simulation parameters see **Appendix C Table 3**.

4.4 Conclusions

We demonstrate that in halide perovskites, trEFM probes local surface potential equilibration time, which is influenced by both electronic carrier recombination and mobile ions. We show that passivation results in slower equilibration times due to strong suppression of SRV, and we directly correlate these equilibration dynamics to SRV obtained from trPL. Importantly, we reveal local variations in SRV after surface passivation using trEFM, demonstrating the need to optimize passivation treatments. Additionally, we conclude that slower equilibration times observed at grain boundaries in unpassivated samples are caused by higher defect concentrations that result in increased contributions of slow ion motion to the surface potential dynamics. These advances highlight the ability to characterize not only the impact of perovskite nanostructure on local carrier dynamics, but also to evaluate the effectiveness of passivation below the optical diffraction limit at length scales relevant to modern halide perovskites. We anticipate the use of sub-diffraction-limited imaging of carrier recombination dynamics to optimize perovskite semiconductor devices and passivation treatments down to the nanoscale.

4.5 Acknowledgements

The atomic force microscopy imaging work (M.D.B., J.P., R.G.) was supported by the U.S. Department of Energy, Office of Basic Energy Sciences, Division of Materials Sciences and Engineering under Award DE-SC0013957. Part of this work was carried out at the Molecular Analysis Facility, a National Nanotechnology Coordinated Infrastructure site at the University of Washington, which is supported by the National Science Foundation (NNCI-1542101), the Molecular Engineering and Sciences Institute, and the Clean Energy Institute. M.D.B. acknowledges support from the NSF Graduate Student Fellowship program under Grant no. DGE-2140004. M.D.B. thanks Nir Tessler for advice on drift-diffusion simulations. J.P. thanks Zixu

Huang for help with XRD measurements. D.S.G acknowledges salary and infrastructure support from the Washington Research Foundation, the Alvin L. and Verla R. Kwiram endowment, and the B. Seymour Rabinovitch Endowment.

4.6 References

(1) Zhang, H., Pfeifer, L., Zakeeruddin, S. M., Chu, J. & Grätzel, M. Tailoring passivators for highly efficient and stable perovskite solar cells. *Nat. Rev. Chem.* **7**, 632–652 (2023).

(2) Stranks, S. D. & Snaith, H. J. Metal-halide perovskites for photovoltaic and light-emitting devices. *Nat. Nanotech.* **10**, 391–402 (2015).

(3) Li, M. *et al.* Acceleration of radiative recombination for efficient perovskite LEDs. *Nature* **630**, 631–635 (2024).

(4) Wei, H. & Huang, J. Halide lead perovskites for ionizing radiation detection. *Nat. Commun.* **10**, 1066 (2019).

(5) Nguyen, H. A. *et al.* Design Rules for Obtaining Narrow Luminescence from Semiconductors Made in Solution. *Chem. Rev.* **123**, 7890–7952 (2023).

(6) Eperon, G. E., Horantner, M. T. & Snaith, H. J. Metal halide perovskite tandem and multiple-junction photovoltaics. *Nat. Rev.* **1**, 0095 (2017).

(7) Dequilettes, D. W. *et al.* Photoluminescence Lifetimes Exceeding 8 μs and Quantum Yields Exceeding 30% in Hybrid Perovskite Thin Films by Ligand Passivation. *ACS Energy Lett.* **1**, 438–444 (2016).

(8) DeQuilettes, D. W. *et al.* Impact of microstructure on local carrier lifetime in perovskite solar cells. *Science* **348**, 683–686 (2015).

(9) Jariwala, S. *et al.* Local Crystal Misorientation Influences Non-radiative Recombination in Halide Perovskites. *Joule* **3**, 3048–3060 (2019).

(10) Kim, G.-W. & Petrozza, A. Defect Tolerance and Intolerance in Metal-Halide Perovskites 2. Defects in Perovskite Solar Cells: Efficiency versus Stability. *Adv. Energy Mater.* **10**, 2001959 (2020).

(11) De Keersmaecker, M., Tirado, J., Armstrong, N. R. & Ratcliff, E. L. Defect Quantification in Metal Halide Perovskites Anticipates Photoluminescence and Photovoltaic Performance. *ACS Energy Lett* **9**, 243–252 (2024).

(12) Dequilettes, D. W. *et al.* Reduced recombination via tunable surface fields in perovskite thin films. *Nat Energy* **9**, 457–466 (2024).

(13) Wang, J. *et al.* Reducing Surface Recombination Velocities at the Electrical Contacts Will Improve Perovskite Photovoltaics. *ACS Energy Lett.* **14**, 222–227 (2019).

(14) Lin, Y. H. *et al.* Bandgap-universal passivation enables stable perovskite solar cells with low photovoltage loss. *Science* **384**, 767–775 (2024).

(15) Shi, Y. *et al.* (3-Aminopropyl)trimethoxysilane Surface Passivation Improves Perovskite Solar Cell Performance by Reducing Surface Recombination Velocity. *ACS Energy Lett.* **7**, 4081–4088 (2024).

(16) Jariwala, S. *et al.* Reducing surface recombination velocity of methylammonium-free mixed-cation mixed-halide perovskites via surface passivation. *Chem. Mater.* **33**, 5035–5044 (2021).

(17) Rigter, S. A. *et al.* Passivation Properties and Formation Mechanism of Amorphous Halide Perovskite Thin Films. *Adv. Func. Mater.* **31**, 2010330 (2021).

(18) Akrami, F., Jiang, F., Giridharagopal, R. & Ginger, D. S. Kinetic Suppression of Photoinduced Halide Migration in Wide Bandgap Perovskites via Surface Passivation. *J. Phys. Chem. Lett* **14**, 9310–9315 (2023).

(19) Pothoof, J., Westbrook, R. J. E., Giridharagopal, R., Breshears, M. D. & Ginger, D. S. Surface Passivation Suppresses Local Ion Motion in Halide Perovskites. *J. Phys. Chem. Lett* **14**, 6092–6098 (2023).

(20) Jiang, F. *et al.* Scanning Kelvin Probe Microscopy Reveals That Ion Motion Varies with Dimensionality in 2D Halide Perovskites. *ACS Energy Lett.* **6**, 100–108 (2021).

(21) McGovern, L. *et al.* Reduced Barrier for Ion Migration in Mixed-Halide Perovskites. *ACS Appl Energy Mater* **4**, 13431–13437 (2021).

(22) Liu, Y. *et al.* Direct Observation of Photoinduced Ion Migration in Lead Halide Perovskites. *Adv. Funct. Mater.* **31**, 2008777 (2020).

(23) Jiang, F. *et al.* Improved reverse bias stability in p-i-n perovskite solar cells with optimized hole transport materials and less reactive electrodes. *Nat. Energy* **9**, 1275–1284 (2024).

(24) Weber, S. A. L. *et al.* How the formation of interfacial charge causes hysteresis in perovskite solar cells. *Energy Environ. Sci.* **11**, 2404–2413 (2018).

(25) Liu, J. *et al.* Correlations between Electrochemical Ion Migration and Anomalous Device Behaviors in Perovskite Solar Cells. *ACS Energy Lett.* **6**, 1003–1014 (2021).

(26) Jones, T. W. *et al.* Lattice strain causes non-radiative losses in halide perovskites. *Energy Environ Sci* **12**, 596–606 (2019).

(27) Tennyson, E. M., S Doherty, T. A. & Stranks, S. D. Heterogeneity at multiple length scales in halide perovskite semiconductors. *Nat. Rev.* **4**, 573–587 (2019).

(28) Frohna, K. *et al.* The impact of interfacial quality and nanoscale performance disorder on the stability of alloyed perovskite solar cells. *Nat Energy* (2024) doi:10.1038/s41560-024-01660-1.

(29) Delport, G., Macpherson, S. & Stranks, S. D. Imaging Carrier Transport Properties in Halide Perovskites using Time-Resolved Optical Microscopy. *Adv. Energy Mater.* **10**, 1903814 (2020).

(30) Giridharagopal, R., Cox, P. A. & Ginger, D. S. Functional Scanning Probe Imaging of Nanostructured Solar Energy Materials. *Acc. Chem. Res.* **49**, 1769–1776 (2016).

(31) Giridharagopal, R. *et al.* Time-Resolved Electrical Scanning Probe Microscopy of Layered Perovskites Reveals Spatial Variations in Photoinduced Ionic and Electronic Carrier Motion. *ACS Nano* **13**, 2812–2821 (2019).

(32) Guthrey, H. & Moseley, J. A Review and Perspective on Cathodoluminescence Analysis of Halide Perovskites. *Adv. Energy Mater.* **10**, 1903840 (2020).

(33) Zhou, Y., Herz, L. M., Jen, A. K.-Y. & Saliba, M. Advances and challenges in understanding the microscopic structure–property–performance relationship in perovskite solar cells. *Nat. Energy* **7**, 794–807 (2022).

(34) Tennyson, E. M. *et al.* Correlated Electrical and Chemical Nanoscale Properties in Potassium-Passivated, Triple-Cation Perovskite Solar Cells. *Adv. Mater. Interaces* **7**, 2000515 (2020).

(35) Collins, S. D. *et al.* Observing Ion Motion in Conjugated Polyelectrolytes with Kelvin Probe Force Microscopy. *Adv Electron Mater* **3**, 1700005 (2017).

(36) Taddei, M. *et al.* Interpreting Halide Perovskite Semiconductor Photoluminescence Kinetics. *ACS Energy Lett.* **9**, 2508–2516 (2024).

(37) Yuan, Y. *et al.* Shallow defects and variable photoluminescence decay times up to 280 μs in triple-cation perovskites. *Nature Materials* | **23**, 391–397 (2024).

(38) Xiong, S. *et al.* Reducing nonradiative recombination for highly efficient inverted perovskite solar cells via a synergistic bimolecular interface. *Nat. Commun.* **15**, 5607 (2024).

(39) Zhao, K. *et al.* peri-Fused polyaromatic molecular contacts for perovskite solar cells. *Nature* **632**, 301–306 (2024).

(40) Rehman, W. *et al.* Photovoltaic mixed-cation lead mixed-halide perovskites: links between crystallinity, photo-stability and electronic properties. *Energy Environ. Sci* **10**, 361–369 (2017).

(41) Bischak, C. G., Sanehira, E. M., Precht, J. T., Luther, J. M. & Ginsberg, N. S. Heterogeneous Charge Carrier Dynamics in Organic−Inorganic Hybrid Materials: Nanoscale Lateral and Depth-Dependent Variation of Recombination Rates in Methylammonium Lead Halide Perovskite Thin Films. *ACS Nano Lett.* **15**, 4799–4807 (2015).

(42) Dwyer, R. P., Harrell, L. E. & Marohn, J. A. Lagrangian and Impedance-Spectroscopy Treatments of Electric Force Microscopy. *Phys. Rev. Appl.* **11**, 64020–64052 (2019).

(43) Tirmzi, A. M., Dwyer, R. P., Jiang, F. & Marohn, J. A. Light-Dependent Impedance Spectra and Transient Photoconductivity in a Ruddlesden-Popper 2D Lead-Halide Perovskite Revealed

by Electrical Scanned Probe Microscopy and Accompanying Theory. *J. Phys. Chem. C* **124**, 13639–13648 (2020).

(44) Albrecht, T. R., Grütter, P., Horne, D. & Rugar, D. Frequency modulation detection using high-Q cantilevers for enhanced force microscope sensitivity. *J. Appl. Phys.* **69**, 668–673 (1991).

(45) Miyahara, Y., Cockins, L. & Grütter, P. Electrostatic Force Microscopy Characterization of Low Dimensional Systems. in *Kelvin Probe Force Microscopy* (eds. Sadewasser, A. & Glatzel, T.) vol. 48 177–199 (Springer, Berlin, Heidelberg).

(46) Collins, L. *et al.* Breaking the Time Barrier in Kelvin Probe Force Microscopy: Fast Free Force Reconstruction Using the G-Mode Platform. *ACS Nano* **11**, 8717–8729 (2017).

(47) Coffey, D. C. & Ginger, D. S. Time-resolved electrostatic force microscopy of polymer solar cells. *Nat. Mater.* **5**, 735–740 (2006).

(48) Karatay, D. U., Harrison, J. S., Glaz, M. S., Giridharagopal, R. & Ginger, D. S. Fast time-resolved electrostatic force microscopy: Achieving sub-cycle time resolution. *Rev. Sci. Instrum.* **87**, 053702 (2016).

(49) Giridharagopal, R. *et al.* Submicrosecond time resolution atomic force microscopy for probing nanoscale dynamics. *Nano Lett.* **12**, 893–898 (2012).

(50) Cox, P. A. *et al.* Imaging Charge Transfer State Excitations in Polymer/Fullerene Solar Cells with Time-Resolved Electrostatic Force Microscopy. *J. Phys. Chem. Lett.* **6**, 2852–2858 (2015).

(51) Reid, O. G., Rayermann, G. E., Coffey, D. C. & Ginger, D. S. Imaging Local Trap Formation in Conjugated Polymer Solar Cells: A Comparison of Time-Resolved Electrostatic Force Microscopy and Scanning Kelvin Probe Imagin. *J. Phys. Chem. C.* **114**, 20672–20677 (2010).

(52) Shao, G., Rayermann, G. E., Smith, E. M. & Ginger, D. S. Morphology-Dependent Trap Formation in Bulk Heterojunction Photodiodes. *J. Phys. Chem. B* **117**, 4654–4660 (2013).

(53) Breshears, M. D., Giridharagopal, R., Pothoof, J. & Ginger, D. S. A Robust Neural Network for Extracting Dynamics from Electrostatic Force Microscopy Data. *J. Chem. Inf. Model.* **62**, 4342–4350 (2022).

(54) Teale, S., Degani, M., Chen, B., Sargent, E. H. & Grancini, G. Molecular cation and low-dimensional perovskite surface passivation in perovskite solar cells. *Nat. Energy* **9**, 779–792 (2024).

(55) Jiang, Q. *et al.* Surface passivation of perovskite film for efficient solar cells. *Nat. Photonics* **13**, 460–466 (2019).

(56) Thornton, S. T. & Marion, J. B. Classical Dynamics of Particles and Systems. in *Classical Dynamics of Particles and Systems* 100–117 (Thomsom Brooks/Cole, 2004).

(57) Taddei, M. *et al.* Ethylenediamine Addition Improves Performance and Suppresses Phase Instabilities in Mixed-Halide Perovskites. *ACS Energy Lett.* **7**, 4265–4273 (2022).

(58) Xu, J. *et al.* Triple-halide wide–band gap perovskites with suppressed phase segregation for efficient tandems. *Science* **367**, 1097–1104 (2020).

(59) Wang, R. *et al.* Constructive molecular configurations for surface-defect passivation of perovskite photovoltaics. *Science* **366**, 1509–1513 (2019).

(60) Johnston, M. B. & Herz, L. M. Hybrid Perovskites for Photovoltaics: Charge-Carrier Recombination, Diffusion, and Radiative Efficiencies. *Acc. Chem. Res.* **49**, 146–154 (2016).

(61) Courtier, N. E., Richardson, G. & Foster, J. M. A fast and robust numerical scheme for solving models of charge carrier transport and ion vacancy motion in perovskite solar cells. *Appl. Math. Model.* **63**, 329–348 (2018).

(62) Courtier, N. E., Cave, J. M., Foster, J. M., Walker, A. B. & Richardson, G. How transport layer properties affect perovskite solar cell performance: insights from a coupled charge transport/ion migration model. *Energy Environ. Sci* **12**, 396–409 (2019).

(63) Courtier, N. E., Cave, · J M, Walker, · A B, Richardson, · G & Foster, · J M. IonMonger: a free and fast planar perovskite solar cell simulator with coupled ion vacancy and charge carrier dynamics. *J Comput Electron* **18**, 1435–1449 (2019).

(64) Peng, W. *et al.* Quantification of Ionic Diffusion in Lead Halide Perovskite Single Crystals. *ACS Energy Lett.* **3**, 1477–1481 (2018).

(65) Futscher, M. H. *et al.* Quantification of ion migration in CH3NH3PbI 3 perovskite solar cells by transient capacitance measurements. *Mater. Horiz.* **6**, 1497–1503 (2019).

(66) Yun, J. S. *et al.* Critical Role of Grain Boundaries for Ion Migration in Formamidinium and Methylammonium Lead Halide Perovskite Solar Cells. *Adv. Energy Mater.* **6**, 1600330 (2016).

(67) Siekmann, J., Ravishankar, S. & Kirchartz, T. Apparent Defect Densities in Halide Perovskite Thin Films and Single Crystals. *ACS Energy Lett.* **6**, 3244–3251 (2021).

(68) Eames, C. *et al.* Ionic transport in hybrid lead iodide perovskite solar cells. *Nat. Commun.* **6**, 7497 (2015).

(69) Wu, N., Walter, D., Fell, A., Wu, Y. & Weber, K. The Impact of Mobile Ions on the Steady-State Performance of Perovskite Solar Cells. *J. Phys. Chem. C* **124**, 219–229 (2020).

(70) Mcgovern, L. *et al.* Reduced Barrier for Ion Migration in Mixed-Halide Perovskites. *Appl. Energy Mater.* **4**, 13431–13437 (2021).

Appendix A: Supporting Information for Chapter 2

A1. Materials and Methods

1.1 Materials

All materials were purchased from Sigma-Aldrich or Alfa Aesar and used as received, unless otherwise stated. Butylammonium iodide (BAI) and methylammonium iodide (MAI) were purchased from GreatCell Solar Ltd.

1.2 Film preparation and device fabrication

All perovskite devices for SKPM measurement, with the structure of glass/perovskite/PMMA/SiO_x/Au, were prepared on glass substrates. The glass substrates were sonicated in baths using detergent in de-ionized water, de-ionized water, acetone and 2-propanol in sequence. BA_2PbI_4 (n=1) perovskite solution was prepared by dissolving 1.8 M butylammonium iodide (BAI) and 0.9 M lead (II) iodide (PbI_2) in dimethylformamide (DMF). $BA_2MA_3Pb_4I_{13}$ (~<n>=4) perovskite solution was prepared by dissolving 0.5 M BAI, 0.75 M methylammonium iodide (MAI), and 1.0 M PbI_2 in DMF. The perovskite solutions were spin coated on plasma-treated substrates at 4000 rpm for 40 s, followed by thermal annealing at 100 °C for 10 minutes. For $BA_2MA_3Pb_4I_{13}$ (~<n>=4) films, the glass substrates were pre-heated on a hot plate at 130 °C, employing the hot casting method to fabricate the perovskite films.[1] The thickness of the BA_2PbI_4 (n=1) and $BA_2MA_3Pb_4I_{13}$ (~<n>=4) perovskite films was around 500 nm and 300 nm respectively. The PMMA layer, with a thickness of ~ 160 nm as measured by profilometry, was spin-coated from chloroform solution (25 mg/mL) at 4000 rpm for 40 s. On top of the PMMA layer, >65 nm thick SiO_x layer was e-beam evaporated. Finally, 70 nm gold electrodes were thermally evaporated on top, and junctions with width ranging between ~8 μm and ~13 μm were created using commercial tungsten wires of varied width on the evaporation mask. We have also replaced the PMMA layer with another insulating polymer polystyrene (PS)

1.3 Scanning Kelvin force microscopy measurement

Scanning Kelvin probe microscopy (SKPM) measures the contact potential difference (CPD, where $V_{CPD} = (\phi_{tip} - \phi_{sample})/-e$) between the work functions of the tip (ϕ_{tip}) and sample (ϕ_{sample}). The CPD measurement can be in principle an extremely useful tool to gain information concerning the work function, dopant concentration, and charge distribution of the sample being measured. Unless otherwise stated, all the SKPM measurements were conducted at room temperature (T = ~25 °C). Details for the measurement are as follows: Devices were imaged in a flow cell under nitrogen protection. The SKPM measurements were carried out using an Asylum Research MFP-3D (Oxford Instruments) atomic force microscope mounted on an inverted Nikon

Eclipse microscope and a customized piezo-stage. Cr/Pt-coated silicon tips (MikroMasch, 325 kHz, 40 N/m) were used to probe the SKPM signal. During the measurement, the cantilever was oriented parallel to the junction and the scanning was carried out in the direction perpendicular to the junction. Single line scans were achieved by measuring the same line across the electrode gap repeatedly, and each line measurement took around 16 – 17 s to finish. The two gold electrodes at the two ends of the junctions were connected to a Keithley 2400 power supply, with one side grounded and the other side biased with a +9 V bias. The SKPM measurement was conducted in a frequency-modulated mode, which allows electrical characterization with better sensitivity compared to conventional amplitude-modulated mode. An AC bias was applied to the tip (700 kHz, 2 V peak-to-peak) from an Agilent 15 MHz Function/Arbitrary Waveform Generator. The electrostatic tip-sample interactions induce the oscillation of the cantilever, the cantilever oscillation is isolated using a lock-in-amplifier (Stanford Research Systems Model SR830) and set to a feedback circuit. The feedback circuit tries to minimize the frequency shift by applying a DC bias to the tip (referred to as V_{DC} or V_{tip}). Since the V_{tip} is the potential applied to the tip to nullify the CPD, the CPD in principle can be calculated simply by taking the inverse additive of V_{tip}. All of the potential curves shown in this study refer to V_{tip} unless otherwise stated. Meanwhile, for the light intensity dependent SKPM measurement, a 455 nm blue LED (LEDEngin LZ4) was coupled and focused through the microscope optics onto the sample where the AFM tip was placed. The temperature dependent SKPM measurements were completed in an Asylum Research Cypher ES Environment, with a temperature-controllable stage to adjust the temperatures. All of the potential profiles shown in the manuscript and supporting information are given by assuming the contact potential difference between the tip and the gold electrode as zero.

1.4 X-ray diffraction measurement

The X-ray diffraction measurements of BA_2PbI_4 (n=1) and $BA_2MA_3Pb_4I_{13}$ (~<n>=4) perovskite films on glass substrates were conducted using a Bruker D8 Discover with a Pilatus 100 K large-area 2D detector (Cu Kα radiation at 50,000 mW).

1.5 UV-Vis Absorbance measurement.

UV-Vis absorbance spectra of the BA_2PbI_4 (n=1) and $BA_2MA_3Pb_4I_{13}$ (~<n>=4) perovskite films on glass substrates were recorded on an Agilent 8453 UV-Vis Spectrometer in a range of 400 – 800 nm and an integration time of 0.5 s.

1.6 Activation Energy (E_a) calculations.

At each timestep, the positive and negative potential peak values were extracted at 283, 293, 303, and 313 K for BA_2PbI_4 (n=1) and $BA_2MA_3Pb_4I_{13}$ (~<n>=4) in the dark and under illumination. Those values were then fitted with either single- or bi-exponential functions and the

decay rates were extracted for the positive and negative potential values at all temperatures. In the case of bi-exponential fits, the decay rate was calculated as the weighted average of the two decay rates. The decay rates were then plotted against temperature and fitted to the Arrhenius equation using a non-linear ordinary distance regression. In the fit, errors in the temperature were assumed to be ± 2 K and errors in the decay rate were assumed to be ± 10% of the decay rate value at each data point to account for instrumental error. From this fit, activation energies were calculated for positive and negative potential peaks (charge pairs) in the dark and in the light for BA_2PbI_4 (n=1) and $BA_2MA_3Pb_4I_{13}$ (~<n>=4).

1.7 Drift-Diffusion Simulations

1-D Drift-diffusion simulations were performed on COMSOL Multiphysics 5.5, using a Nernst–Planck-Poisson interface that combines electrostatics and transport of diluted species. As there are no convections and magnetic fields in our system, the equations governing the charge dynamics become

$$\frac{\partial c}{\partial t} = -\nabla \cdot J \tag{1}$$

$$J = -(D\nabla c + \frac{Dze}{k_B T} c \cdot \nabla \mathrm{V}) \tag{2}$$

where J is the diffusion flux density, t is time, D is the diffusivity of the chemical species, c is the concentration of the species, z is the valence of ionic species, e is the elementary charge, k_B is the Boltzmann constant, T is the temperature, and V is the electric potential. For the boundary condition, we set no electronic carrier or ionic species exchange with the electrode (or the materials underneath the electrode, as we performed 1D simulation whereas the real device is a 3D stack), i.e. $J(0)=J(L)=0$, where L is the channel length $10\mu m$.

We set the charge of cations and anions to be +1 and -1, respectively. We also add electrons and holes, of which the mobilities are set to be ~10 cm^2/Vs, corresponding to a diffusivity D ~ 0.26 cm^2/s, and the concentrations are listed in **Figure S4**. We note that, though the model is not particularly designed for semiconductor simulations, it should be valid for electronic carriers at the chosen low concentrations as those are still in the Maxwell-Boltzmann regime. We also note that the mobilities of ionic species are on the order of 10^{-10}~10^{-9} cm^2/Vs, which differentiate them from the electronic carriers in the modeled system. For the space charges, i.e. the p-dopants or n-dopants, we set their diffusivities D to be zero. The potential distribution shown in **Figure S4** is at 10 ms after applying the voltage. Indeed, due to the more than 10 orders of magnitude mobility difference between the electronic carriers and ionic species, the potential distribution remains 'static' over the time range of microseconds to the first few seconds, *regardless of the ionic species input*, which is referred as the electronic equilibrium condition. As noted in the main text, the ionic charging process may be a result of the electric field induced by electronic carriers, as the electronic carriers screen the applied electric field and drift on a timescale orders of magnitude faster than ionic carriers.

A2. Supplementary figures and discussions

2.1 Perovskite film morphologies

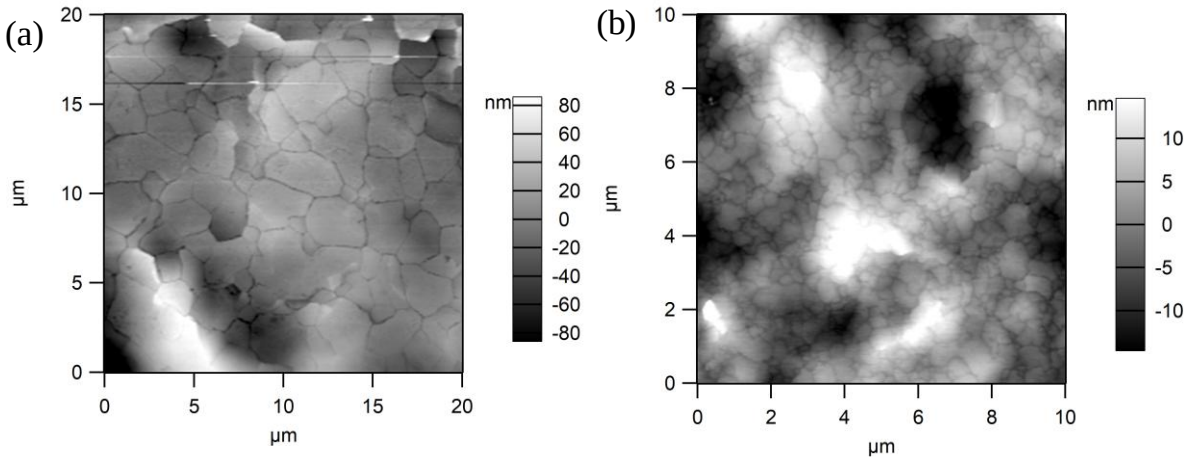

Figure S1. The top-view morphologies of the as-fabricated (a) 2D BA_2PbI_4 (n=1) and (b) quasi-2D $BA_2MA_3Pb_4I_{13}$ (~<n>=4) perovskite films.

The top-view morphologies of perovskite films on glass substrates were obtained by atomic force microscopy in the tapping mode. Both the BA_2PbI_4 (n=1) and $BA_2MA_3Pb_4I_{13}$ (~<n>=4) perovskite films show good crystallinity with flat and compact morphologies. The grain sizes for the BA_2PbI_4 (n=1) perovskite films are up to several micrometers, while around several hundred nanometers for the $BA_2MA_3Pb_4I_{13}$ (~<n>=4) perovskite films.

2.2 UV-Vis Absorbance spectra.

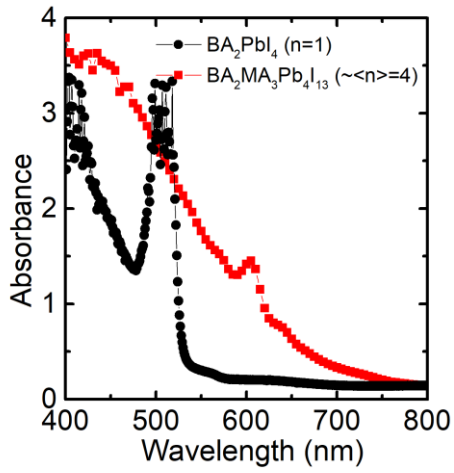

Figure S2. The UV-Vis absorbance spectra of the as-fabricated 2D BA_2PbI_4 (n=1) and quasi-2D $BA_2MA_3Pb_4I_{13}$ (~<n>=4) perovskite films.

For the BA_2PbI_4 (n=1) perovskite film, we observed a strong excitonic peak at the wavelength of ~500 nm. The excitonic peak is the result of the quantum confinement in the inorganic spaces as well as the dielectric mismatch between the inorganic and organic layers.[2, 3] The excitonic peak was not completely captured because its intensity exceeded the limit of the equipment. In contrast, the $BA_2MA_3Pb_4I_{13}$ (~<n>=4) perovskite film shows more broaden absorption range, with the absorption edge extending to around ~780 nm, and with several small excitonic peaks at wavelengths between 600 nm and 750 nm. This indicates that the as-fabricated $BA_2MA_3Pb_4I_{13}$ perovskite films is a mixture of 3D perovskites and 2D perovskites of varied n value.

2.3 X-ray diffraction patterns.

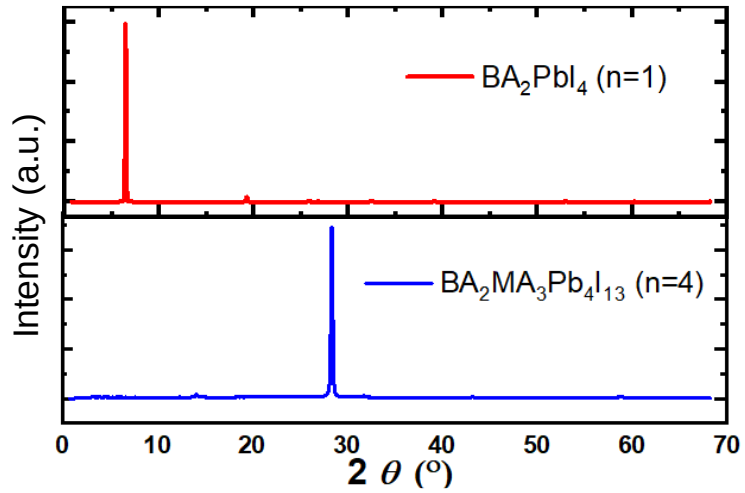

Figure S3. The X-ray diffraction patterns of the 2D BA_2PbI_4 (n=1) and quasi-2D $BA_2MA_3Pb_4I_{13}$ (~<n>=4) perovskite films.

For the BA_2PbI_4 (n=1) perovskite film, the main diffraction peak (2θ = 6.42 °) corresponds to the (002) plane, indicating the in-plane orientation of the perovskites.[4] For the $BA_2MA_3Pb_4I_{13}$ (~<n>=4) perovskite films, the main diffraction peak (2θ = 28.40°) corresponds to the (202) plane, indicating the out-of-plane orientation of the perovskites.[1]

2.4 Drift-Diffusion simulations at the electronic equilibrium condition

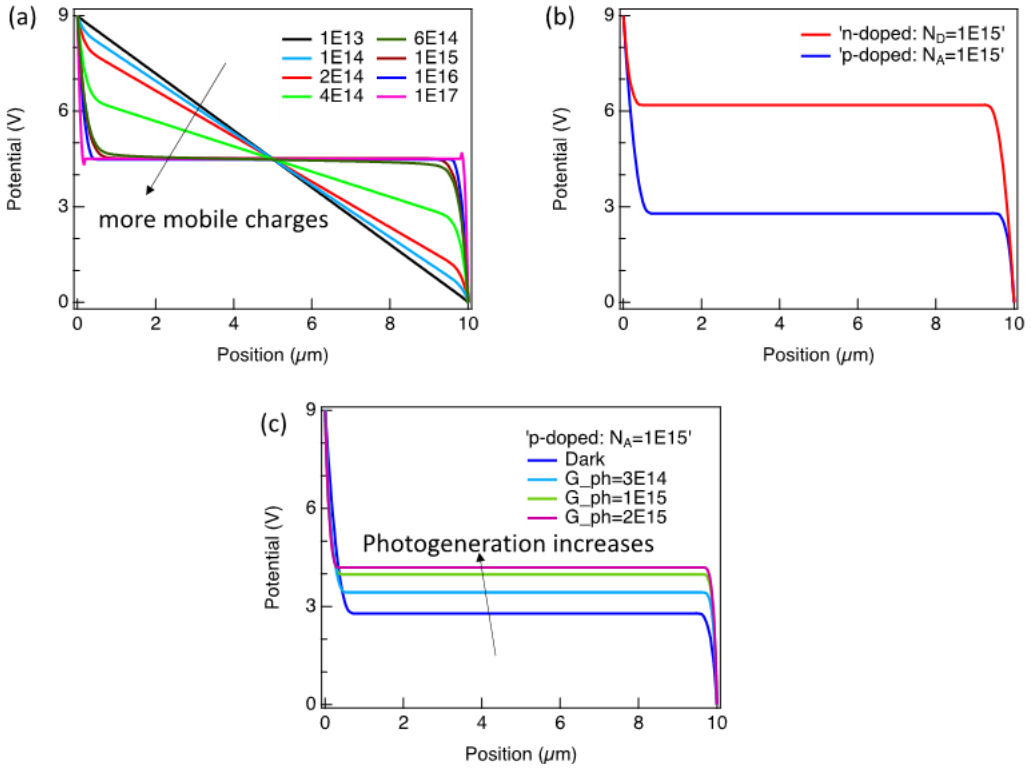

Figure S4. Drift-diffusion simulated potential profiles at electronic equilibrium, i.e. within the first scan during the charging process. (a) equal electron and hole density (n = p) with varying mobile charge density (in the unit of cm^{-3}). (b) asymmetric potential drop as predicted for n-doped (red) and p-doped (blue) semiconductor. (c) a p-doped semiconductor (N_A = 1E15 cm^{-3}) with varying photogenerated carrier density.

The potential distribution at electronic equilibrium greatly depends on the background mobile charge density. These figures explain the origin of potential distribution difference between n=1 and ~<n>=4 films to be that n=1 film is more intrinsic (n, p, ~ 2E14 cm^{-3}) whereas the ~<n>=4 film is self p-doped (N_A = 1E15 cm^{-3}). These simulation results further explain the potential evolution under illumination to be a result of photogenerated carriers in help screening the external electric field.

2.5 Proposed ion charging/discharging mechanism

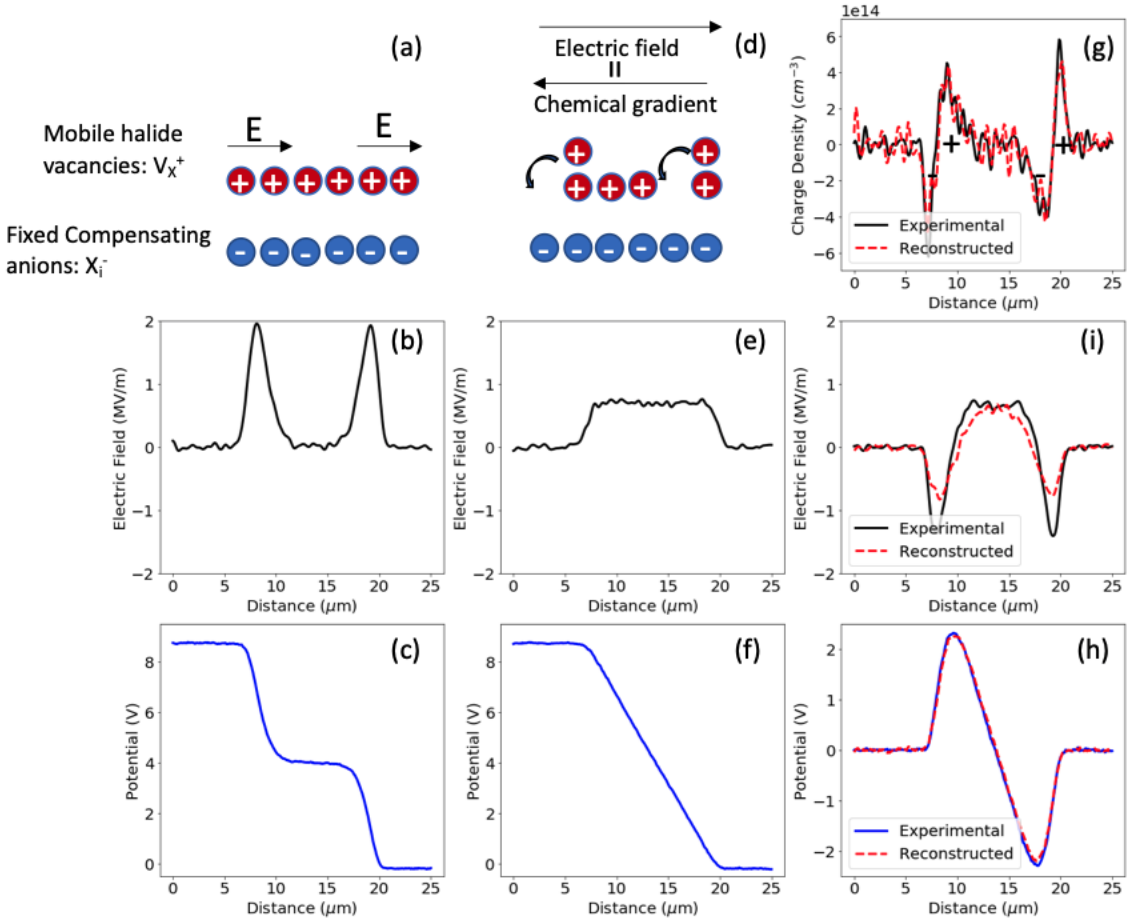

Figure S5. The proposed ion charging mechanism (a), electric field (b), and potential (c) profiles at electronic equilibrium (1st column); the proposed ion motion equilibrium with the field and chemical gradients (d), electric field (e), and potential (f) at the overall steady state (2nd column), i.e. long time after charging; the ionic charge density (g), electric field (i), and potential (h) at the ionic equilibrium (3rd column), where the experimental traces (solid) are measured immediately after removing the bias and the reconstructed traces (dashed) are calculated from subtracting the short time from the long time experimental potentials.

The charging process represent two responses (electronic/ionic) occurring on different timescales. In chronological order: (1) the bias is applied, at times faster than we can resolve the potential drop should be linear (not shown); (2) the electronic carriers respond, leading to the early time potential and field profiles shown in the experimental traces in the left column of **Figure S5** (**Figure S5 (c) & (b)**), this is the potential trace we measure immediately (a few sec) after poling. (If the bias is quickly removed at this point, very little ionic build up is observed). As the figure show the electric field is substantially screened – a high electric field is only located near the two contacts whereas the electric field in the center is near zero. Therefore, only ions at those high-field edges will drift to the right (**Figure S5 (a)**), but those near the center

remain at their equilibrium location (here we draw only for the BA_2PbI_4 (n=1) case, where the mobile ionic species should only be the positively charged halide vacancies) (3) After longer times (hundreds of seconds) the ionic charge carriers in the high field regions have migrated under the net field, coming to equilibrium with the field and the chemical concentration gradient (**Figure S5 (d)**). Eventually, the ions stop moving further along the electric field, possibly indicating a limiting reaction, either depletion of the ion density, or reaction between the high densities of the ions and electronic carriers. The exact chemical mechanism of this reaction will likely require in depth study. The resulting experimental long-time/equilibrium electric potential and field profiles are shown in the middle column of the figure (**Figure S5 (f) & (e)**). (4) Finally, after the bias is removed, the electronic carriers rapidly return, leaving a snapshot of the long time local ionic charge distribution behind as shown in the third column, experimental **Figure S5 (g)-(h)**, [solid trace, immediately after removing the long-time poling bias]. Consistent with this proposal, we can "reconstruct" the ionic-only potential and field by subtracting the short time from long time electric potentials (red dashed traces in **Figure S5 (g)-(h)**). The resulting traces agree remarkably well, as seen in **Figure S5 (g)**, implying that the equilibrium "linear" potential profile results from a superposition of the early time "electronic" profile and the longer time "ionic" profile. The resulting charge density distribution is also consistent with the scheme we proposed for the charging process (**Figure S5 (g) vs. (d)**).

2.6 Potential profiles for samples with different poling time.

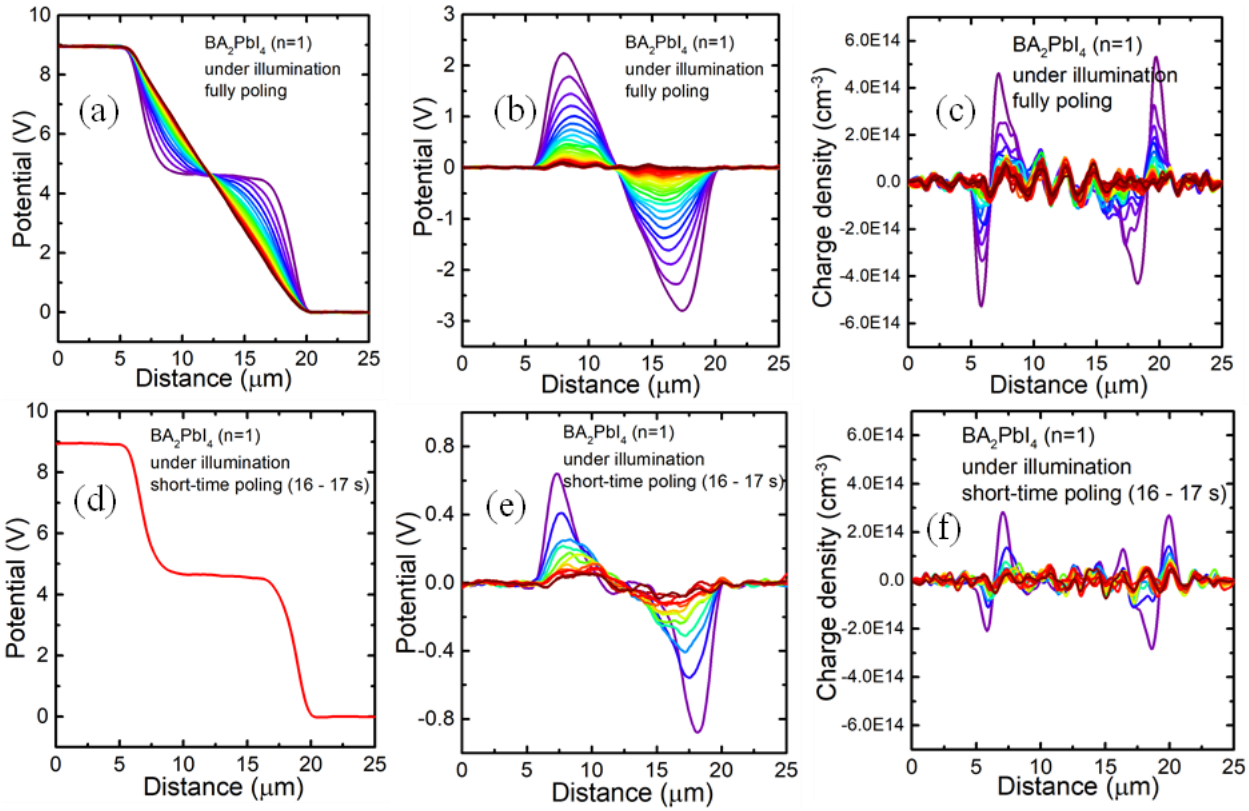

Figure S6. The charging, discharging potential profiles and charge carrier densities of BA_2PbI_4 (*n*=1) based devices under illumination with (a-c) ~ 300 seconds' full poling, and (d-f) 16 – 17 seconds' incomplete poling. All of the potential profiles have been shifted so that the grounded electrode is fixed at zero (essentially removing the small CPD between the tip and the gold electrode).

2.7 Potential, Field, and Charge Density from Experimental SKPM Data via Poisson Equation

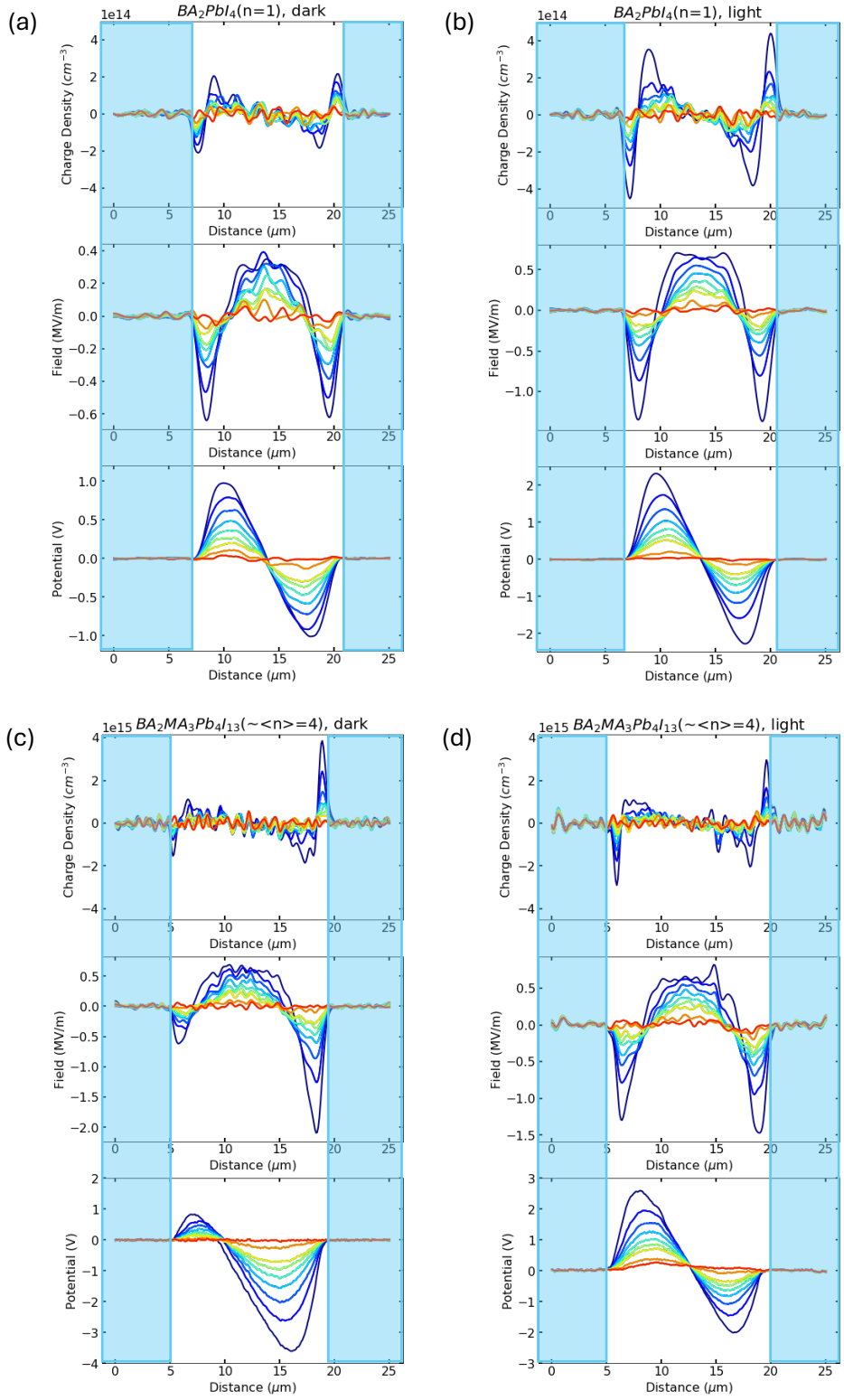

Figure S7. Calculated electric field and charge density distribution during the discharging process for BA_2PbI_4 (n=1) perovskite films (a) in the dark and (b) under illumination, and $BA_2MA_3Pb_4I_{13}$ (~<n>=4) perovskite films (c) in the dark and (d) under illumination. The lines evolve in time from the dark purple to the dark red line. The light yellow overlays indicate the position of the gold electrodes. The wiggles in the middle junction of electric field and charge density plots are artifacts due to the differentiation process. All of the potential profiles have been shifted so that the grounded electrode is fixed at zero (essentially removing the small CPD between the tip and the gold electrode).

2.8 The light intensity dependent ion migration behavior for BA_2PbI_4 (n=1) perovskite samples.

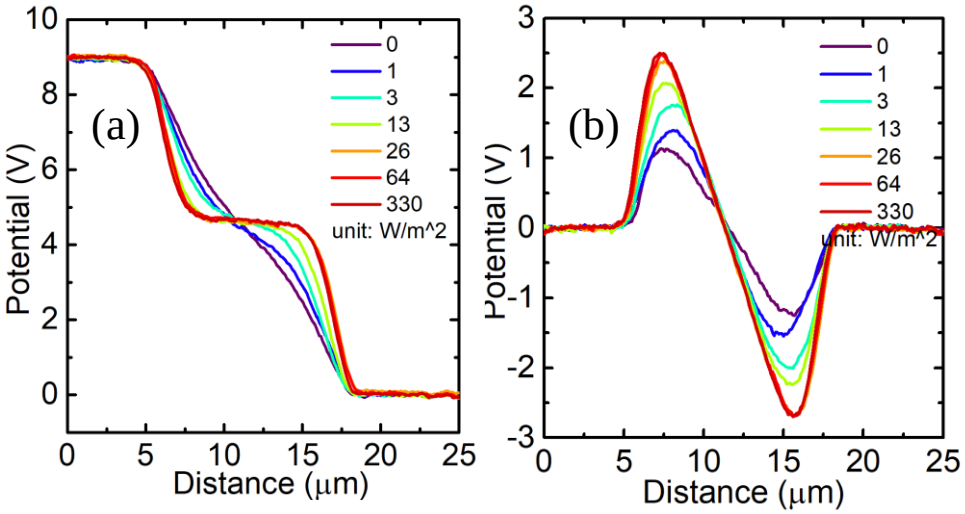

Figure S8 Potential profiles, evolving from dark purple lines to bright red lines as light illumination intensity increases, for BA_2PbI_4 (n=1) based devices during the (a) charging and (b) discharging process under light illumination. All of the potential profiles have been shifted so that the grounded electrode is fixed at zero (essentially removing the small CPD between the tip and the gold electrode).

2.9 Potential profiles/decay profiles of devices using polystyrene/SiOx or PMMA (varied thickness)/SiOx as the insulator.

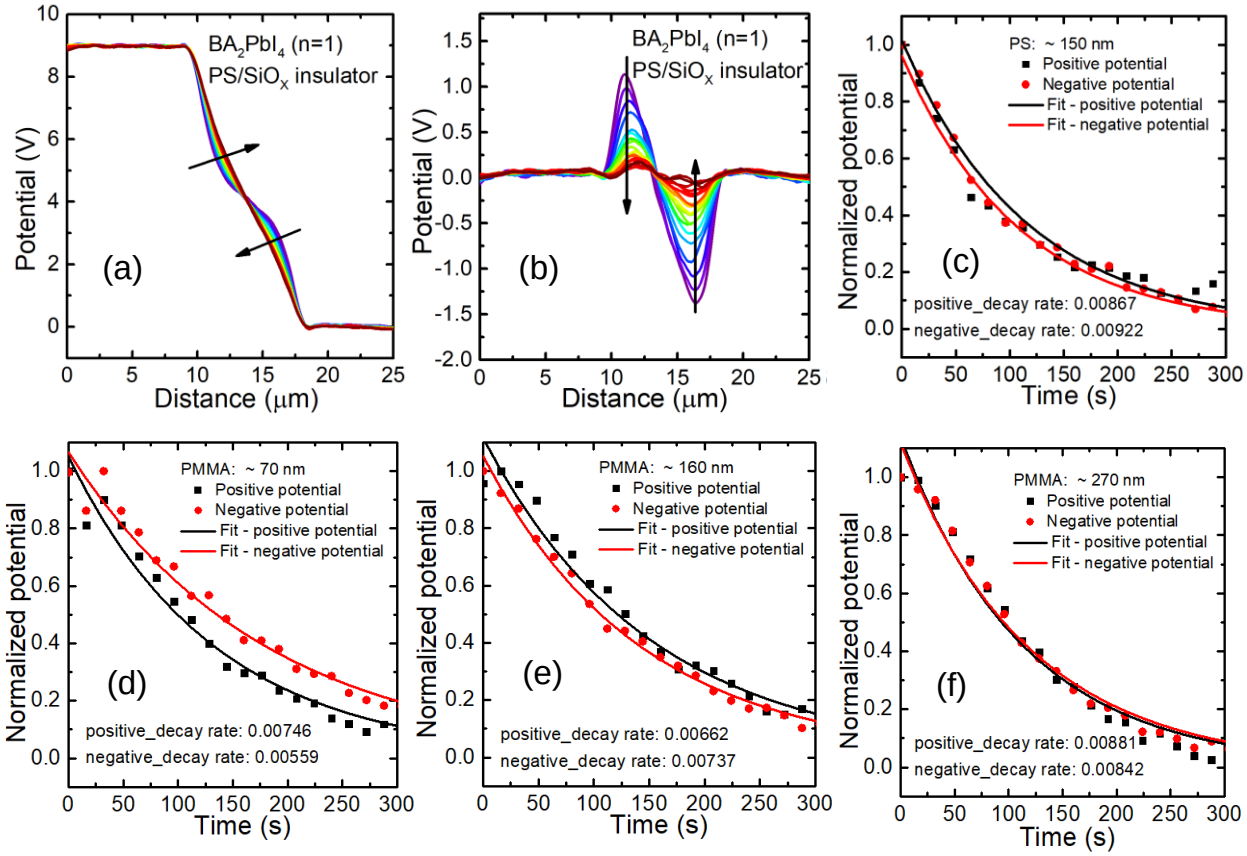

Figure S9. The (a) charging and (b) discharging potential profiles of BA_2PbI_4 (n=1) based device that uses polystyrene/SiOx as the insulating layer. A comparison between the decay profiles/rates that (c) ~ 150 nm – thick polystyrene, (d) ~ 70 nm – thick PMMA, (e) ~ 160 nm - thick PMMA, and (f) ~ 270 nm – thick PMMA, together with ~ 65 nm – thick SiOx as the insulating layer. All of the potential profiles have been shifted so that the grounded electrode is fixed at zero (essentially removing the small CPD between the tip and the gold electrode).

2.10 Decay curves of BA_2PbI_4 (n=1) perovskite samples measured at different temperatures.

(a) In the dark; negative potentials

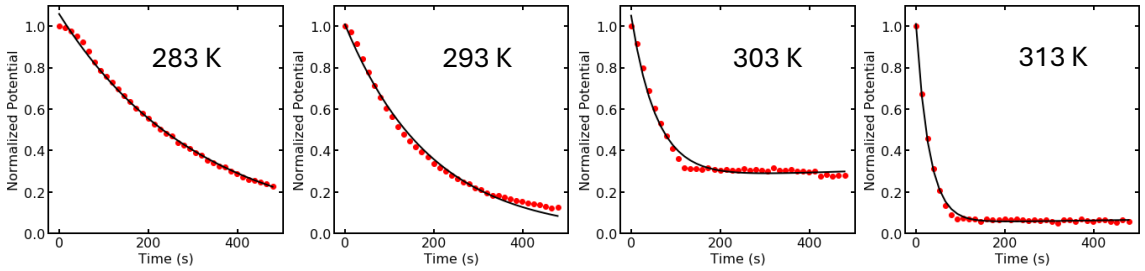

(b) In the dark; positive potentials

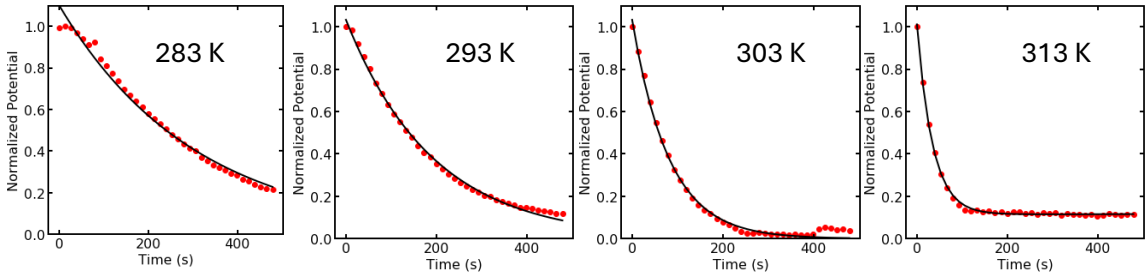

(c) Under light; negative potentials

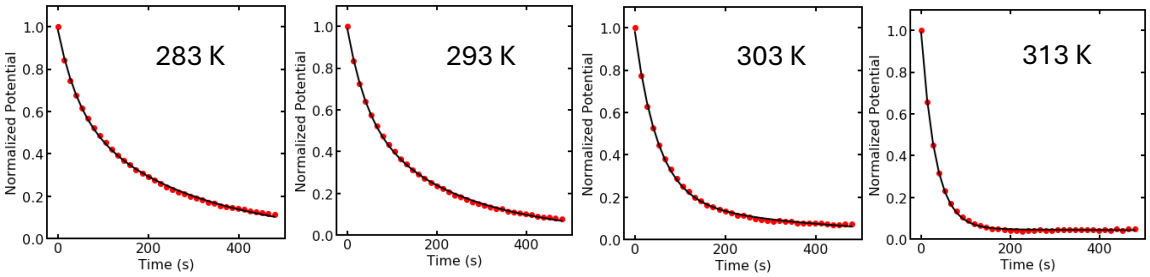

(d) Under light; positive potentials

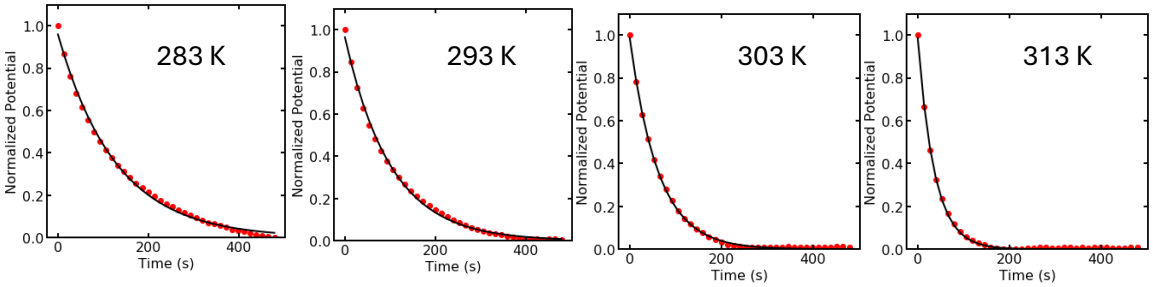

Figure S10. Decay curves and the corresponding fitted curves of (a, c) negative potentials and (b, d) positive potentials for BA_2PbI_4 (n=1) perovskite samples measured at different temperatures, in the dark and under light illumination. The data are obtained by extracting both the negative and positive potential peaks at each time step and then are fit with exponential functions to determine decay rates.

2.11 Decay curves of $BA_2MA_3Pb_4I_{13}$ (~<*n*>=4) perovskite samples measured at different temperatures.

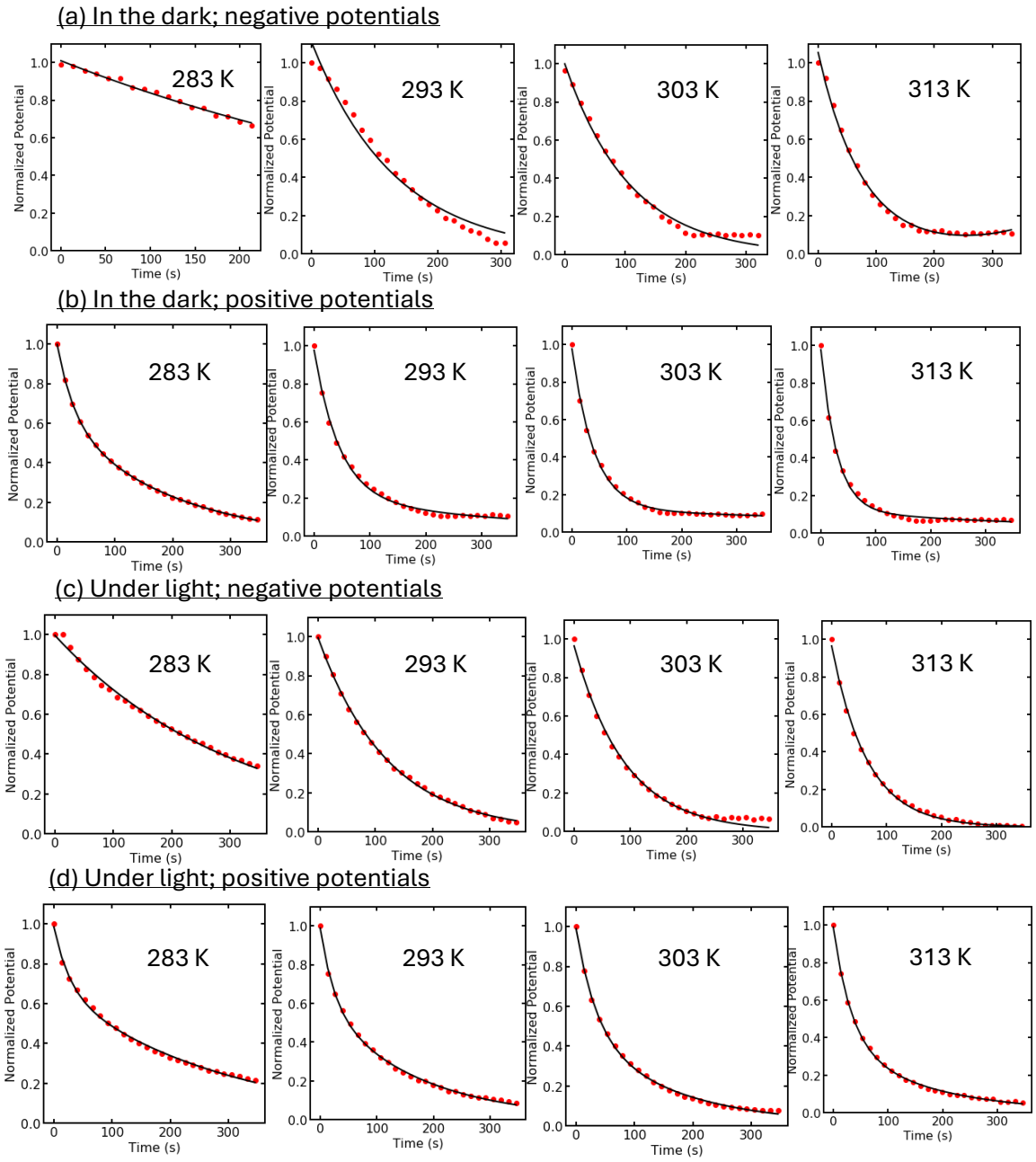

Figure S11. Decay curves and the corresponding fitted curves of (a, c) negative potentials and (b, d) positive potentials for $BA_2MA_3Pb_4I_{13}$ (~<*n*>=4) perovskite samples measured at different temperatures, in the dark and under light illumination. The data are obtained by extracting both the negative and positive potential peaks at each time step and then are fit with exponential functions to determine decay rates.

2.12 Comparison of activation energies for BA_2PbI_4 (n=1) and $BA_2MA_3Pb_4I_{13}$ (~<n>=4) perovskite films.

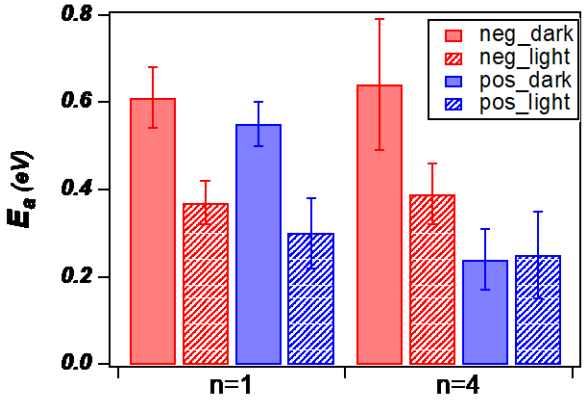

Figure S12. A graphical comparison of the activation energies obtained for BA_2PbI_4 (n=1) and $BA_2MA_3Pb_4I_{13}$ (~<n>=4) perovskite films both in the dark and under illumination with the associated error bars.

A3. References

(1) Tsai, H.; Nie, W.; Blancon, J. C.; Stoumpos, C. C.; Asadpour, R.; Harutyunyan, B.; Neukirch, A. J.; Verduzco, R.; Crochet, J. J.; Tretiak, S.; Pedesseau, L.; Even, J.; Alam, M. A.; Gupta, G.; Lou, J.; Ajayan, P. M.; Bedzyk, M. J.; Kanatzidis, M. G., High-Efficiency Two-Dimensional Ruddlesden-Popper Perovskite Solar Cells. *Nature* **2016**, 536, 312-316.

(2) Soe, C. M. M.; Nagabhushana, G. P.; Shivaramaiah, R.; Tsai, H.; Nie, W.; Blancon, J.-C.; Melkonyan, F.; Cao, D. H.; Traoré, B.; Pedesseau, L.; Kepenekian, M.; Katan, C.; Even, J.; Marks, T. J.; Navrotsky, A.; Mohite, A. D.; Stoumpos, C. C.; Kanatzidis, M. G., Structural and Thermodynamic Limits of Layer Thickness in 2d Halide Perovskites. *Proc. Natl. Acad. Sci.* **2019**, 116, 58-66.

(3) Hong, X.; Ishihara, T.; Nurmikko, A. V., Dielectric Confinement Effect on Excitons in PbI_4-Based Layered Semiconductors. *Phys. Rev. B* **1992**, 45, 6961-6964.

(4) Stoumpos, C. C.; Cao, D. H.; Clark, D. J.; Young, J.; Rondinelli, J. M.; Jang, J. I.; Hupp, J. T.; Kanatzidis, M. G., Ruddlesden–Popper Hybrid Lead Iodide Perovskite 2D Homologous Semiconductors. *Chem. Mater.* **2016**, 28, 2852-2867.

Appendix B: Supporting Information for Chapter 3

B1. Experimental Methods

1.1 Sample preparation

A 1.2 M $Cs_{0.22}FA_{0.78}Pb(I_{0.85}Br_{0.15})_3$ solution was prepared by mixing the correct molar ratio of PbI_2 (TCI, 99.99%, for perovskite precursor), $PbBr_2$ (Alfa Aesar, 99.999%, ultra dry), Formamidinium iodide (Great Cell Solar, >99.99%), CsI (Alfa Aesar, 99.999%) and a 3 mol% relative to the Pb content equivalent of $PbCl_2$ (TCI, >99.0%, for perovskite precursor) and Methylammonium chloride (Xi'an Polymer Light Technology Corp., >99.5%) in a 3:1 solvent ratio of N,N-Dimethylformamide (DMF) and Dimethyl sulfoxide (DMSO). Glass and indium tin oxide (ITO) coated glass substrates 1.5 cm^2 in size were cleaned by sequential sonication in water containing ~2% Micro-90 detergent, DI water, acetone, and isopropanol for 10 minutes each. The substrates were ozone-cleaned for 23 minutes prior to spincoating. The perovskite solution was filtered through a 0.2 μm PTFE membrane filter. Approximately 60 μL of the perovskite solution was deposited on top of the substrate and spincoated at 5000 rpm for 50 s with an acceleration of 2500 rpm/s. After 25-30 s, 200 μL of a Methyl acetate antisolvent was deposited on the spinning substrate. The thin film was then annealed for 30 min at 100 °C on a hot plate.

A 1.2 M $Cs_{0.17}FA_{0.83}Pb(I_{0.75}Br_{0.25})_3$ solution was prepared by mixing the correct molar ratio of PbI_2 (TCI, 99.99%, for perovskite precursor), $PbBr_2$ (Alfa Aesar, 99.999%, ultra dry), Formamidinium iodide (Great Cell Solar, >99.99%), CsI (Alfa Aesar, 99.999) in a 4:1 solvent ratio of DMF and DMSO. The same cleaning and solution filtration was carried out as described above. Using dynamic spincoating, the substrate was allowed to spin at 1000 rpm for 10 s with an acceleration of 200 rpms/s and around 80 μL of the perovskite solution was deposited on top of the substrate after 3 s of spinning. Next, the spincoater ramped up to 5000 rpm for 35 s with an acceleration of 800 rpm/s and 330 μL of an anisole antisolvent was deposited at 5 s remaining. The thin film was then annealed for 45 min at 100 °C on a hot plate.

For hyperspectral measurements, perovskite samples deposited on glass were encapsulated in a nitrogen glovebox. The encapsulation method uses a second glass slide to sandwich the perovskite thin film between the substrate and the other glass slide. UV curable BLUFIXX epoxy is used along the edges and corners of the glass sandwich to seal them together in the nitrogen atmosphere.

1.2 Surface passivation with APTMS

APTMS passivation of the perovskite films was performed at room temperature and ambient conditions in a vacuum oven for 5 mins. A volume of 500 μL of APTMS was placed in a 4 mL vial with the perovskite film placed face up near the vial. The vial and film were covered with a 500 mL glass jar inside of the chamber and was pumped down to -26 In. of Hg relative to atmospheric pressure. Schematics for the silane deposition can be found in Ref. 1.[1]

1.3 Time-Resolved Photoluminescence (TRPL)

TRPL was measured using a PicoQuant Picoharp 300 TCSPC system equipped with a 640 nm pulsed diode laser with a high average power of 30 mW. The laser was pulsed at repetition rates of 500 kHz and 83 kHz for the control and APTMS passivated films, respectively, in order to capture the full decay trace and prevent photon pile-up at the detector. The excitation fluence used for both samples was ~3.4 nJ/cm^2. The PL emission was passed through a 700 nm long-pass filter before reaching the detector. The PL data was fitted using a stretched exponential function with the characteristic lifetime (τ_C) and β factor used as fitting parameters, as described in Equation 1. For this measurement, the perovskite samples were deposited on glass and were measured in ambient conditions immediately after removal from a dry-nitrogen glovebox.

Equation 1.

$$< \tau > \ = \frac{\tau_C}{\beta} \Gamma \left(\frac{1}{\beta} \right)$$

A summary of the fitted results in Table 1 show an ten-fold enhancement in the lifetime after APTMS passivation as well as an increase in the β factor – which suggests a reduction in the distribution of relaxation rates.

Table S1. Stretched exponential fitting parameters for $Cs_{0.22}FA_{0.78}Pb(I_{0.85}Br_{0.15})_3$ control and APTMS-passivated samples

	Control	**APTMS-passivated**
β factor	0.598	0.832
τ_C (ns)	79.90	817.56
<τ> (ns)	120.78	1015.60

1.4 Poling-based scanning Kelvin probe microscopy

Scanning Kelvin probe microscopy (SKPM) is a technique used to the contact potential difference (CPD) between the atomic force microscopy (AFM) tip and the sample. The CPD is determined by the difference between the work function of the tip and the sample ($V_{CPD} = -(\Phi_{tip} - \Phi_{sample})/e$).[2] Thus, electrical changes that occur in the sample to shift the work function of the sample can be understood through the CPD. All measurements were performed at room temperature, in the dark, and in a nitrogen flow cell. The SKPM measurements were made using an Asylum Research MFP-3D (Oxford Instruments) atomic force microscope mounted on an inverted Nikon Eclipse microscope and a customized piezo-stage. Cr/Pt-coated silicon tips (MikroMasch, 325 kHz, 40 N/m) were used to probe the CPD. The SKPM measurements were made using the conventional amplitude-modulated (AM) mode with the standard lift-based method.

For this experiment, the SKPM measurement technique was modified to include an extra step to pole mobile charges towards the surface. First, the topography of a line is measured during a single-pass. Second, the cantilever lifts up to a set lift height, the AFM head is used to apply a set

DC bias to the tip while the ITO substrate is grounded, and a double-pass is performed across the line. Applying this bias to the tip creates a vertical electric field to pole mobile charges to the surface and prevented charge injection into the film by having the atmosphere act as an insulator between the tip and sample. Next, the DC bias to create the electric field is removed and the system transitions into the CPD measurement. Finally, an AM mode SKPM single-pass is performed to measure the CPD after poling. This process occurs for each individual line collected in the images.

1.5 SKPM image processing

Due to applying relatively large biases to the tip during the SKPM measurements and length of the measurement, the AFM tip is prone to both picking up contaminant or dulling which may lead to drift in the measured CPD. These errors are corrected by collecting a quick, low resolution CPD image with no applied bias to the tip in a region 30 μm away from the poled measurement area, as shown in **Figure S3**. This is performed prior to every image. The average CPD from the low resolution image is then subtracted from the following CPD image measured with an applied bias. Small line-to-line deviations that result in "streaky" images are also corrected for by using detrend function from the python scipy library to subtract a linear least-squares fit from the data at each line. Finally, the average CPD prior to detrending is added back to the image. These corrections allow for high quality images while retaining the meaning of the data even as the state of the tip changes throughout the measurements.

We create the binary mask to separate out domain centers from domain interfaces by first aligning the stack of image based on the topography. Next, we manually create a custom mask based on the topography to identify the domain interfaces. Using this mask, we extract the coordinates of the domain interfaces and use a pairwise distance function built in to SciKit Learn and calculate the average CPD with respect to distance from the nearest domain interface pixel.

1.6 Hyperspectral microscopy

Hyperspectral measurements were made using a Photon etc. IMA upright microscope fitted with a transmitted darkfield condenser and a 60X objective (Nikon Plan RT, NA 0.7, CC 0-1.2). Widefield, diffraction limited imaging is capable of being captured at a spectral range of 400 to 1000 nm with a lateral resolution of up to ~350 nm using a ThorLabs 1501M-USB 1.4 Megapixel cooled charged-coupled device (CCD) camera. The perovskite samples were deposited on glass and were excited with a 532 nm, 3W laser at a power density of ~600 mW/cm^2. A tunable Bragg filter is used by the hyperspectral microscope to image sample emission at specific wavelengths to generate a "Hyper Cube", which contains spectral information at each pixel. Hyperspectral images were collected for $Cs_{0.22}FA_{0.78}Pb(I_{0.85}Br_{0.15})_3$ control and APTMS passivated samples on glass that were encapsulated in a nitrogen glovebox with a spectral step size of 2 nm and integration time of 1.5 s per wavelength.

1.7 X-ray Diffraction

The X-ray diffraction measurements of $Cs_{0.22}FA_{0.78}Pb(I_{0.85}Br_{0.15})_3$ and $Cs_{0.17}FA_{0.83}Pb(I_{0.75}Br_{0.25})_3$ perovskite thin films on glass substrates with and without APTMS surface passivation were

conducted using a Bruker D8 Discover with a Pilatus 100 K large-area 2D detector (Cu Kα radiation at 50,000 mW). The perovskite samples were measured in ambient conditions immediately after being removed from a dry-nitrogen glovebox.

1.8 UV-Vis Extinction

UV-Vis extinction spectra of the $Cs_{0.22}FA_{0.78}Pb(I_{0.85}Br_{0.15})_3$ and $Cs_{0.17}FA_{0.83}Pb(I_{0.75}Br_{0.25})_3$ perovskite thin films on glass substrates with and without APTMS surface passivation were measured on an Agilent 8453 UV-Vis Spectrometer in a range of 400 – 800 nm and an integration time of 0.5 s. The perovskite samples were measured in ambient conditions immediately after being removed from a dry-nitrogen glovebox.

B2. Supplementary figures and discussions

2.1 X-ray diffraction patterns

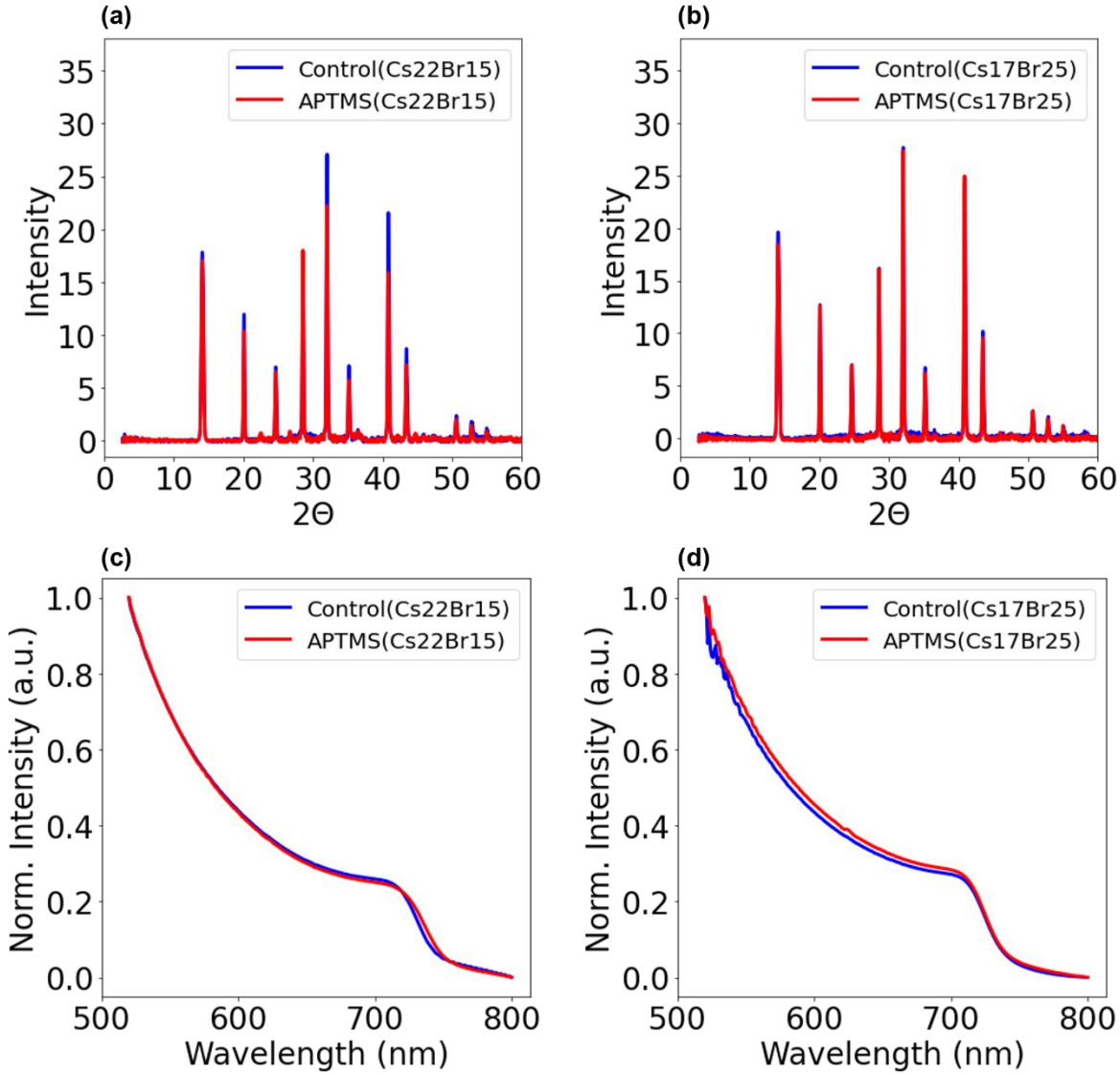

Figure S1. X-ray diffraction for (a) $Cs_{0.22}FA_{0.78}Pb(I_{0.85}Br_{0.15})_3$ and (b) $Cs_{0.17}FA_{0.83}Pb(I_{0.75}Br_{0.25})_3$ control and APTMS passivated films. UV-vis extinction spectra for (c) $Cs_{0.22}FA_{0.78}Pb(I_{0.85}Br_{0.15})_3$ and (d) $Cs_{0.17}FA_{0.83}Pb(I_{0.75}Br_{0.25})_3$ control and APTMS passivated films.

2.2 SKPM energy band diagram

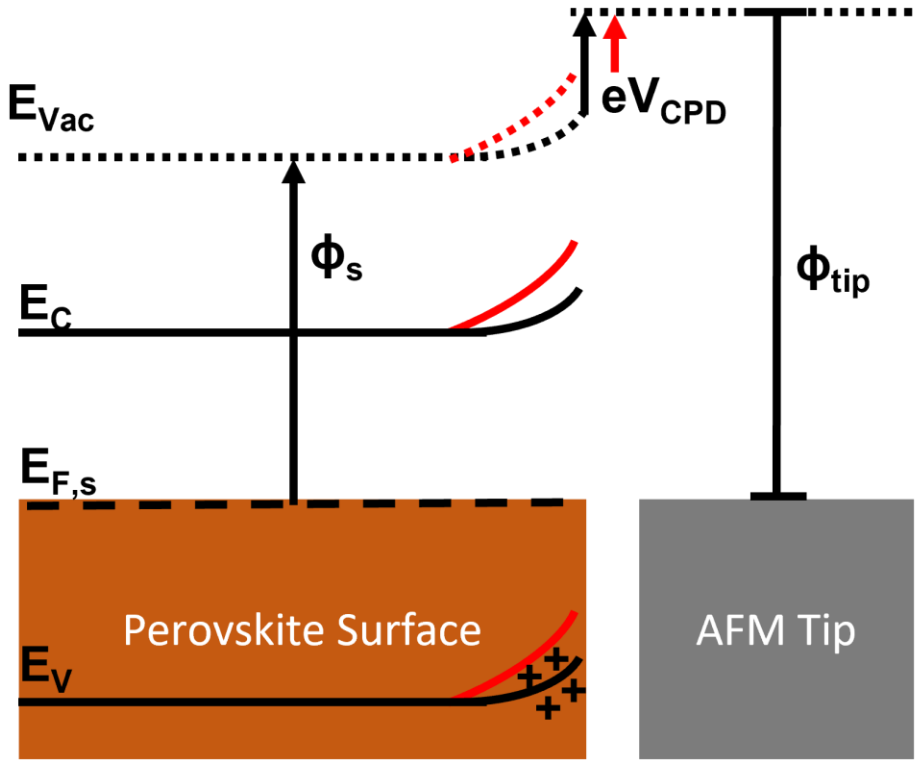

Figure S2. Illustration of the energy band alignment between the perovskite surface and AFM tip. Shown in black is the energy alignment when the CPD is measured without an applied field and shown in red is the alignment when the CPD is measured under a negative tip bias – which poles positive charges (halide vacancies) to the surface and induces further bending of the bands.

2.3 SKPM potential drift correction

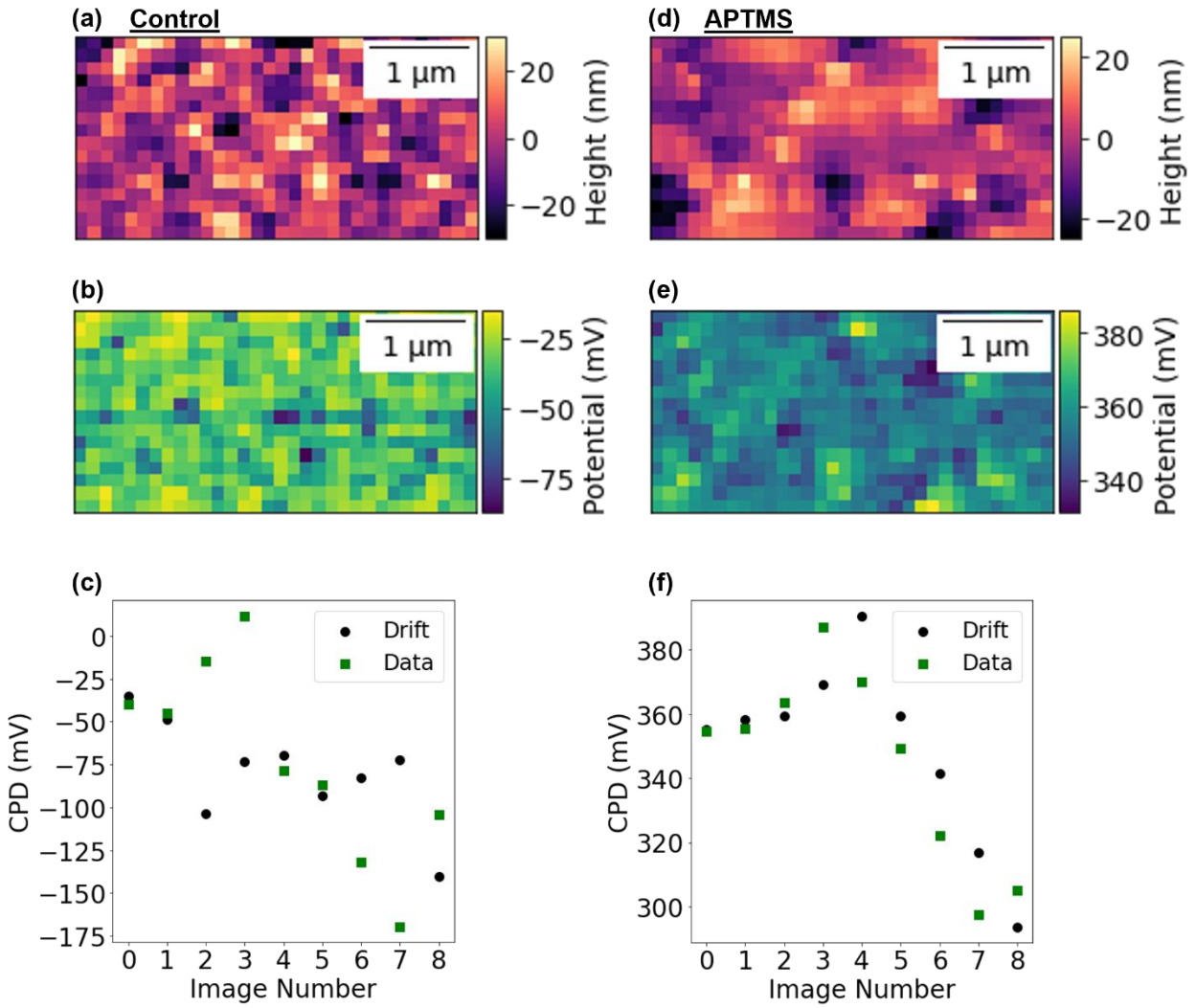

Figure S3. Low resolution (a, d) topography and (b, e) CPD of $Cs_{0.22}FA_{0.78}Pb(I_{0.85}Br_{0.15})_3$ control and APTMS passivated films, respectively, at a region 30 µm away from poling-based SKPM region. The measured CPD at this location is used to track and correct for drift in the measured CPD in our regions-of-interest. (c,f) Measured CPD of region used to track the drift in the control and APTMS passivated films, respectively, compared with the actual measured data shown for each collected image.

In **Figure S4**, we examine the perovskite CPD after completing poling in both the positive and negative direction. In the unpassivated sample, we see that the CPD remains shifted after poling, whereas the APTMS-passivated sample returns close to its pre-poling state. This result shows that the passivated film is more resilient to permanent changes at the surface induced by poling.

2.4 CPD pre- and post-poling

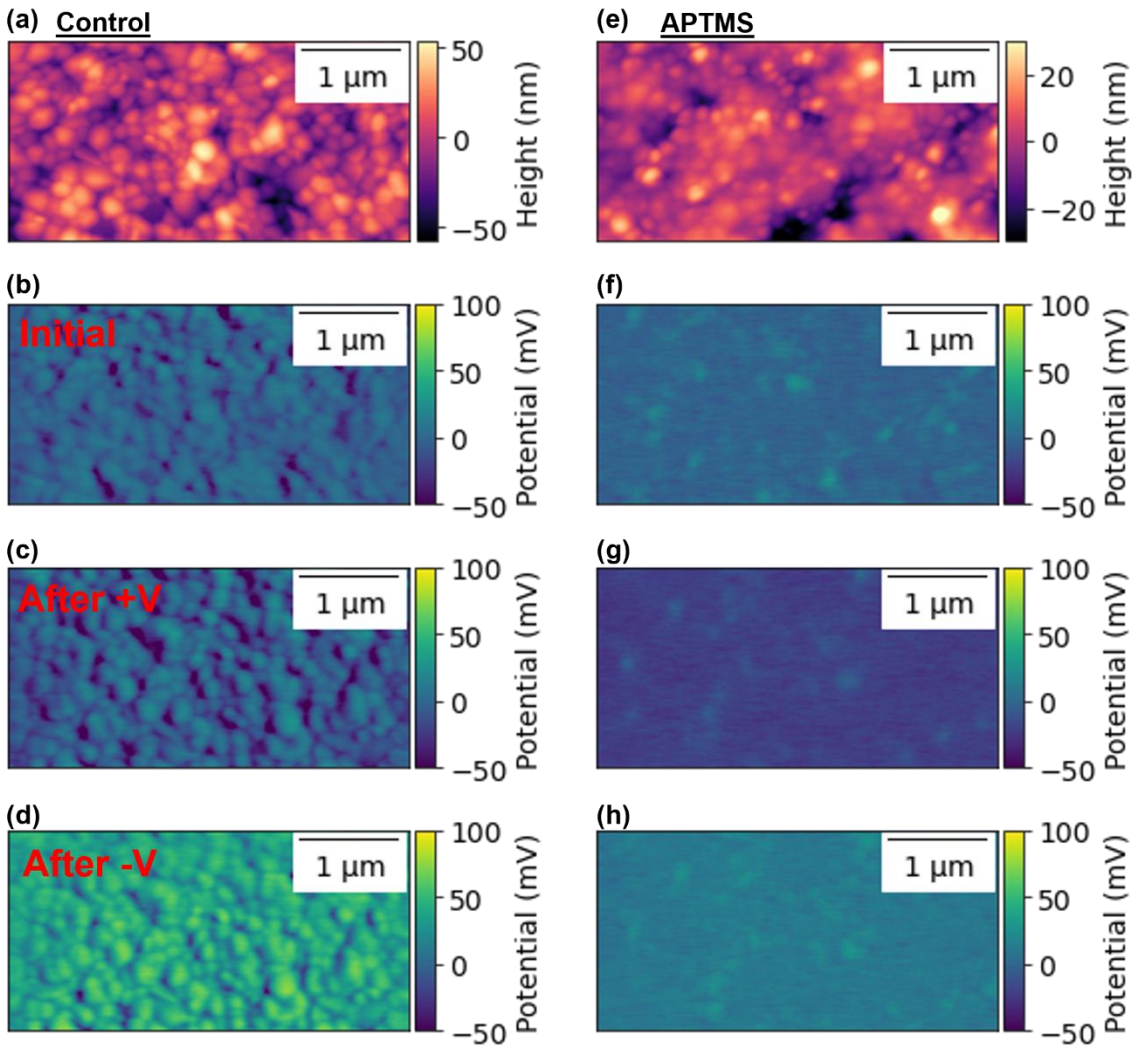

Figure S4. (a,e) Topography of the $Cs_{0.22}FA_{0.78}Pb(I_{0.85}Br_{0.15})_3$ control and APTMS-passivated films. (b,f) Baseline CPD of the control and passivated films measured at 0 V. (c,g) CPD of the control and passivated films measured at 0 V after sweeping the tip bias in the positive direction. (d,h) CPD of the control and passivated films measured at 0 V after sweeping the tip bias in the negative direction.

We show in **Figure S5** the same *local*-poling based SKPM measurement on a second perovskite composition with the composition $Cs_{0.17}FA_{0.83}Pb(I_{0.75}Br_{0.25})_3$. We observe similar changes in the average CPD and heterogeneity after APTMS passivation, but to a lesser extent. The decreased effect of APTMS here may be due to decreased ion motion in the perovskite formulation or varying degrees of passivation effectiveness on varying chemical compositions, but nonetheless shows the reproducibility of this measurement.

2.5 Poling experiment on alternative perovskite formulation

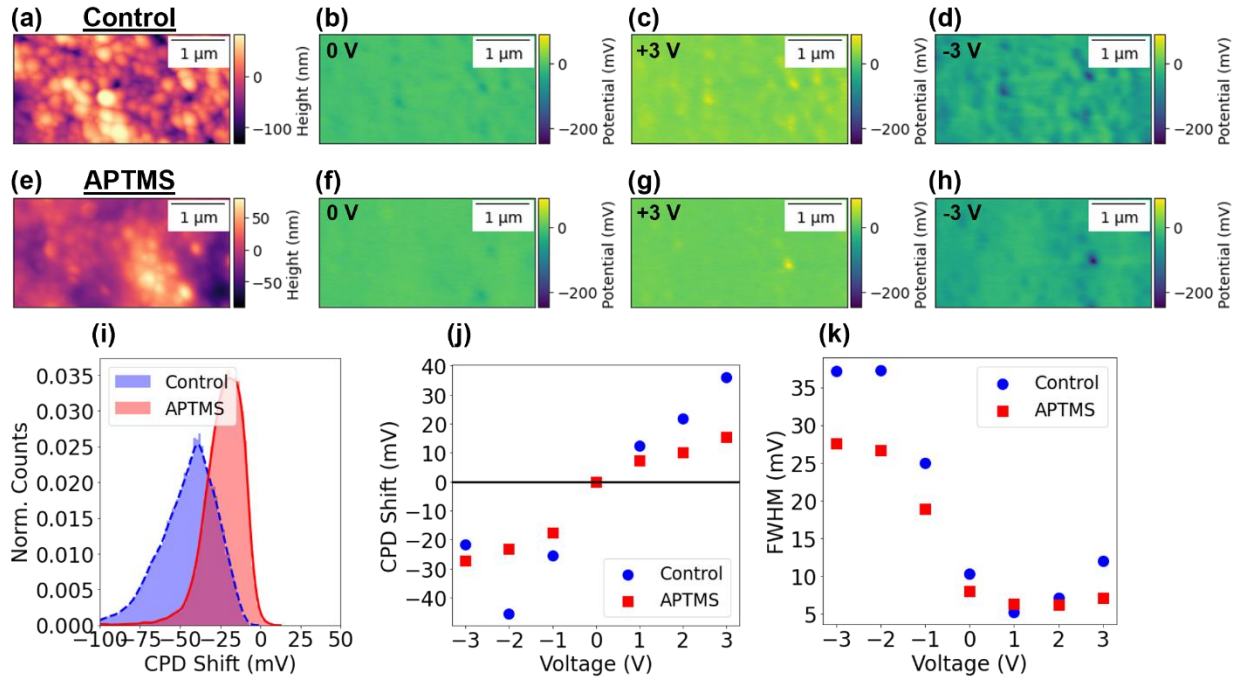

Figure S5. (a) Topography and (b-d) CPD of a $Cs_{0.17}FA_{0.83}Pb(I_{0.75}Br_{0.25})_3$ control film measured with applied tip biases of 0, +3, and -3 V. (e) Topography and (f-h) CPD of APTMS passivated film measured with applied tip biases of 0, +3, and -3 V. All CPD images are shown on the same color scale to show the differences between the two samples. (i) Probability density distribution of the shift in CPD relative to the baseline CPD for control and APTMS passivated films measured at -2 V. (j) CPD shift relative to the baseline CPD as a function of bias for control and APTMS passivated films. (k) FWHM as a function of applied tip for control and APTMS passivated films.

2.6 Probability density distributions of CPD shift

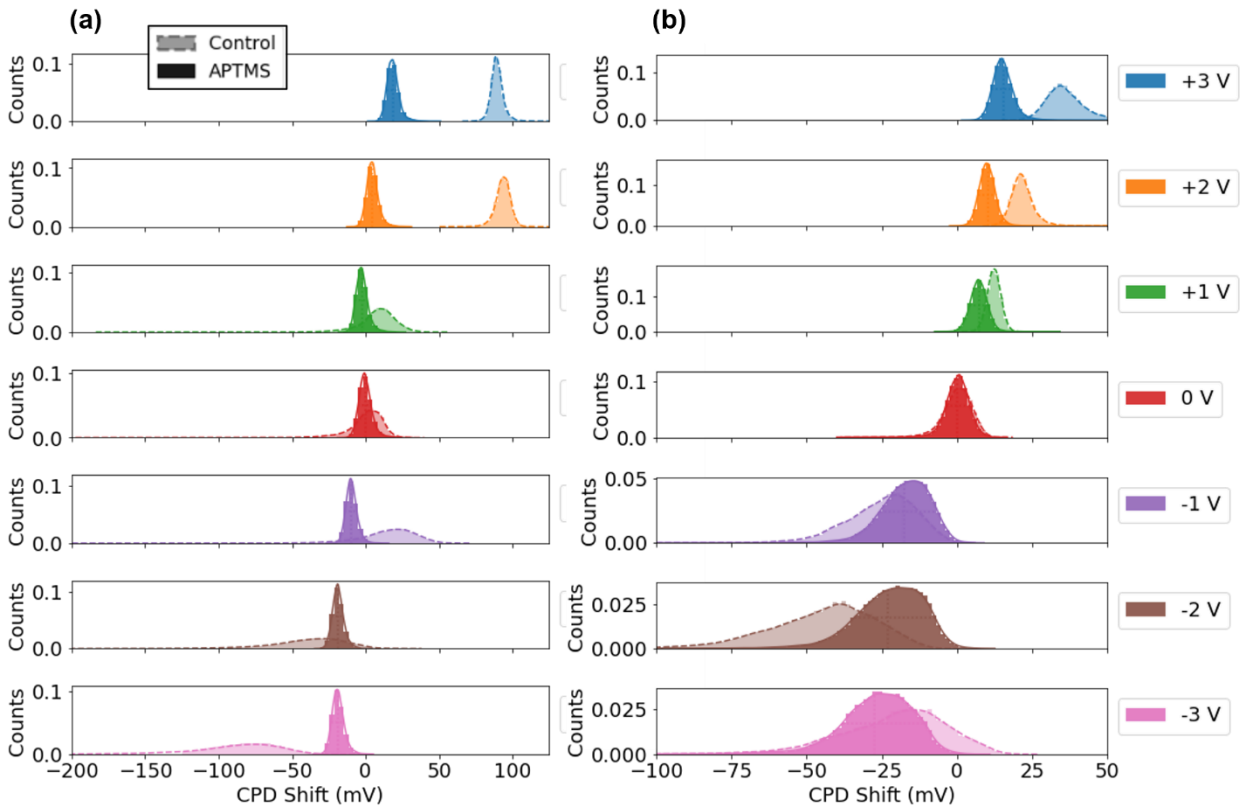

Figure S6. Overall probability density distributions for (a) $Cs_{0.22}FA_{0.78}Pb(I_{0.85}Br_{0.15})_3$ and (b) $Cs_{0.17}FA_{0.83}Pb(I_{0.75}Br_{0.25})_3$ control and APTMS passivate films as a function of applied tip bias.

2.7 CPD relative to distance from domain interface

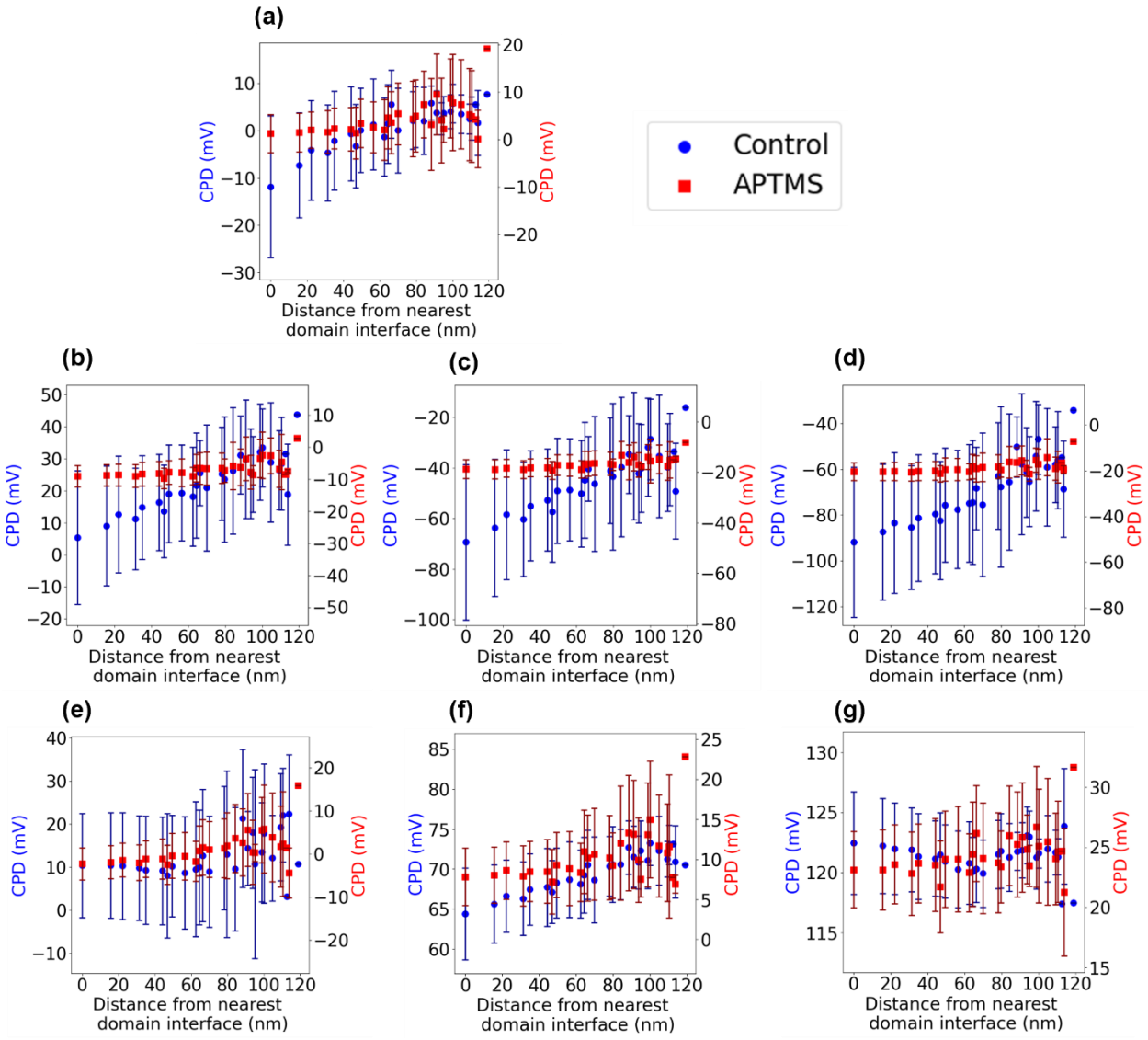

Figure S7: Measure CPD as a function of distance to the nearest domain interface for $Cs_{0.22}FA_{0.78}Pb(I_{0.85}Br_{0.15})_3$ control and APTMS passivated films at biases of (a) 0V, (b-d) -1 to -3 V, and (e-g) +1 to +3 V.

2.8 CPD image contrast relative to tip bias

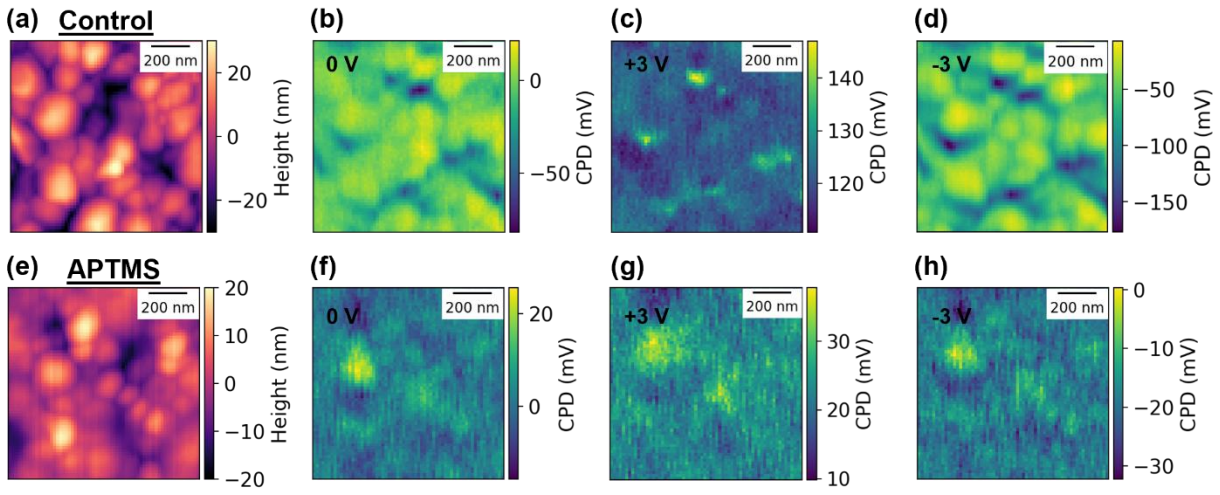

Figure S8: (a) Topography and (b-d) CPD of a $Cs_{0.22}FA_{0.78}Pb(I_{0.85}Br_{0.15})_3$ control film at 0, +3, and -3 V bias, respectively. (e) Topography and (f-h) CPD of an APTMS passivated film at 0, +3, and -3V bias, respectively.

We analyzed the measured CPD as a function of sample morphology by exploring the dependence of the CPD on the area of each domain. We used the same masks to separate out sample domain and domain interfaces to identify individual domains, as shown in **Figure S9a and c**, and calculate both the area and average CPD of each domain. We show the CPD as a function of domain area for $Cs_{0.22}FA_{0.78}Pb(I_{0.85}Br_{0.15})_3$ control and APTMS-passivated in **Figure S9b and d**. We do not see an obvious trend of CPD with domain area and we observe that the measured values at all area agree well with the average CPD of the scanned area.

2.9 CPD relative to domain size

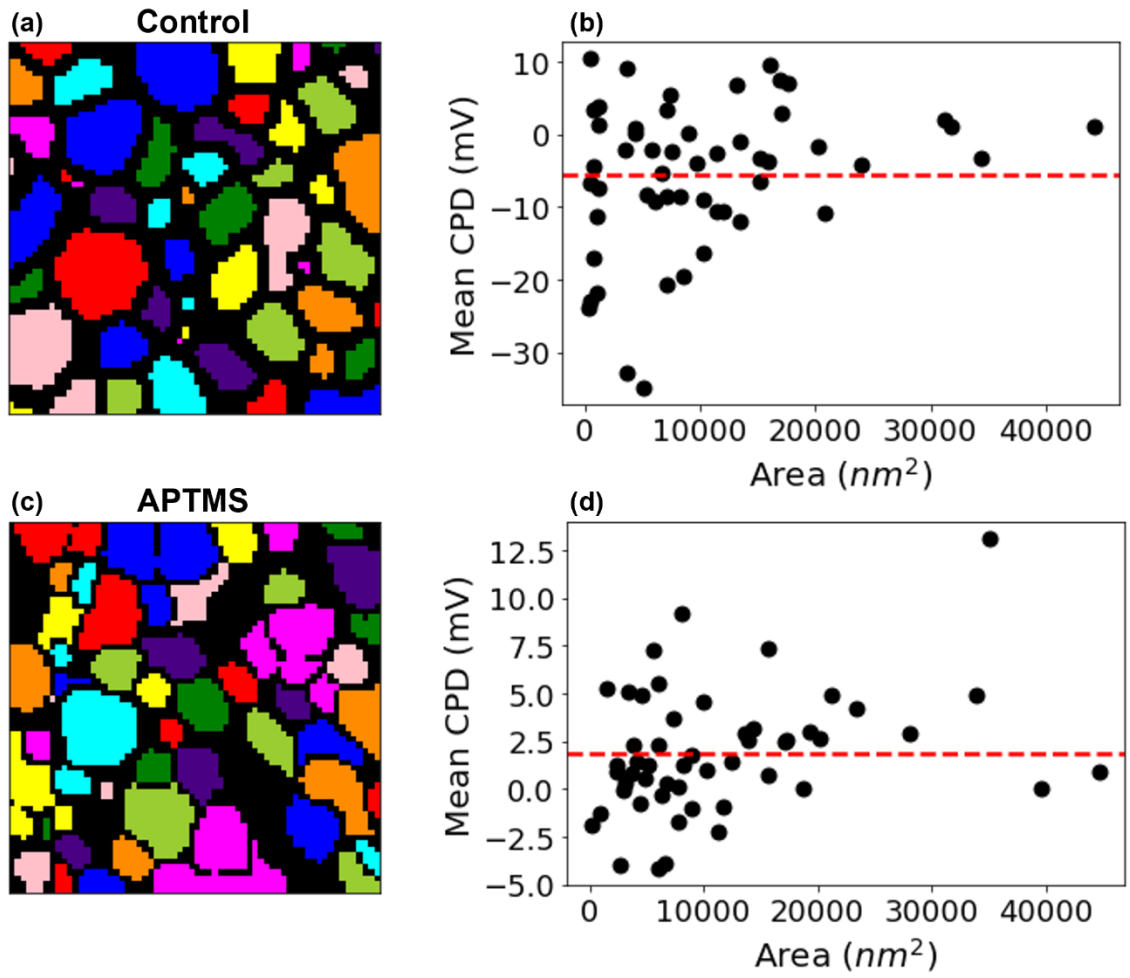

Figure S9: (a,c) Map of individually selected domains of $Cs_{0.22}FA_{0.78}Pb(I_{0.85}Br_{0.15})_3$ control and APTMS-passivated films. (b,d) Mean CPD as a function of domain area. The red, dashed line show the average CPD of the whole imaged area.

2.10 Hyperspectral PL intensity maps

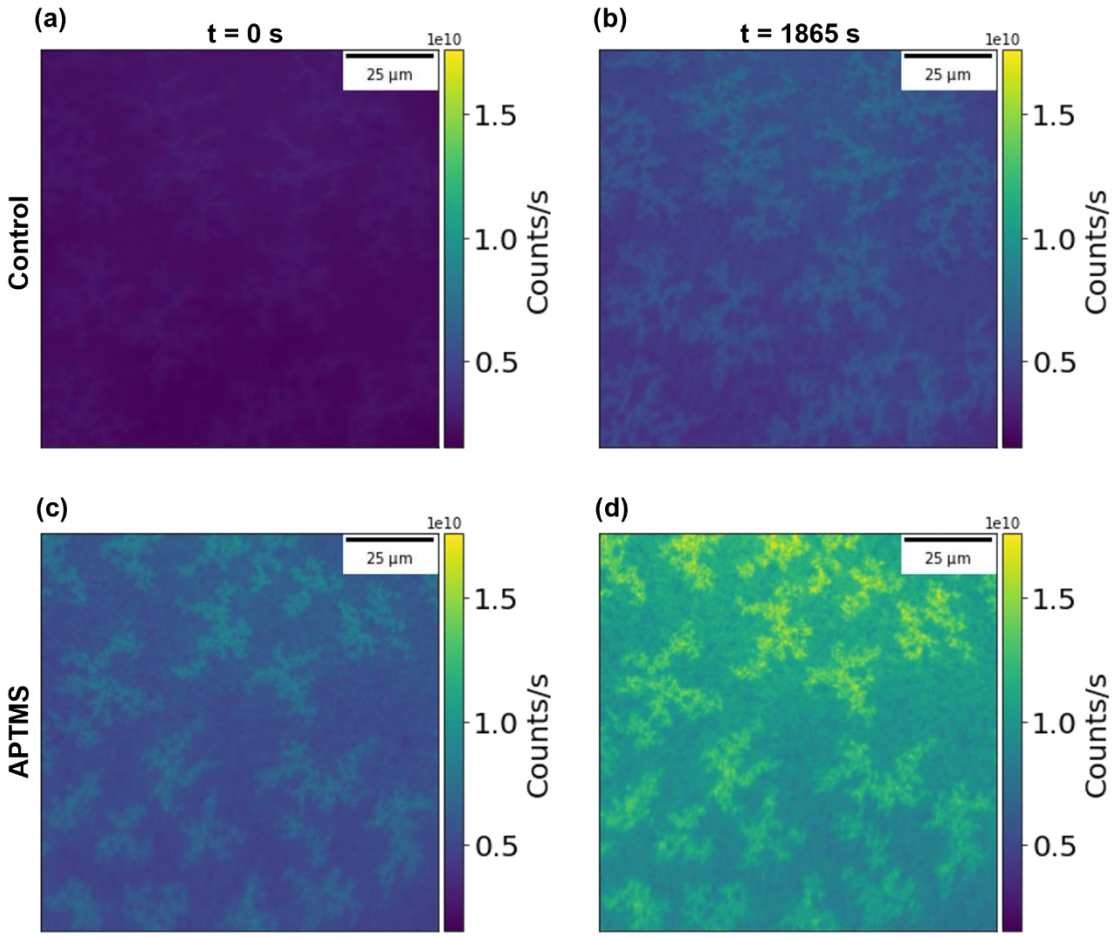

Figure S10. Overall PL intensity map of the $Cs_{0.22}FA_{0.78}Pb(I_{0.85}Br_{0.15})_3$ control film after photo-soaking times of (a) 0 s and (b) 1865 s. (c) Overall PL intensity map of the APTMS passivation film after photo-soaking times of (c) 0 s and (d) 1865 s.

2.11 Halide phase segregation analysis

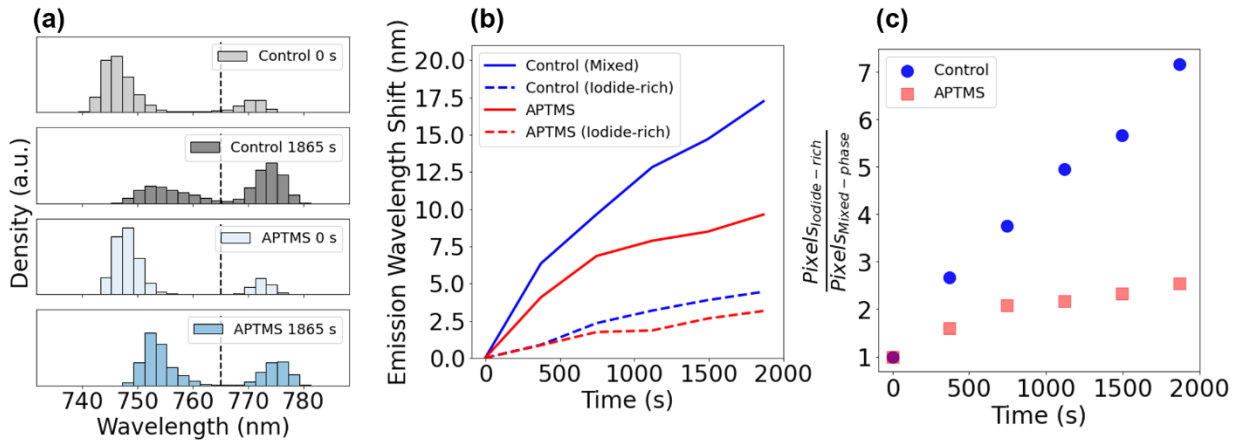

Figure S11. (a) Histograms to show the density of pixels emitting at wavelengths in the range of 735-785 nm for $Cs_{0.22}FA_{0.78}Pb(I_{0.85}Br_{0.15})_3$ control and APTMS passivated films before and at the end of photo-soaking. The dashed black line shows the 765 nm threshold used to separate out mixed-phase and iodide-rich phase regions. (b) Shift in the emission wavelength for control and APTMS passivated films in regions that are mixed and iodide rich. (c) The extent of phase-segregation calculated fraction of iodide-rich to mixed-phase pixels relative to the initial phase segregation in control and APTMS passivated films.

B3. References

(1) Jariwala, S.; Burke, S.; Dunfield, S.; Shallcross, R. C.; Taddei, M.; Wang, J.; Eperon, G. E.; Armstrong, N. R.; Berry, J. J.; Ginger, D. S. Reducing Surface Recombination Velocity of Methylammonium-Free Mixed-Cation Mixed-Halide Perovskites via Surface Passivation. *Chemistry of Materials* **2021**, *33* (13), 5035–5044. https://doi.org/10.1021/acs.chemmater.1c00848.

(2) Melitz, W.; Shen, J.; Kummel, A. C.; Lee, S. Kelvin Probe Force Microscopy and Its Application. *Surf Sci Rep* **2011**, *66* (1), 1–27. https://doi.org/10.1016/j.surfrep.2010.10.001.

Appendix C: Supporting Information for Chapter 4

C1. Experimental Methods

1.1 Materials

Lead iodide (99.99%, for perovskite precursor) and Me-4PACz (>99.0%) were purchased from TCI. Lead bromide (99.999%, ultra dry) and cesium iodide (99.999%) were purchased from Alpha Aesar. Formamidinium iodide (>99.99%), phenethylammonium iodide, and methylammonium chloride (>99.99%) were purchased from Greatcell Solar Materials. Aluminum oxide nanoparticles dissolved at 20 wt% was purchased from Sigma Alrich. All other materials were purchased from Sigma Aldrich.

1.2 Sample preparation

All preparation of perovskite samples were performed in a N_2 glovebox.

A 1.2 M $Cs_{0.17}FA_{0.83}Pb(I_{0.75}Br_{0.25})_3$ solution was prepared according to previous literature reports[43] by mixing the correct molar ratio of PbI_2, $PbBr_2$, FAI, and CsI in a 4:1 solvent ratio of N,N-Dimethylformamide (DMF) and Dimethyl sulfoxide (DMSO). 1.5 cm^2 indium tin oxide (ITO) coated glass substrates were cleaned by sequential sonication in DI water containing ~2% Micro-90 detergent, DI water, acetone, and isopropanol for 10 minutes each. The substrates were ozone-cleaned for 23 minutes prior to spincoating. Me-4PACz was dissolved in DMF at a concentration of 50 mg/mL and subsequently diluted to 1 mg/mL in isopropanol. Approximately 60 µL of the 1 mg/mL Me-4PACz solution was deposited on the substrate and spincoated at 5000 rpm for 30 s with an acceleration of 800 rpm/s. The film was annealed at 100°C for 10 minutes. Next, 100 µL of a solution with the ratio 1:150 Al_2O_3 nanoparticle to ispropanol was spincoated at 6000 rpm for 30 s with an acceleration of 800 rpm/s to wash off excess Me-4PACz and improve wettability. The substrates were annealed at 100°C for 30 s. Finally, 70 µL of the perovskite precursor solution were deposited on the substrate and spincoated at 1000 rpm for 10 s with an acceleration of 200 rpm/s followed by spinning at 5000 rpm for 35 s with an acceleration of 800 rpm/s; 10 s before the completion of the final spincoating step, 300 µL of anisole was dynamically deposited on the sample. The sample was annealed at 100°C for 45 minutes.

A 1.2 M $Cs_{0.22}FA_{0.78}Pb(I_{0.85}Br_{0.15})_3$ solution was prepared by mixing the correct molar ratio of PbI_2, $PbBr_2$, FAI, CsI and a 15 mol% relative to the Pb content equivalent of MACl to improve crystallization in a 4:1 solvent ratio of N,N-Dimethylformamide (DMF) and Dimethyl sulfoxide (DMSO). Indium tin oxide (ITO) coated glass substrates 1.5 cm^2 in size were cleaned by sequential sonication in DI water containing ~2% Micro-90 detergent, DI water, acetone, and isopropanol for 10 minutes each. The substrates were ozone-cleaned for 23 minutes prior to spincoating. Me-4PACz was first dissolved in DMF at a concentration of 50 mg/mL and was subsequently diluted to 1 mg/mL in 2-propanol (IPA). Approximately 60 µL of the 1 mg/mL Me-4PACz solution was spincoated on the substrates at 5000 rpms for 30 s with an acceleration of 800 rpm/s and annealed at 100 °C for 10 min. Next, 100 µL of IPA was dynamically spincoated on the substrate to wash

away excess Me-4PACz at 6000 rpm for 30 s with an acceleration of 800 rpm/s and annealed at 100 °C for 5 min. Following that, Al_2O_3 nanoparticles suspended in IPA was diluted further with IPA by 1:150. Approximately 50 µL of the Al_2O_3 solution was spincoated at 6000 rpm for 30 s and annealed at 100 °C for 50 s to improve the wettability of perovskite on the Me-4PACz layer. The perovskite solution was filtered through a 0.2 µm PTFE membrane filter. Approximately 60 µL of the perovskite solution was dynamically deposited on top of the substrate and spincoated at 1000 rpm for 10 s with an acceleration of 200 rpm/s followed by spinning at 5000 rpm for 35 s with an acceleration of 800 rpm/s. After 25-30 s of the second step, 330 µL of an anisole antisolvent was dynamically deposited on the spinning substrate. The half-stack was then annealed for 30 min at 100 °C on a hot plate.

1.3 Passivation

APTMS and AEAPTMS passivation of the perovskite half-stacks was performed at room temperature and ambient conditions in a vacuum oven for 4 mins. A volume of 500 µL of the silane was placed in a 4 mL vial with the perovskite sample placed face up near the vial. The vial and sample were covered with a 500 mL glass jar inside of the vacuum chamber, and the pressure was pumped down to -26 inHg relative to the atmospheric pressure, as described in previous work.[18]

PEAI passivation was performed in a nitrogen glovebox by first preparing a 0.030 M solution of PEAI in IPA. Next, 100 µL of the PEAI solution was dynamically spincoated on the perovskite surface at 3000 rpm for 30 s with an acceleration of 800 rpm/s. Following treatment with PEAI, the sample was left to rest in the nitrogen glovebox in the dark for ~24 hours prior to making measurements.[40]

1.4 UV-Vis characterization

UV-Vis absorption spectra of the perovskite control and passivated half-stacks were collected using an Agilent 8453 UV-Vis Spectrometer in a wavelength range of 200-1100 nm and an integration time of 0.5 s.

1.5 XRD characterization

X-ray diffraction measurements of the perovskite control and passivated half-stacks were measured using a Bruker D8 Discover with a Pilatus 100 K large-area 2D detector with Cu Kα radiation at 50,000 mW.

1.6 Photoluminescence characterization

trPL was measured using a PicoQuant Fluotime 100 spectrometer and Picoharp 300 TCSPC system equipped with a 640 nm pulsed diode laser with a high average power of 30 mW and 90 ps pulse width. The repetition rate of the pulsed laser was controlled with an external function generator. The laser was pulsed with an excitation intensity of ~ 30 nJ/cm^2, in order to capture the decay at a carrier density near that of one Sun power. The PL emission was passed through a 700 nm long-pass filter before reaching the detector. The PL data was fitted using a stretched exponential function, additional information of this fitting can be found in the Supporting Information. For this

measurement, the samples were measured in ambient conditions immediately after removal from a nitrogen glovebox.

Steady-state PL spectra and PLQY values were collected using an integrating sphere spectrometer (Hamamatsu Photonics K.K.) and a 532 nm continuous wave laser (CrystalLaser Lc). The integration time of the spectrometer was set to 250 ms and 5 measurements were averaged for each spectrum. The laser fluences was measured with a Thorlabs beam profiler (BP209-VIS). A continuous neutral density filter wheel (Thorlabs) was used to control the laser fluence. The neutral density filter wheel was adjusted for all measurements to be made at 100 mW/cm^2.

1.7 Confocal photoluminescence characterization

Confocal PL imaging was performed using a custom scanning confocal microscope built with a Nikon TE-2000 inverted microscope fitted with 60x dry objective (Nikon Plan Fluor, NA=0.7). A 640 nm pulsed diode laser (PDL 800-D P-C-640B, FWHM = 90 ps) was used at a repetition rate of 250 kHz, with a resulting fluence of 105 nJ/cm^2. The laser was coupled to the microscope via a FC/APC single-mode fiber and directed into the objective via a 640 dichroic cube. Sample was encapsulated under nitrogen and excited face-on (not through the substrate). The emission was filtered through a 700-850 nm bandpass filter (700 LP and 850 SP) and focused on a Single Photon Avalanche Diode from Micro Photon Devices. The PL decay was collected using a PicoHarp 300 time-correlated single photon counting (TCSPC) module. The scanning is done using a piezo nano position stage (PI). The data collection and analysis are performed through custom Python-based software.

1.8 trEFM characterization

trEFM and the required experimental setup have been discussed in detail.[33,34] Measurements were performed on an Asylum Research MFP3D-BIO mounted on a Nikon inverted optical microscope. All measurements used Pt-coated cantilevers (mikroMasch HQ/NSC15/Pt) driven at resonance frequency (~300 kHz). The sample was mounted in an inert glovebox environment in a sealed cell, then imaged under active flowing nitrogen in this sealed cell. The cantilever oscillation was recorded using a 16-bit A/D digitizer (Dynamic Signals/GaGe Razor Express CSE1622), typically at 5 MS/s, and synced to the cantilever oscillation phase (180°) using custom trigger electronics (detailed circuit information can be found in our previous reports; additional information available upon request).[33,34] In an experimental window of 16 ms, we apply a bias of +10 V to the cantilever at t = 1 ms, the sample is then allowed to equilibrate for 4 ms; the cantilever oscillation is digitized starting at t = 4.6 ms through t = 8.6 ms, and laser excitation is triggered at 5 ms and turned off at t = 7 ms. We used either a 405 nm (Omicron PhoxXplus 405-120) or a 705 nm (Omicron PhoxXplus 705-40) continuous wavelength laser at an incident intensity of ~110-150 mW/cm^2 to excite our samples; we adjust the intensity using neutral density filters and the electrical power via software control. The laser was focused via a bottom objective on an inverted optical microscope and co-aligned with the cantilever tip. The illumination intensity was measured using the combination of a calibrated photodiode and a Pixera CCD camera (150CL-CU). Raw cantilever deflection data were used to extract the instantaneous frequency by demodulating the time-dependent cantilever amplitude using a short-time Fourier transform (STFT) and then using a

parabolic estimation of the peak frequency (ridge finding) per time segment. This code is freely available online via the FFTA Python package (https://github.com/GingerLabUW/FFTA).

C2. Supplementary figures and discussions

Note 1. Cantilever calibration for trEFM time constant extraction.

The experimental and theoretical background behind trEFM is described in significant detail in our previous works[1,2] and by Tirmzi, et al.[3] Here, we summarize the cantilever calibration procedure for the sake of reference.

During the trEFM experiment, we digitize the deflection or the raw oscillation of the cantilever, and then we demodulate it using a Short-Time Fourier Transform (STFT). Many demodulation methods work, such as non-stationary Fourier mode decomposition,[4] which demonstrates improved signal-to-noise extraction but is computationally expensive and slow. Hilbert Transforms[1,5] are computationally fast, but less robust to the experimental noise we observe. Thus, we use STFT to demodulate our data to balance the signal-to-noise we obtain and computation time. We then use a product of two exponentials (**Equation 1**) to empirically fit the change in frequency (Δf), including the transient response and cantilever relaxation (shown in main text Figure 4.1c), and extract the time it takes for the cantilever's frequency to shift to its maximum deviation from the drive frequency after the illumination trigger.

Equation 1.

$$\Delta f = A \times \left[\exp\left(-\frac{t}{\tau_1}\right) - 1\right] \times \left[-\exp\left(-\frac{t}{\tau_2}\right)\right]$$

Where A is a coefficient that accounts for the magnitude of the frequency shift, t is time, τ_1 describes the transient decay, and τ_2 describes the cantilever relaxation.

We call the time it takes for the cantilever's frequency to shift to its maximum deviation from the drive frequency the "time-to-first-peak" or t_{fp}. The t_{fp} is cantilever-dependent, meaning physical qualities of the cantilever like its spring constant or quality factor affect the frequency response. Because the frequency response is cantilever-specific, we must extract the cantilever-independent dynamics via a calibration of the frequency response to a time constant that describes the transient response of interest (main text Figure 4.1c). We collect the relevant cantilever parameters during the trEFM experiment, enabling us to use our model[6] to simulate a t_{fp} to τ calibration curve (Figure S1), which we use to obtain the cantilever-independent equilibration time maps shown in this work.

2.1 Example simulated calibration curve for extraction of cantilever-independent τ values.

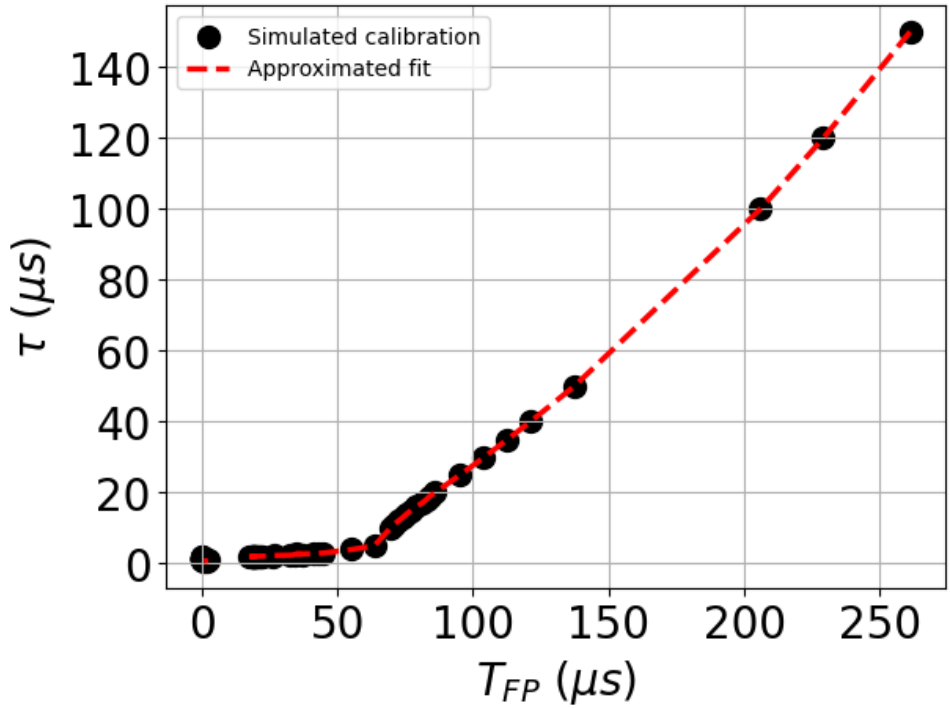

Figure S1. shows characteristic time constant, τ, plotted against time-to-first peak, t_{fp}, obtained from simulation; this calibration curve is used to map experimentally obtained t_{fp} values to cantilever-independent τ values that describe the external force perturbation to the cantilever's oscillation (refer to Note 1). We use our publicly available FFTA Python package to generate this calibration curve.[6]

2.2 Topography of large-scale ROI to correlate trEFM with confocal PL microscopy.

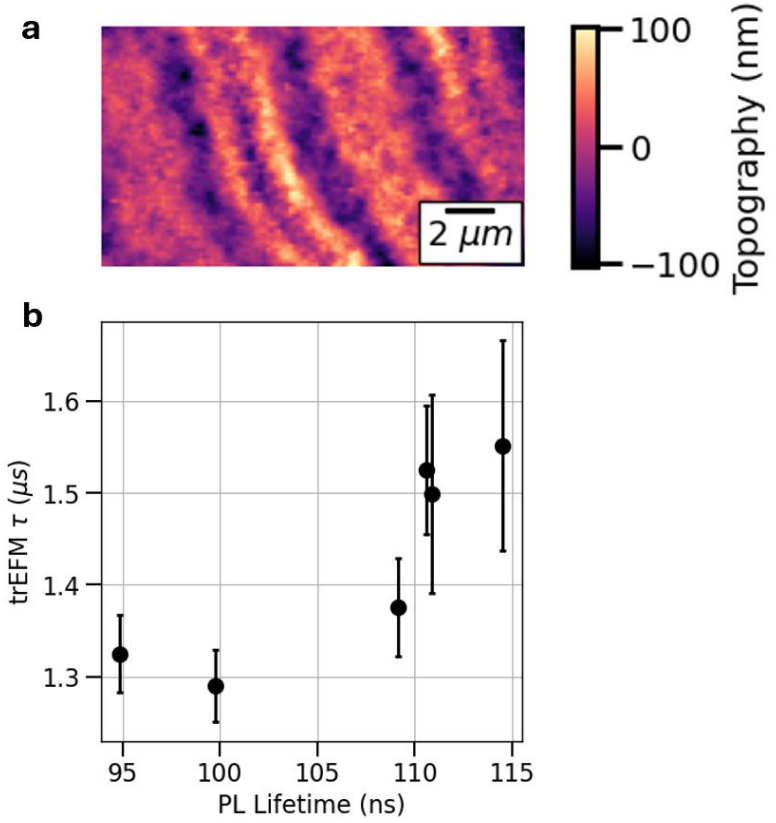

Figure S2. (a) Topography of large-scale ROI shown in main text Figure 4.1d-e. **(b)** trEFM surface potential equilibration time constants plotted against trPL lifetimes in correlated regions. trPL lifetimes were collected with using 60× objective, NA=0.7, using a 640 nm laser at a fluence of 105 nJ/cm^2.

Note 2. Fitting trPL decays with stretch exponential.

We fit the measured trPL decays using a stretched exponential function as described in **Equation 2** below. The stretched exponential function uses both a characteristic lifetime (τ_C) and a β-factor which describe the time to reach 1/e of the initial signal and the degree of heterogeneity in emitting states; a β-factor closer to 1 means emission is more homogenous, and the stretched exponential function collapses into a mono-exponential function.[7]

Equation 2.

$$y = \exp\left(-\frac{t}{\tau_C}\right)^{\beta}$$

From the τ_C and β-factor, we calculated the average trPL lifetimes as shown in **Equation 3**; this takes into account the amount of heterogeneity that exists in halide perovskite emission.[7]

Equation 3.

$$< \tau > = \frac{\tau_C}{\beta}\Gamma\left(\frac{1}{\beta}\right)$$

2.3 UV-vis absorbance and XRD spectra to characterize perovskite half-stack samples and passivations.

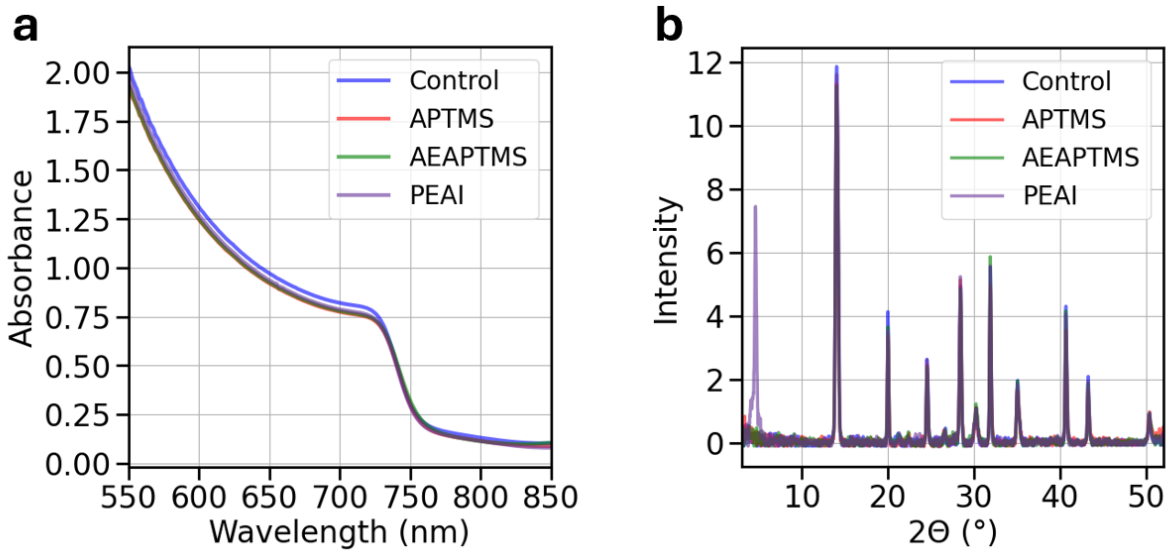

Figure S3. (a) UV-vis absorbance of half-stack samples including the unpassivated control and APTMS-, AEAPTMS-, and PEAI-passivated samples showing negligible change in overall absorbance after passivation. UV-vis characterization protocol described in main text Methods. **(b)** XRD spectra of half-stack samples including the unpassivated control and APTMS-, AEAPTMS-, and PEAI-passivated samples showing negligible change in perovskite diffraction peaks and presence of PEAI salt peak at 4.6°.[8]

2.4 PL spectra and trPL decays of perovskite half-stacks before and after surface passivation treatments.

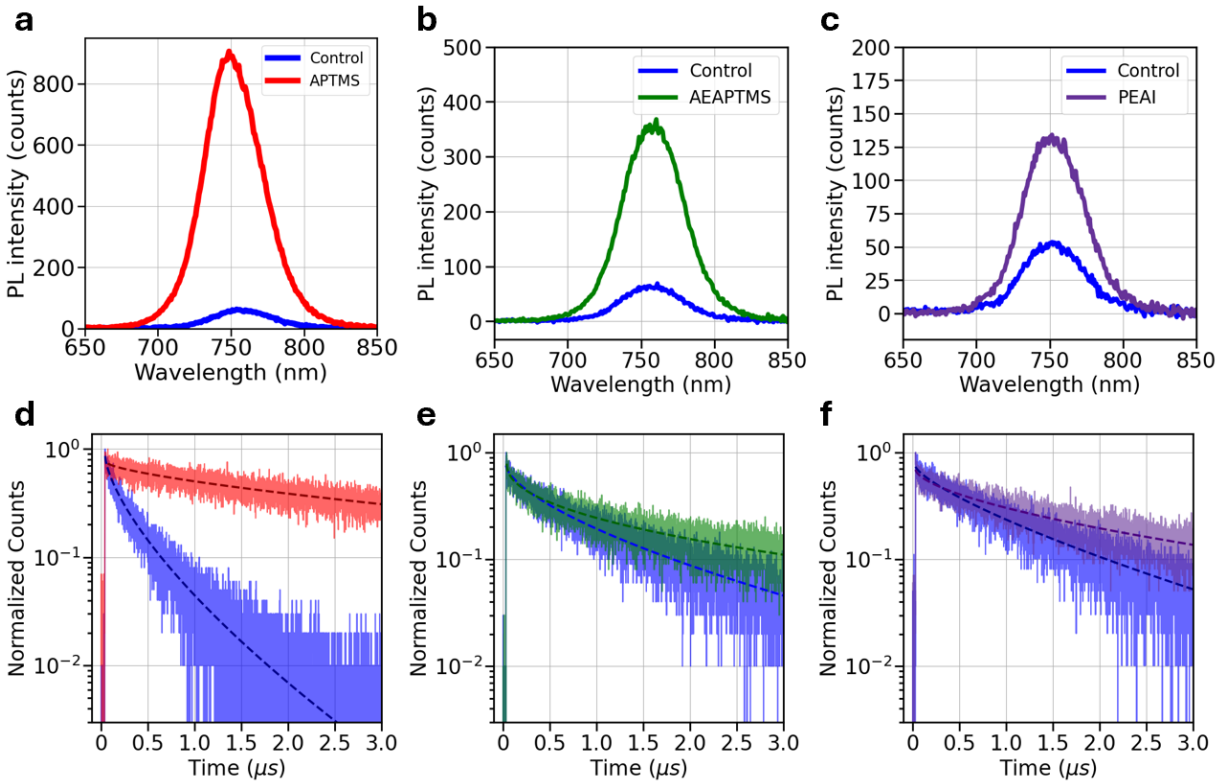

Figure S4. (a)-(c) PL spectra of control and passivated half-stack samples for APTMS, AEAPTMS, and PEAI passivation respectively. **(d)-(f)** trPL decays for control and passivated half-stack samples for APTMS, AEAPTMS, and PEAI passivation respectively.

Table 1. Stretched exponential fitting parameters for Glass/ITO/Me-4PACz/$Cs_{0.22}FA_{0.78}Pb(I_{0.85}Br_{0.15})_3$ half-stack samples before and after passivation with AEAPTMS and PEAI.

Sample	τ_C (ns)	β-factor
Control	598	0.64
AEPTMS	684	0.46
Control	814	0.75
PEAI	1335	0.60

2.5 Photoluminescence quantum yields (PLQY) for control and passivated samples.

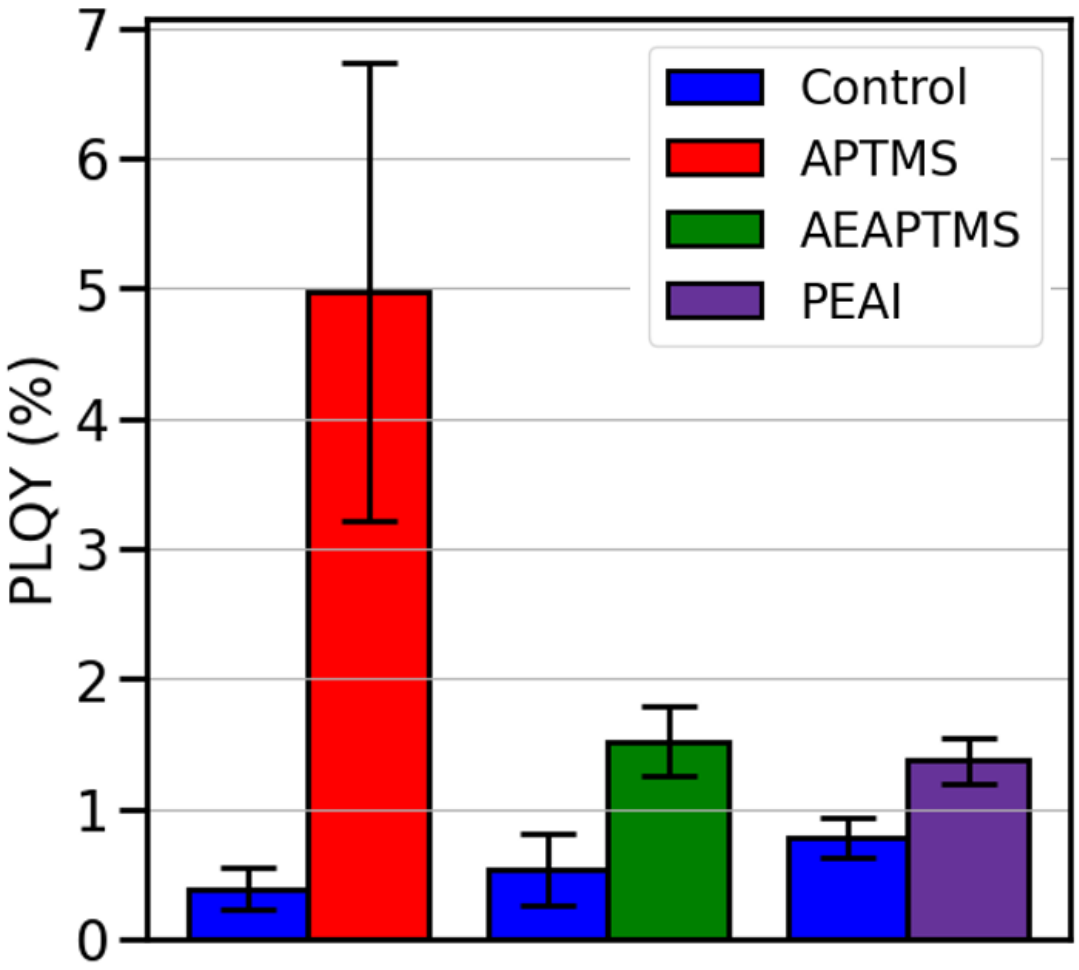

Figure S5. Shows PLQY enhancement after passivation with each passivator. The bar represents the average of 3 different samples and the error bars are the standard deviation.

2.6 trEFM measurements of AEAPTMS and PEAI treatment.

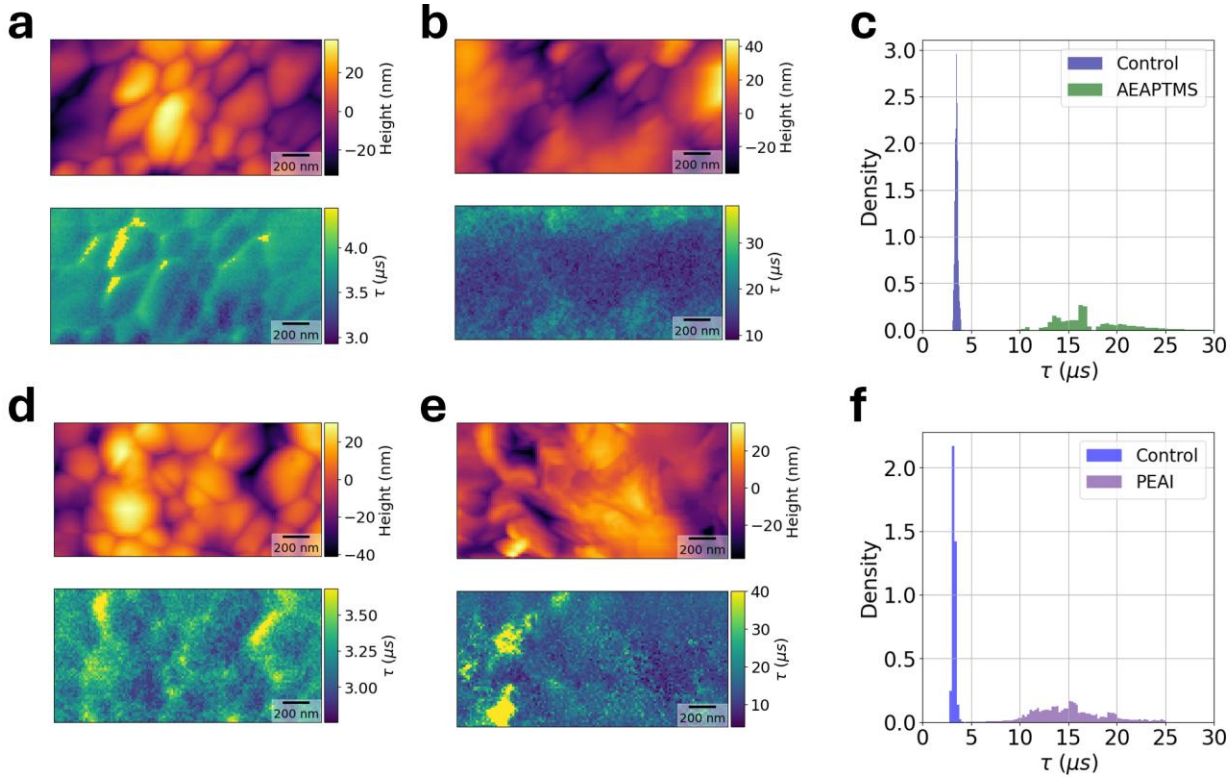

Figure S6. (a) Representative topography and trEFM time constant image of control and **(b)** AEAPTMS treated half-stack samples. **(c)** Associated histogram that shows slower surface potential equilibration times after treatment. **(d)** Representative topography and trEFM time constant image of control and **(e)** PEAI treated samples. **(f)** Associated histogram that also displays slower surface potential equilibration times after treatment.

Note 3. Approximation of surface recombination velocity (SRV) from trPL effective lifetimes.

We approximate the SRV at the surface of the perovskite from the trPL measurements using **Equation 4**. Here, τ_{surf}, W, and D describe the carrier lifetime at the surface, the perovskite thickness (500 nm), and electronic carrier diffusion coefficient (assumed to be 0.75 cm^2/s). We can determine τ_{surf} from the effective carrier lifetime (τ_{eff}) and the bulk carrier lifetime (τ_{bulk}) as shown in **Equation 5**. We take the average trPL lifetimes as the τ_{eff} and assume the τ_{bulk} to be 8000 ns and the surface recombination velocity at the perovskite/substrate interface to be negligible, as previous reported.[9,10]

Equation 4.

$$SRV = \frac{W}{\tau_{surf} - \left(\frac{4}{D}\right)\left(\frac{W}{\pi}\right)^2}$$

Equation 5.

$$\tau_{surf} = \left(\frac{1}{\tau_{eff}} - \frac{1}{\tau_{bulk}}\right)^{-1}$$

2.7 Histograms of the trEFM surface potential equilibration times measured in three ROIs of a control and APTMS-treated $Cs_{0.22}FA_{0.78}Pb(I_{0.85}Br_{0.15})_3$ half-stack sample.

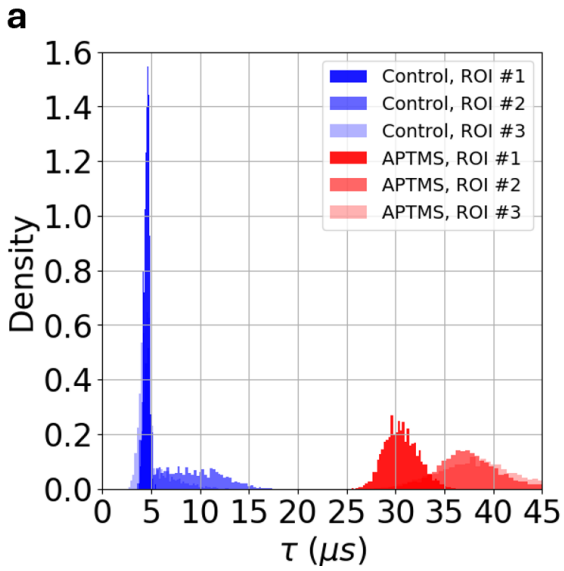

Figure S7. (a) Density normalized histograms showing the trEFM time constants measured across three unique ROIs in a Glass/ITO/Me-4PACz/$Cs_{0.22}FA_{0.78}Pb(I_{0.85}Br_{0.15})_3$ half-stack before and after APTMS treatment. The control and APTMS ROIs are also unique from one another.

Table 2. Average values of the trEFM surface potential equilibration times measured in three separate $Cs_{0.22}FA_{0.78}Pb(I_{0.85}Br_{0.15})_3$ half-stack samples before and after APTMS passivation.

Sample	Control <τ> (μs)	APTMS <τ> (μs)
1	10.5	35.0
2	5.4	14.2
3	5.5	35.5

Note 4: On surface potential equilibration in perovskite systems as modeled by drift diffusion simulations.

We assume that the surface potential in our simulations is dominated by electronic carrier dynamics because we observe equilibration of the surface potential on the scale of microseconds, while ion migration is typically on the minute timescale (see **Equation 6**).[11,12]

Equation 6.

$$\tau_{ion} = \frac{b}{D_I}\sqrt{\frac{V_T \varepsilon_A}{q\widehat{N}_0}}$$

Where τ_{ion} is the time constant that describes mobile ions migrating to the Debye layers in perovskite thin films, b is the sample thickness, D_I is the ion diffusion coefficient, V_T is the built in voltage, ε_A is the dielectric constant of the absorber, q is the elementary charge, and $\widehat{N}_0$ is the mean cation vacancy density (cation vacancies are assumed to be relatively stationary compared to anion vacancies, and cation vacancy density is assumed to be equal to mean anion vacancy density, so $\widehat{N}_0$ represents mobile ion concentration).[11–13] Given the parameters in **Table 3**, ion motion occurs on the scale of several minutes. Because the electric potential in the sample is calculated according to Poisson's Equation ($\frac{d^2\phi}{dt^2} = \frac{q}{\varepsilon_A}\left(\widehat{N}_0 - P + n - p\right)$, where ϕ is potential, P is mobile anion vacancy, n is electron concentration, and p is hole concentration), we can use electronic carrier dynamics to explain the surface potential equilibration timescale. That said, if we increase the concentration of mobile ions (increase $\widehat{N}_0$, because $\widehat{N}_0$= P), we will observe slower surface potential equilibration dynamics due to the proportionally larger contribution from extremely slow ion motion.

We propose that the carrier equilibrium condition can be described by the following set of equations:

Equation 7.

$$G = R = -\frac{dn}{dt}$$

Where G is carrier generation rate, R is carrier recombination rate, n is electronic carrier concentration, and t is time. We describe recombination with the following equation:

Equation 8.

$$R = \frac{1}{\tau_{SRH}}[(n_0 + \Delta n)] + \beta[(n_0 + \Delta n)(p_0 + \Delta p)]$$

Where τ_{SRH} is the nonradiative recombination carrier lifetime, n_0 and p_0 are the electron and hole concentrations in the dark, Δn and Δp are the change in electron and hole concentrations, and β is the bimolecular recombination rate constant. Here, we assume that there is no Auger-Meitner

recombination.[7,11] At the surface, there is an additional recombination term to account for surface recombination velocity, which we describe with the following:

Equation 9.

$$R_{surface} = SRV \times \Delta n$$

Where SRV is the surface recombination velocity at the perovskite/surface interface. Given our electronic carrier equilibrium condition described in **Equation 7** (G = R), carrier concentrations in a sample with a higher SRV term will reach equilibrium at earlier times than a sample with lower SRV.

We fit the surface potential evolution with a tri-exponential function to extract an average time constant to describe the rise time, though we note that this time constant is a phenomenological representation of surface potential equilibration dynamics and the trends should be interpreted as qualitative rather than quantitative in capturing the trEFM experiment.

2.8 Effects of the nonradiative recombination rate constant on the surface potential equilibration time.

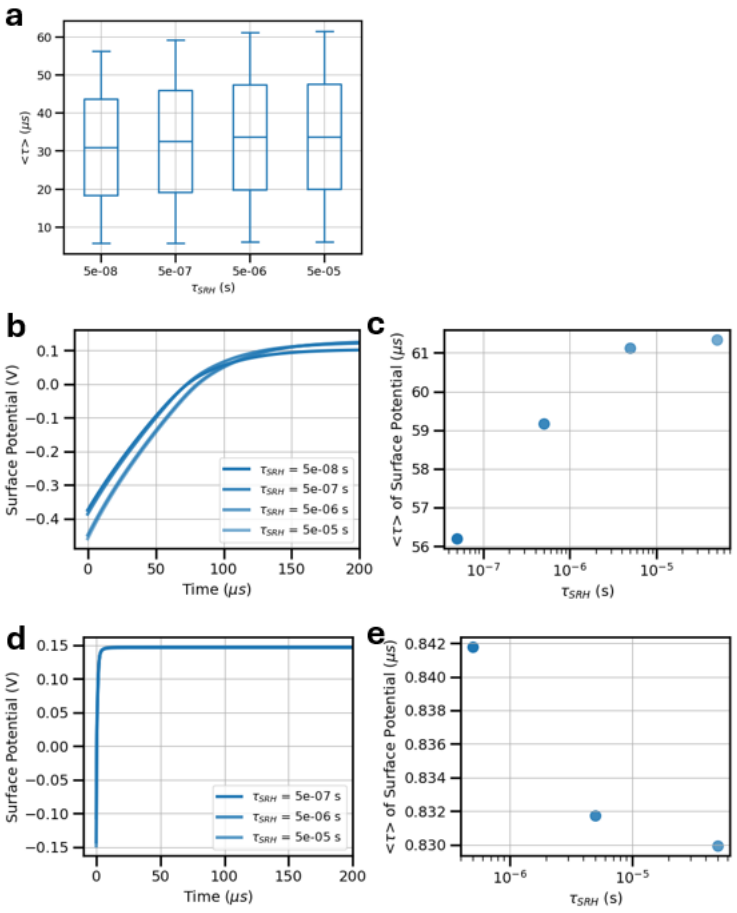

Figure S8. (a) Boxplot showing <τ> values calculated from tri-exponential fits of simulated surface potential traces with 405 nm, 1 mW/cm^2 excitation, showing slight increase in surface potential equilibration time with increasing Shockley Read Hall carrier lifetime (τ_{SRH}); at low fluences, increasing nonradiative recombination lifetime leads to slower equilibration times, which is also shown in **(b)** example surface potential evolutions and **(c)** <τ> fits for those examples; however, at higher excitation intensities like 100 mW/cm^2, τ_{SRH} shows little to no effect on the surface potential equilibration time, as seen in **(d)** and **(e)**. Because τ_{SRH} primarily affects bulk carrier dynamics, we expect that the surface recombination velocity dominates the carrier dynamics at the surface of the absorber. For full simulation details, see Table 3, where the primary parameters swept for **(b)-(e)** are τ_{SRH} (s) and illumination intensity (scalar), and all other parameters are held constant. Boxplot mid-line is the median, box edges are the first and third quartiles of the data, and the whiskers show the range of the data.

2.9 Effects of the bimolecular recombination rate constant on the surface potential equilibration time.

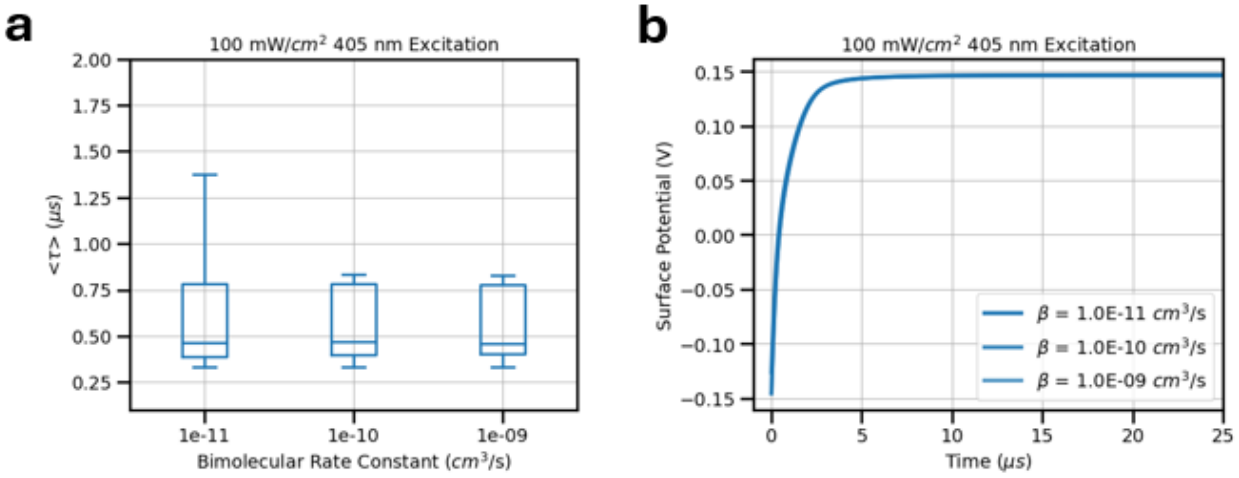

Figure S9. (a) Boxplot showing <τ> values calculated from a tri-exponential fit of simulated surface potential versus bimolecular rate constants, where simulated excitation was 405 nm at 100 mW/cm^2, similar to experimental conditions described in text; **(b)** example surface potential traces with varied bimolecular rate constants for 100 mW/cm^2 405 nm excitation with all other parameters held constant. For full simulation details, see Table 3. We recognize that bimolecular recombination rate may be affected by surface passivation,[14] but these simulations show that the bimolecular rate constant has a relatively minor effect on the surface potential evolution. Boxplot mid-line is the median, box edges are the first and third quartiles of the data, and the whiskers show the range of the data.

Table 3. IonMonger simulation parameters used to simulate perovskite surface potential evolution.

Parameter	Value(s)	Reference
Thickness	500 nm	N/A
Bandgap	1.7 eV	[11]
Absorption coefficient (α)	405 nm: 2.42085×10^{7} m^{-1} 705 nm: 2.5807×10^{6} m^{-1}	[7]
Photon flux (F_{ph})	405 nm: 2.05×10^{21} $m^{-2}s^{-1}$ 705 nm: 3.55×10^{21} $m^{-2}s^{-1}$	N/A
Illumination Intensity (scalar)	0.01 – 10 (scalar of 1 used for all 100 mW/cm^2 simulations)	N/A
Dielectric constant (ε_A)	$24.1\times\varepsilon_0$ Fm^{-1}	[11,15,16]
Mobile ion concentration (N_0)	1×10^{13} - 1×10^{17} cm^{-3}	[17–23]
Ion diffusion coefficient (D_I)	1×10^{-13} cm^2s^{-1}	[16–23]
Carrier diffusion coefficient (D)	7.5×10^{-3} – 7.5×10^{-1} cm^2s^{-1}	[7,16,24,25]
Nonradiative recombination lifetime (τ_{SRH})	5×10^{-8} - 5×10^{-5} s	[7,24]
Bimolecular recombination rate constant (β)	1×10^{-11} - 1×10^{-9} cm^3s^{-1}	[7,11,15]
Auger-Meitner recombination rate	1×10^{-28} cm^6s^{-1}	[7,15]
Surface recombination velocity (SRV)	1×10^{-1} - 1×10^{3} cm s^{-1}	[7,9–11,15,26]

2.10 Binary mask used to separate grain interiors and boundaries.

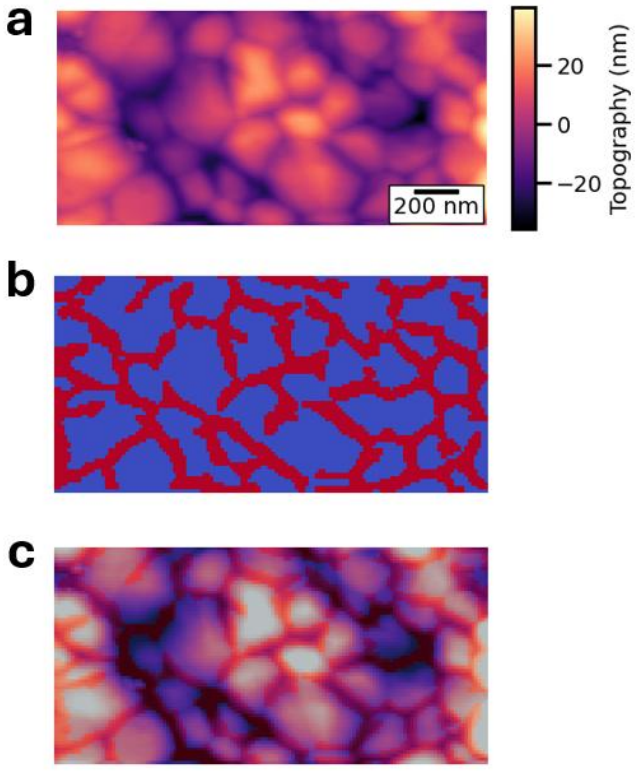

Figure S10. (a) Representative topography of illumination bias region of interest shown in Figure 4.4 of the main text; **(b)** binary mask calculated from topography representing grain boundaries (red) and grain interiors (blue); and **(c)** binary mask overlaid on topography.

2.11 Binary mask used to separate grain interiors and boundaries for second region of interest.

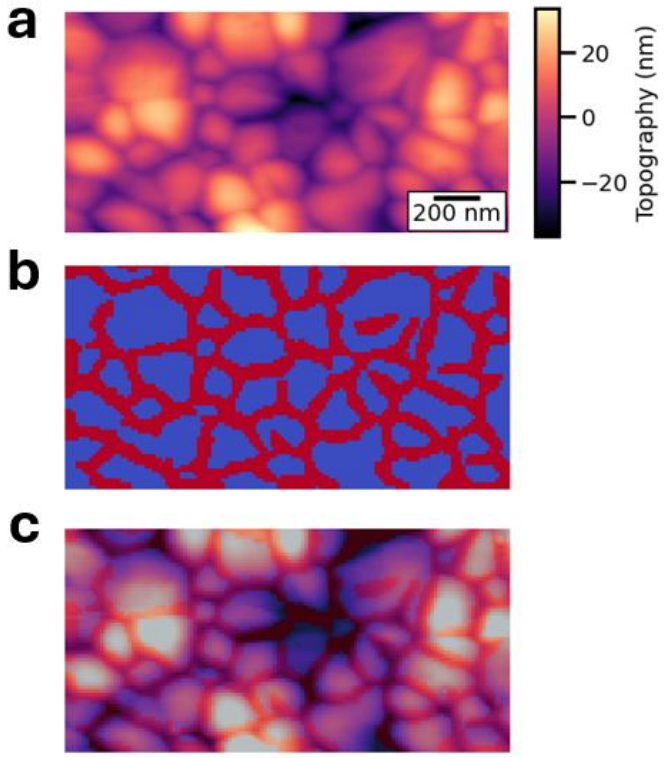

Figure S11. (a) Representative topography of illumination bias *second* region of interest (see Figure S12); **(b)** binary mask calculated from topography representing grain boundaries (red) and grain interiors (blue); and **(c)** binary mask overlaid on topography.

2.12 Illumination bias data for second region of interest (same illumination conditions as main text Figure 4.4).

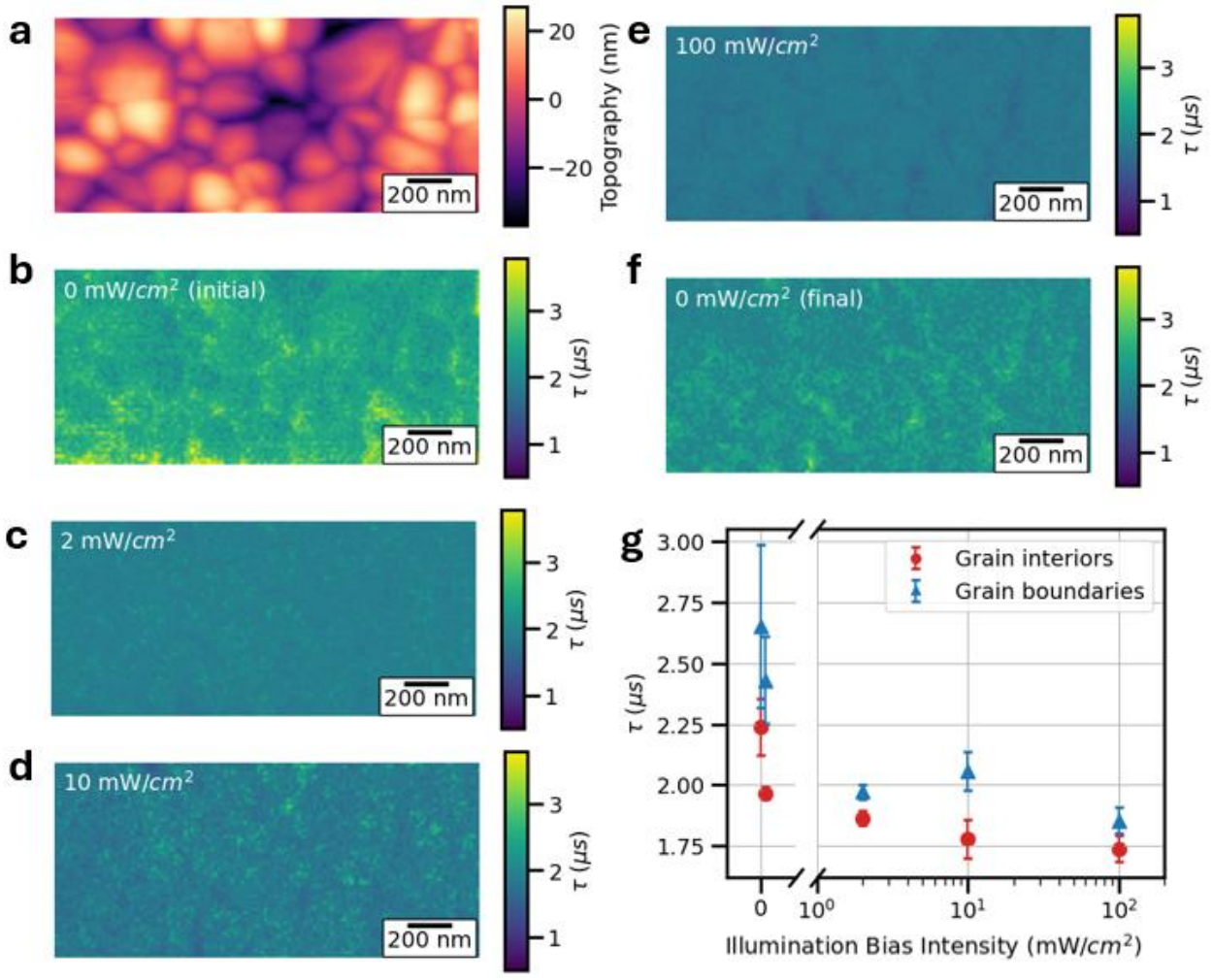

Figure S12. (a) Representative topography of second ROI, showing nanoscale morphology; **(b)-(e)** trEFM surface potential equilibration time images of the same ROI with increasing 660 nm bias illumination intensity ranging from 0 mW/cm2 to 100 mW/cm2, where a fast 405 nm laser at 110 mW/cm2 was used for trEFM excitation; **(f)** reproduced trEFM surface potential equilibration time image at 0 mW/cm2 showing return to unbiased time constants; **(g)** average grain interior and boundary trEFM surface potential equilibration times with respect to illumination bias intensity, error bars show standard deviation of masked pixel selection. Figure S11 shows binary mask used to extract grain boundary and interior data. Mean grain interior trEFM surface potential equilibration times decrease 22.1% at 100 mW/cm^2 with respect to unbiased image, and mean grain boundary trEFM time constants decrease 27.0%.

2.13 Binary mask used to separate grain interiors and boundaries for third region of interest.

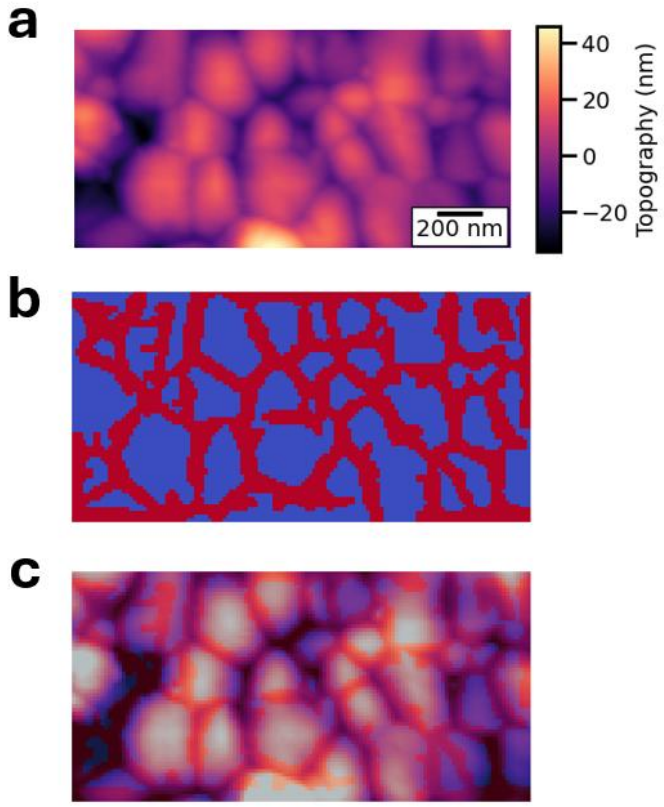

Figure S13. (a) Representative topography of illumination bias *third* region of interest where sample was biased with variable intensity 455 nm light and excited with the fast 405 nm laser (see Figure S14); **(b)** binary mask calculated from topography representing grain boundaries (red) and grain interiors (blue); and **(c)** binary mask overlaid on topography

2.14 Illumination bias data for third region of interest.

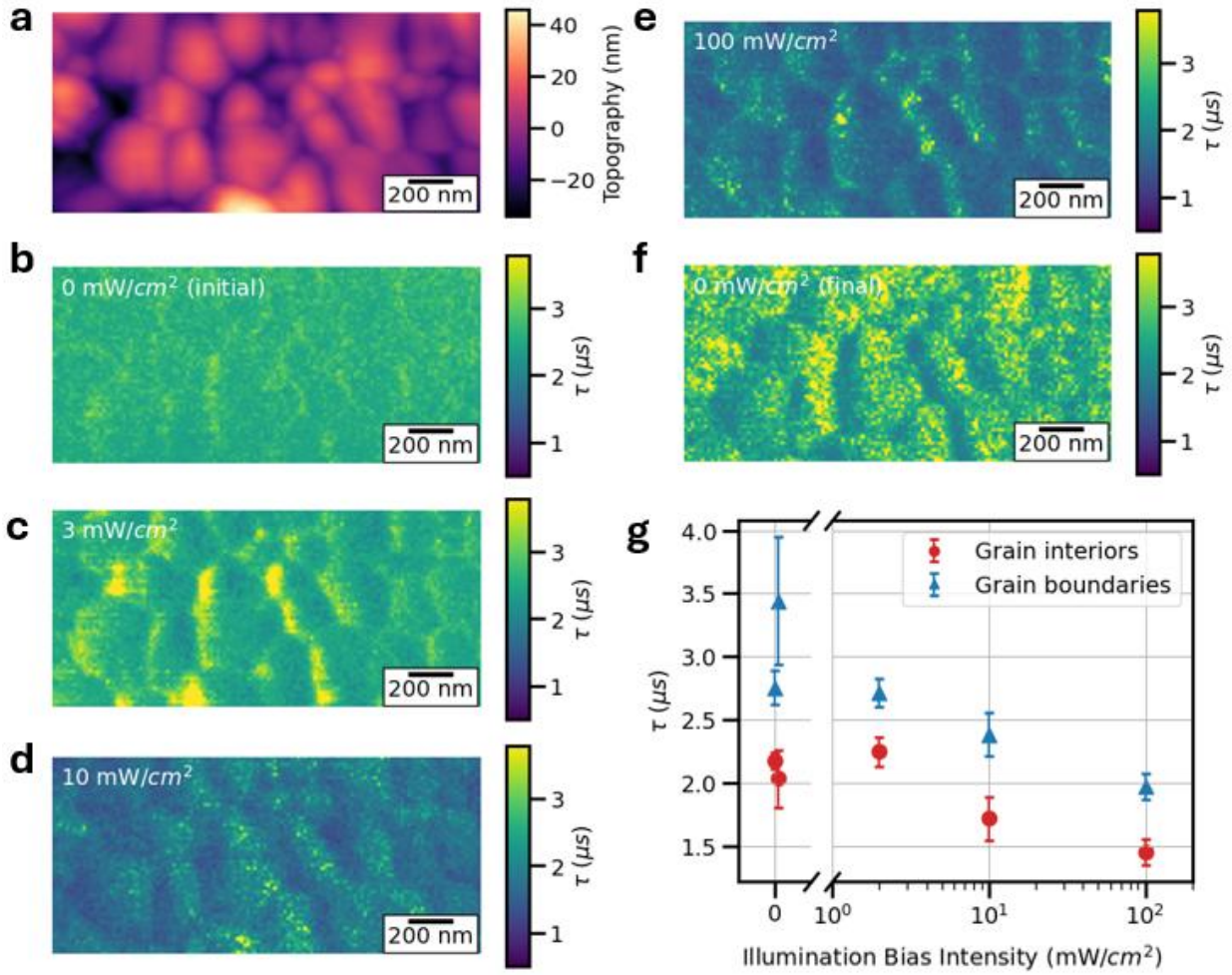

Figure S14. (a) Representative topography of third ROI, showing nanoscale morphology; **(b)-(e)** trEFM surface potential equilibration time images of the same ROI with increasing 455 nm bias illumination intensity ranging from 0 mW/cm2 to 100 mW/cm2, where a fast 405 nm laser at 110 mW/cm2 was used for trEFM excitation; **(f)** reproduced trEFM surface potential equilibration time image at 0 mW/cm2 showing return to unbiased surface potential equilibration times; **(g)** average grain interior and boundary trEFM surface potential equilibration times with respect to background illumination bias intensity, error bars show standard deviation of masked pixel selection. Figure S13 show the mask used for grain boundary and interior analysis. Mean grain interior trEFM surface potential equilibration times decrease 17.6% at 100 mW/cm^2 with respect to unbiased image, and mean grain boundary trEFM surface potential equilibration times decrease 31.2%.

2.15 Excitation intensity dependent trPL lifetimes.

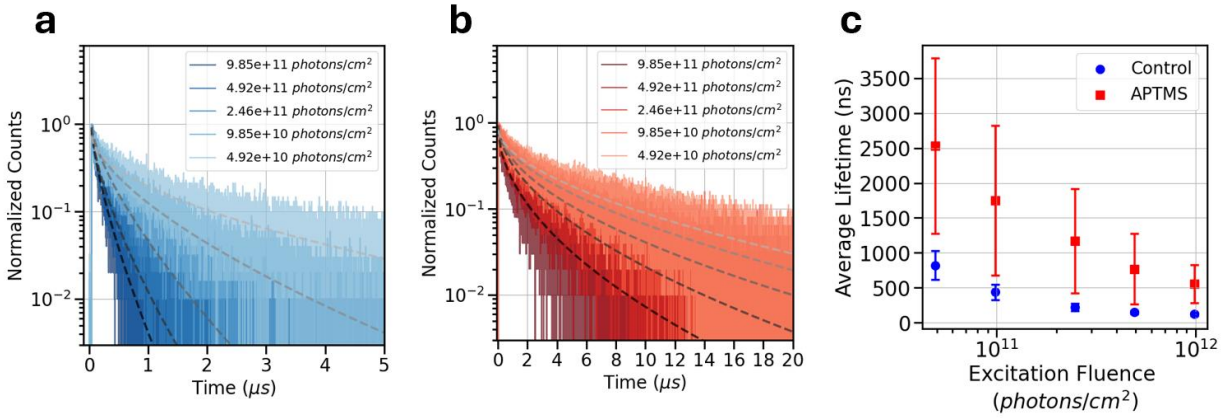

Figure S15. (a) Representative measured trPL decays for a $Cs_{0.22}FA_{0.78}Pb(I_{0.85}Br_{0.15})_3$ half-stacks before and **(b)** after APTMS passivation with varied excitation fluences. Stretched exponential fits are shown with the dashed lines. **(c)** Average trPL lifetime measured as a function of the excitation intensity of a 640 nm laser for a set of $Cs_{0.22}FA_{0.78}Pb(I_{0.85}Br_{0.15})_3$ half-stacks before and after passivation. The average value is calculated from measurements made on three separate samples and the error bars represent the standard deviation of those three samples. See Table 4 for fitting parameters.

2.16 Excitation intensity dependent trEFM measurements.

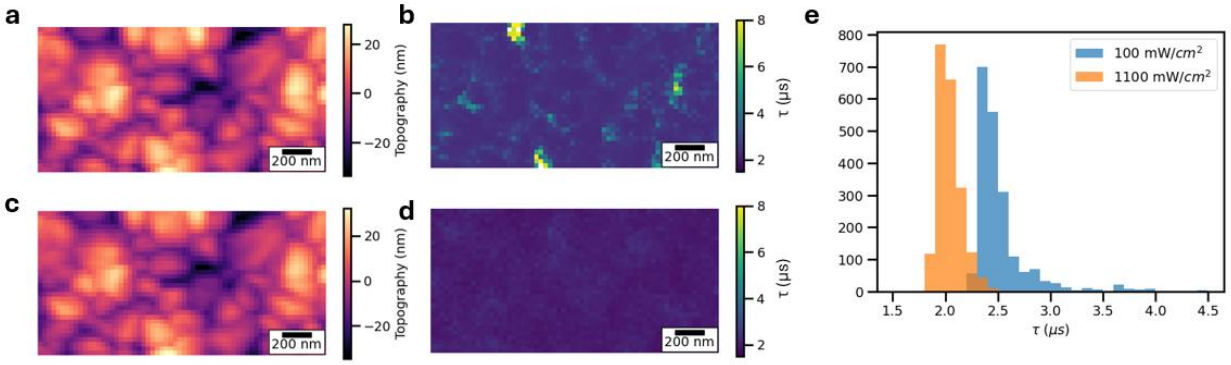

Figure S16. (a) Representative topography of a $Cs_{0.22}FA_{0.78}Pb(I_{0.85}Br_{0.15})_3$ half-stack showing nano-scale grains; **(b)** trEFM surface potential equilibration time map from 100 mW/cm^2 excitation with 405 nm laser showing slower dynamics at grain boundaries, as expected (see main text Figure 4.2d); **(c)** topography of the same region of interest; **(d)** trEFM surface potential equilibration time map from image taken with 1100 mW/cm^2 405 nm excitation, showing no observed contrast at grain boundaries and faster dynamics overall; and **(e)** histogram of these two trEFM surface potential equilibration time images validating our observation of faster (and lower contrast) surface potential equilibration dynamics captured with higher excitation intensity; at higher excitation intensity, higher order recombination dynamics have a higher contribution to overall electronic carrier recombination, meaning the sample reaches its equilibrium condition at earlier times.

2.17 IonMonger excitation intensity simulations.

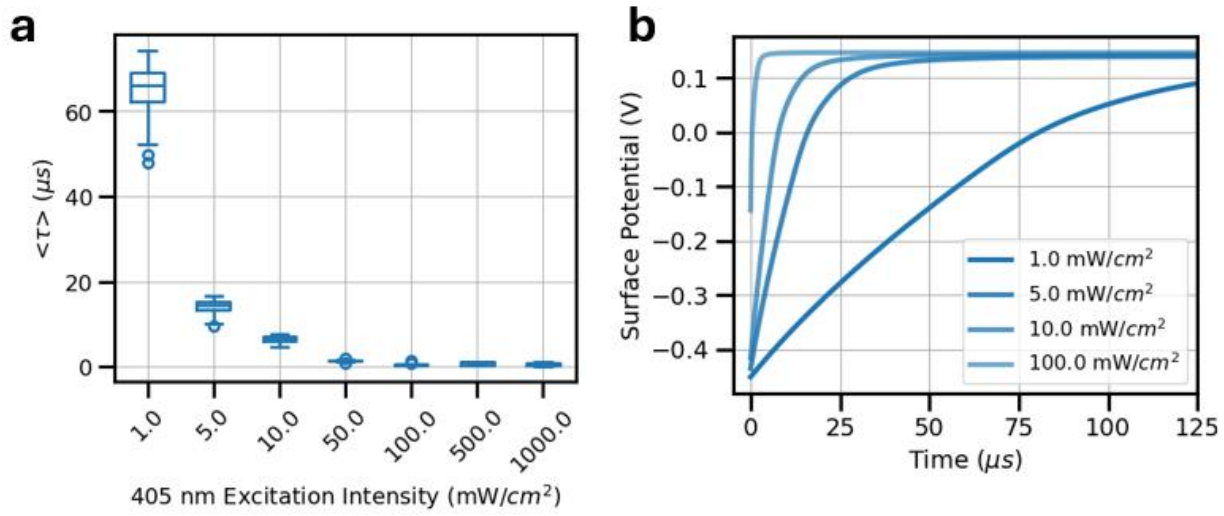

Figure S17. (a) Boxplot showing <τ> values calculated from tri-exponential fits of simulated surface potential dynamics plotted against excitation intensity with 405 nm excitation, showing faster dynamics when absorber is excited with higher intensity light; **(b)** shows example surface potential traces with varied excitation intensities, demonstrating faster dynamics with higher excitation intensity. For full simulation details, see Table 3, where primary parameter swept was Illumination Intensity (scalar).

2.18 Wavelength dependent trEFM measurements.

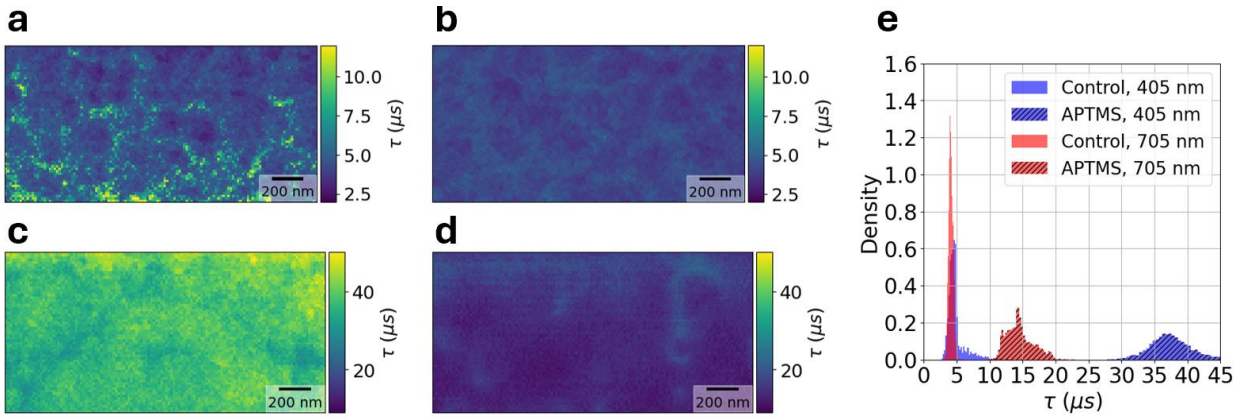

Figure S18. (a) Representative trEFM surface potential equilibration time images for $Cs_{0.22}FA_{0.78}Pb(I_{0.85}Br_{0.15})_3$ control half-stacks excited with 405 nm and **(b)** 705 nm fast lasers. **(c)** Representative trEFM surface potential equilibration time images for APTMS-treated half-stacks excited with 405nm and **(d)** 705 nm fast lasers. All images were collected with an incident intensity of ~150 mW/cm^2. Note that **(a)** and **(b)** share a color bar and **(c)** and **(d)** share a color bar to show the difference observed with different wavelengths. **(e)** Histogram representations of all images where 405 nm excitation, 705 nm excitation, and APTMS-treatment correspond to blue, red, and hashed appearance, respectively. Excitation with 705 nm light yields faster surface potential equilibration times compared to excitation with 405 nm light.

2.19 IonMonger wavelength dependence simulations.

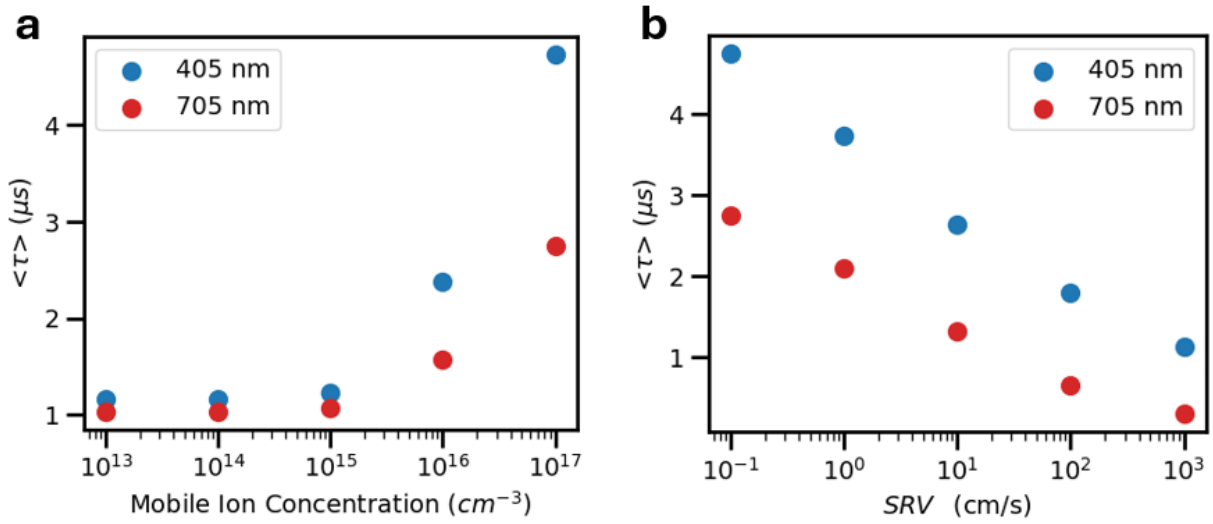

Figure S19. (a) <τ> values calculated from a tri-exponential fit to simulated surface potential evolution, plotted against variable mobile ion concentrations for 405 nm and 705 nm excitation, showing 705 nm excitation consistently results in faster surface equilibration dynamics; and **(b)** showing that at varied surface recombination velocities, 705 nm excitation still results in faster equilibration dynamics than 405 nm excitation. For full simulation details, see Table 3, where the primary parameters swept were mobile ion concentration and surface recombination velocity, with all other parameters held constant.

Table 4. Excitation fluence dependent stretched exponential fitting parameters for Glass/ITO/Me-4PACz/$Cs_{0.22}FA_{0.78}Pb(I_{0.85}Br_{0.15})_3$ half-stack samples before and after passivation with APTMS. Representative for Figure S15a,b.

Sample, Fluence (photons/cm^2)	τ_C (ns)	β-factor
Control, 9.85e11	92	0.72
Control, 4.92e11	118	0.69
Control, 2.46e11	209	0.72
Control, 9.85e10	390	0.65
Control, 4.92e10	566	0.54
APTMS, 9.85e11	504	0.52
APTMS, 4.92e11	853	0.54
APTMS, 2.46e11	1261	0.54
APTMS, 9.85e10	1929	0.57
APTMS, 4.92e10	2483	0.57

C3. References

(1) Giridharagopal, R., Rayermann, G. E., Shao, G., Moore, D. T., Reid, O. G., Tillack, A. F., Masiello, D. J. & Ginger, D. S. Submicrosecond time resolution atomic force microscopy for probing nanoscale dynamics. *Nano Lett.* **12**, 893–898 (2012).

(2) Karatay, D. U., Harrison, J. S., Glaz, M. S., Giridharagopal, R. & Ginger, D. S. Fast time-resolved electrostatic force microscopy: Achieving sub-cycle time resolution. *Rev. Sci. Instrum.* **87**, 1–11 (2016).

(3) Tirmzi, A. M., Dwyer, R. P., Jiang, F. & Marohn, J. A. Light-Dependent Impedance Spectra and Transient Photoconductivity in a Ruddlesden-Popper 2D Lead-Halide Perovskite Revealed by Electrical Scanned Probe Microscopy and Accompanying Theory. *J. Phys. Chem. C* **124**, 13639–13648 (2020).

(4) Shea, D. E., Giridharagopal, R., Ginger, D. S., Brunton, S. L. & Kutz, J. N. Extraction of Instantaneous Frequencies and Amplitudes in Nonstationary Time-Series Data. *IEEE Access* **9**, 83453–83466 (2021).

(5) Yazdanian, S. M., Marohn, J. A. & Loring, R. F. Dielectric fluctuations in force microscopy: Noncontact friction and frequency jitter. *J. Chem. Phys.* **128**, (2008).

(6) Rajiv Giridharagopal. FFTA. *GitHub repository, https://github.com/rajgiriUW/ffta* (2021).

(7) Taddei, M., Jariwala, S., Westbrook, R. J. E., Gallagher, S., Weaver, A. C., Pothoof, J., Ziffer, M. E., Snaith, H. J. & Ginger, D. S. Interpreting Halide Perovskite Semiconductor Photoluminescence Kinetics. *ACS Energy Lett.* **9**, 2508–2516 (2024).

(8) Jiang, Q., Zhao, Y., Zhang, X., Yang, X., Chen, Y., Chu, Z., Ye, Q., Li, X., Yin, Z. & You, J. Surface passivation of perovskite film for efficient solar cells. *Nat. Photonics* **13**, 460–466 (2019).

(9) Jariwala, S., Burke, S., Dunfield, S., Shallcross, R. C., Taddei, M., Wang, J., Eperon, G. E., Armstrong, N. R., Berry, J. J. & Ginger, D. S. Reducing surface recombination velocity of methylammonium-free mixed-cation mixed-halide perovskites via surface passivation. *Chem. Mater.* **33**, 5035–5044 (2021).

(10) Wang, J., Fu, W., Jariwala, S., Sinha, I., K-Y Jen, A. & Ginger, D. S. Reducing Surface Recombination Velocities at the Electrical Contacts Will Improve Perovskite Photovoltaics. *ACS Energy Lett.* **14**, 222–227 (2019).

(11) Courtier, N. E., Cave, · J M, Walker, · A B, Richardson, · G & Foster, · J M. IonMonger: a free and fast planar perovskite solar cell simulator with coupled ion vacancy and charge carrier dynamics. *J Comput Electron* **18**, 1435–1449 (2019).

(12) Courtier, N. E., Richardson, G. & Foster, J. M. A fast and robust numerical scheme for solving models of charge carrier transport and ion vacancy motion in perovskite solar cells. *Appl. Math. Model.* **63**, 329–348 (2018).

(13) Courtier, N. E., Cave, J. M., Foster, J. M., Walker, A. B. & Richardson, G. How transport layer properties affect perovskite solar cell performance: insights from a coupled charge transport/ion migration model. *Energy Environ. Sci* **12**, 396–409 (2019).

(14) Lin, Y. H., Vikram, Yang, F., Cao, X. L., Dasgupta, A., Oliver, R. D. J., Ulatowski, A. M., McCarthy, M. M., Shen, X., Yuan, Q., Christoforo, M. G., Yeung, F. S. Y., Johnston, M. B., Noel, N. K., Herz, L. M., Islam, M. S. & Snaith, H. J. Bandgap-universal passivation enables stable perovskite solar cells with low photovoltage loss. *Science* **384**, 767–775 (2024).

(15) Riquelme, A. J., Valadez-Villalobos, K., Boix, P. P., Oskam, G., Ivá Mora-Seró, ac & Anta, J. A. Understanding equivalent circuits in perovskite solar cells. Insights from drift-diffusion simulation †. *Phys. Chem. Chem. Phys* **24**, 15657 (2022).

(16) Yang, D., Ming, W., Shi, H., Zhang, L. & Du, M.-H. Fast Diffusion of Native Defects and Impurities in Perovskite Solar Cell Material CH 3 NH 3 PbI 3. (2016) doi:10.1021/acs.chemmater.6b01348.

(17) Peng, W., Aranda, C., Bakr, O. M., Garcia-Belmonte, G., Bisquert, J. & Guerrero, A. Quantification of Ionic Diffusion in Lead Halide Perovskite Single Crystals. *ACS Energy Lett.* **3**, 1477–1481 (2018).

(18) Futscher, M. H., Min Lee, J., McGovern, L., Muscarella, L. A., Wang, T., Irfan Haider, M., Fakharuddin, A., Schmidt-Mende, L. & Ehrler, B. Quantification of ion migration in CH3NH3PbI 3 perovskite solar cells by transient capacitance measurements. *Mater. Horiz.* **6**, 1497–1503 (2019).

(19) Mcgovern, L., Grimaldi, G., Futscher, M. H., Hutter, E. M., Muscarella, L. A., Schmidt, M. C. & Ehrler, B. Reduced Barrier for Ion Migration in Mixed-Halide Perovskites. *Appl. Energy Mater.* **4**, 13431–13437 (2021).

(20) Yun, J. S., Seidel, J., Kim, J., Mahboubi Soufi ani, A., Huang, S., Lau, J., Joong Jeon, N., Il Seok, S., Green, M. A., Ho-Baillie, A., Yun, J. S., Kim, J., Soufi ani, A. M., Huang, S., Lau, J., Green, M. A., Ho-Baillie, A., Seidel, J., Jeon, N. J., *et al.* Critical Role of Grain Boundaries for Ion Migration in Formamidinium and Methylammonium Lead Halide Perovskite Solar Cells. *Adv. Energy Mater.* **6**, 1–8 (2016).

(21) Siekmann, J., Ravishankar, S. & Kirchartz, T. Apparent Defect Densities in Halide Perovskite Thin Films and Single Crystals. *ACS Energy Lett.* **6**, 3244–3251 (2021).

(22) Eames, C., Frost, J. M., Barnes, P. R. F., O'regan, B. C., Walsh, A. & Saiful Islam, & M. Ionic transport in hybrid lead iodide perovskite solar cells. *Nat. Commun.* **6**, 1–8 (2015).

(23) Wu, N., Walter, D., Fell, A., Wu, Y. & Weber, K. The Impact of Mobile Ions on the Steady-State Performance of Perovskite Solar Cells. *J. Phys. Chem. C* **124**, 219–229 (2020).

(24) Bertoluzzi, L., Boyd, C. C., Rolston, N., Xu, J., Prasanna, R., O'regan, B. C. & Mcgehee, M. D. Mobile Ion Concentration Measurement and Open-Access Band Diagram Simulation Platform for Halide Perovskite Solar Cells. doi:10.1016/j.joule.2019.10.003.

(25) Sun, Q., Zhang, X., Zhao, C., Tian, W. & Jin, S. Carrier Transport in Lead Halide Perovskites. *J. Phys. Chem. C* **127**, (2023).

(26) Shi, Y., Rojas-Gatjens, E., Wang, J., Pothoof, J., Giridharagopal, R., Ho, K., Jiang, F., Taddei, M., Yang, Z., Sanehira, E. M., Irwin, M. D., Silva-Acuñ, C. & Ginger, D. S. (3-Aminopropyl)trimethoxysilane Surface Passivation Improves Perovskite Solar Cell Performance by Reducing Surface Recombination Velocity. *ACS Energy Lett.* **7**, 4081–4088 (2024).